General Disclaimer

One or more of the Following Statements may affect this Document

- This document has been reproduced from the best copy furnished by the organizational source. It is being released in the interest of making available as much information as possible.

- This document may contain data, which exceeds the sheet parameters. It was furnished in this condition by the organizational source and is the best copy available.

- This document may contain tone-on-tone or color graphs, charts and/or pictures, which have been reproduced in black and white.

- This document is paginated as submitted by the original source.

- Portions of this document are not fully legible due to the historical nature of some of the material. However, it is the best reproduction available from the original submission.

NASA

CHARGED PARTICLE SOURCES FOR IMPLANTATION AND SURFACE REACTIONS

F. G. Ruedenauer and C. K. Crawford

Final Report

December 1969

Particle Optics Laboratory Technical Report #4

Prepared under Contract No. NAS12-679 by

Particle Optics Laboratory

Massachusetts Institute of Technology

Cambridge, Massachusetts

Electronics Research Center

National Aeronautics and Space Administration

CHARGED PARTICLE SOURCES FOR IMPLANTATION AND SURFACE REACTIONS

F. G. Ruedenauer and C. K. Crawford

December 1969

Particle Optics Technical Report #4

Prepared under Contract No. NAS 12-679

by Particle Optics Laboratory

Massachusetts Institute of Technology

Cambridge, Massachusetts

Electronics Research Center

National Aeronautics and Space Administration

CONTENTS

CHARGED PARTICLE SOURCES FOR IMPLANTATION AND SURFACE REACTIONS

By Friedrich G. Ruedenauer and Charles K. Crawford
Massachusetts Institute of Technology, Cambridge, Massachusetts

SUMMARY

The steadily increasing use of integrated curcuits creates a need for the ability to bombard microscopically small areas with charged particles, especially electrons and ions. This ability can be of use in the fabrication of evaporation masks (i.e. by selective area bombardment of photoresists) or the direct creation of active elements by implanting or depositing a selected ion species on the surface of a solid. Due to the smaller wavelength of heavy particles the ultimate spatial resolution of ion generated patterns should be higher than the resolution achievable with electrons.

However to fully utilize the small particle-wavelength of ions two things are needed: high brightness ion sources which can produce ions of metals as well as gases, and a low aberration ion optical system which is capable of focusing a high current of selected ion species into a very small spot.

This work describes a high temperature ion source of the Unoplasmatron type with measured brightness values at 2kV of $\beta > 0.1$ A/cm^{2}sr for ions such as Ar, Pb, Ga. Beam currents for these elements were 6μA, 3μA, 1μA respectively. Total power input for the Ga run (operating temperature 1400°K) was < 110 watts. Source dimensions are 1" dia x 3.5" long.

The design of a demagnifying system is given which, if used in connection with the new ion source, is capable of bombarding a 1μm diameter spot with current densities > 50μA/cm^2. The main features of this system are a new type of a stigmatic focusing magnetic mass analyzer and a 3-lens electrostatic

focusing stage with a special minimum aberration postacceleration lens. Bombarding voltages can be as high as 40kV.

1. INTRODUCTION

This work concerns the development of an ion optics system which will deliver ions of a specific species and charge state with an intensity, energy spread, and emittance suitable for the image optical ion activation of photoresists. To show the feasibility of the method, initial experiments, including bombardment of a silicon dioxide layer, were performed.

To perform the desired functions an ion optical system must consist of

(a) a source which converts neutral atoms of various elements (gaseous as well as solid) into singly or multiply charged ions,

(b) an extraction and acceleration system to extract the ions from the source and accelerate them to an energy suitable for implantation or surface activation work and,

(c) a mass analyzer and focusing system to separate the beam according to particle mass number and charge state, and to make it impinge on the target in a preselected high resolution pattern.

The report is divided into four sections. Section 2 describes the development of the ion source and acceleration system. The system is capable of delivering ion currents in the microampere region from gaseous as well as solid substances. Constructional details and operating parameters are given.

Section 3 contains theoretical ion optical treatment of a special class of two-direction focusing magnetic mass analyzers. Compared to other stigmatic focusing magnetic analyzers, this type is characterized by a higher transmission at a given resolution. A 3-stage electrostatic demagnifying system is also described. This system is capable of producing patterns on the sample

surface with a resolution of the order of a few microns. Neither of these latter two systems has been constructed.

Section 4 describes exploratory experiments which were carried out to determine the feasibility of the concept of low energy ion implantation for photoresist activation and the stabilization of the silicon/silicon dioxide interface.

2. ION SOURCE DEVELOPMENT

A survey of various types of ion sources (Ref. 1) shows that in order to obtain extraction current densities in the order of mA/cm^2 (as are required by the proposed experiments) an ion source has to be selected which uses some kind of gaseous discharge to create a plasma from which ions can be extracted by a high electric field. To obtain a beam consisting of ions of only one element (or predominantly one element) the gas discharge should occur in the vapor of this element rather than in the vapor of a chemical compound containing it. For most elements in the periodic system, this means that the charge material (and the source itself) has to be kept at high temperature. Otherwise the equilibrium vapor pressure of the charge material in the discharge volume will be too low. Gas discharge type ion sources normally operate at pressures in the range of $10^{-3} \rightarrow 10^{-1}$ torr; thus temperatures up to $1500^{\circ}K$ must be reached to process elements like In or Ga.

High temperature gas discharge ion sources which are capable of producing ions of low or medium vapor pressure metals have been built by many investigators. Most of these ion sources have large linear dimensions and surface area. Consequently, they radiate large amounts of power (a few KW) when operated at elevated temperatures. The aim of the present design is to build a small high temperature source which can operate with a low power consumption. The

Unoplasmatron type source first described by von Ardenne (Ref. 1) lends itself well to miniaturization, is characterized by high efficiency and low power consumption and does not require an auxiliary magnetic field. Thus, this type was chosen. Previously, Unoplasmatrons have only been operated as gas ion sources, hence many changes from the published designs are necessary to adapt it for use with metallic vapors. It was decided to proceed in two steps: First, a small stainless steel Unoplasmatron with variable geometric dimensions was built to gain insight into the discharge parameters, power consumption, efficiency, etc. Second, using the optimized parameters, a high temperature version was designed. The high temperature source is suitable for gases as well as solids.

2.1. Unoplasmatron Gas Source

The gas ion source and ion source test setup described in this section is constructed mostly from stainless steel type 304 and consists of the ion source, extraction electrode and a 3-grid Faraday cage, all mounted in a single frame. It is designed to give information concerning arc parameters, power consumption, efficiency, emittance, etc. and to allow an optimization of the final solid material source.

2.1.1. Construction details.--Fig. 1 shows a schematic of the Unoplasmatron gas source. It consists of anode (2) with an extraction opening (1), intermediary electrode (5), cathode (6), electron reflector (7), and feedthroughs (8). The intermediary electrode-anode distance may be adjusted by sliding the intermediate electrode along the standoffs (9) and the cathode-anode distance can be adjusted by moving the backplate (4) inside the tightly fitting anode cylinder (10). Thus, a geometrical optimization of arc parameters is possible.

The operating mechanism of the source (Ref. 2) can be briefly described

as: a) a low voltage arc discharge is burning between the hot filament cathode (6) and the anode (2); b) an intermediary electrode (5) with a hole punched in its top surface (Fig. 1) mechanically constricts the plasma column between the cathode and the anode; and c) a discharge current passing through the opening in the intermediary electrode (IE) creates a very dense plasma between IE and anode.

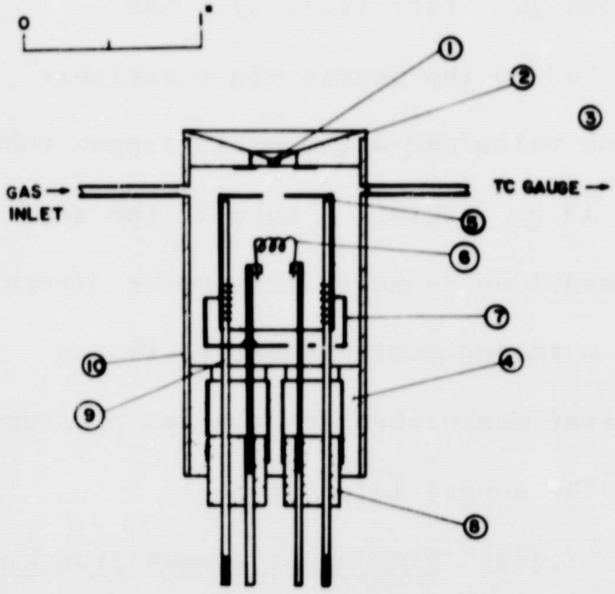

Fig. 1 Experimental Unoplasmatron Gas Ion Source

Ions are extracted from the plasma by an extractor electrode (Fig. 2) which, with the anode plate of the ion source (Figs. 3 and 4), forms a Pierce-extraction sytem. The function of this special extraction system is to guide the extracted particles into a parallel or low divergence beam as long as the the extracted particle current is space charge limited. A 3-grid Faraday collector is mounted on the same axis as the ion source and extraction electrode at a distance of about 5cm from the extraction opening of the source. This arrangement provides for a measurement of the total unfocused extraction current which passes through the 0.125 cm dia hole in the extraction electrode, as well as for energy analysis

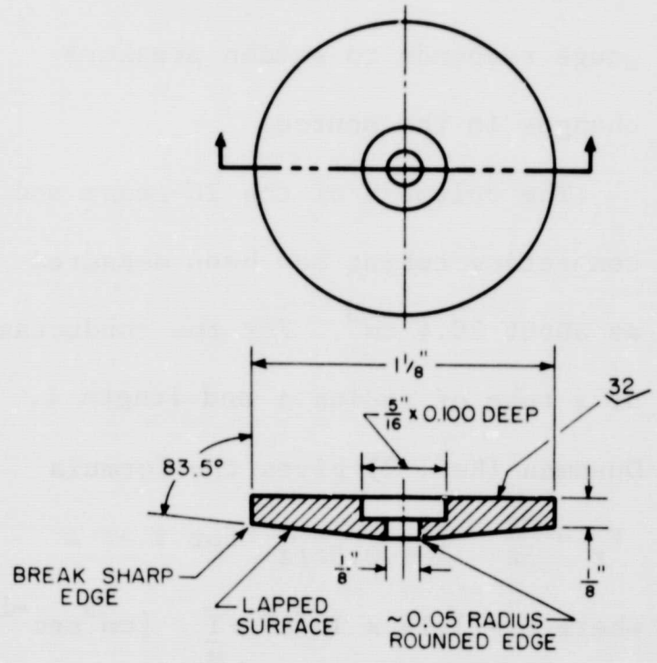

Fig. 2 Extraction Electrode (Pierce Geometry)

of the extracted ions and electrons.

The source-extractor-collector assembly is mounted in a vacuum system capable of achieving pressures of better than 10^{-5} torr (Fig. 5). Gas is fed to the source via a variable leak valve and a 2.0 mm ID copper tube of 15 cm length. A tube of the same dimensions connects the source directly to a thermocouple gauge, so that a direct measurement of the gas pressure in the source is possible.

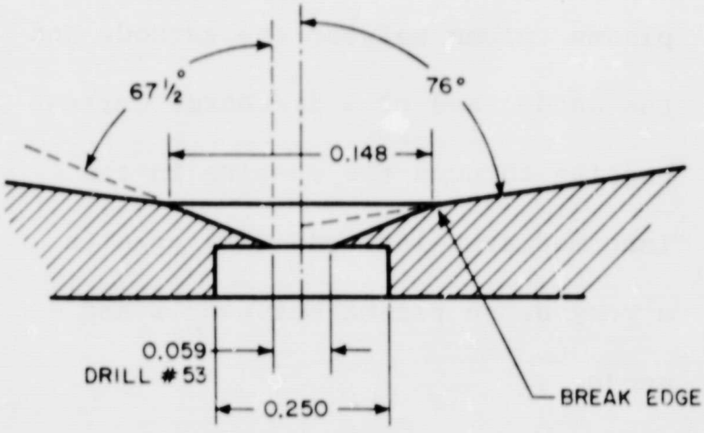

Fig. 3 Unoplasmatron Anode (Pierce Geometry)

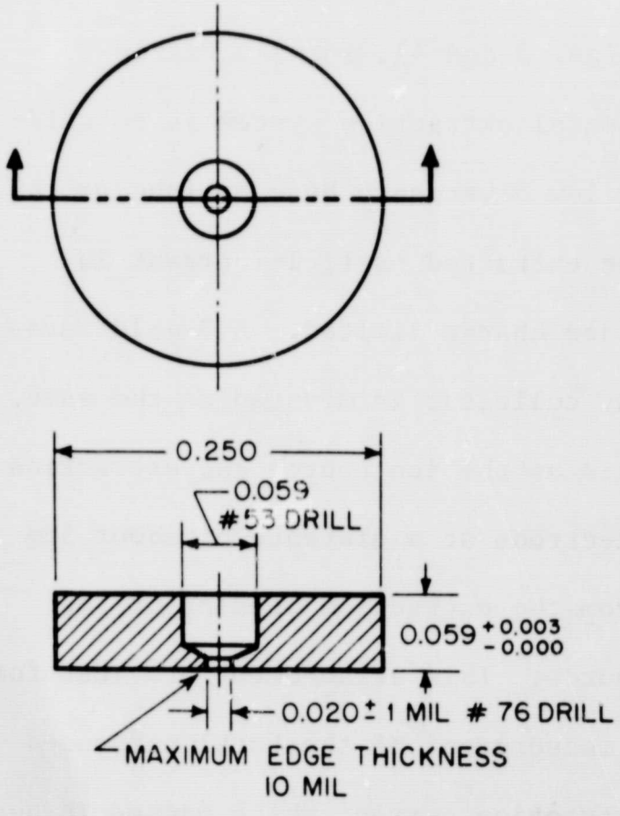

Fig. 4 Unoplasmatron Anode Expansion cup

2.1.2. Timelag of source pressure indication.--From the volume of the thermocouple gauge (V_{TC} = 20 cm^3) and the volume and conductance of the connecting tubing it is possible to estimate the speed with which the TC-gauge responds to sudden pressure changes in the source.

The volume V of the TC-gauge and connecting tubing has been measured as about 20.4 cm^3. For the conductance of a tube of radius a and length ℓ, Dushman (Ref. 3) gives the formula

$$F_t = \frac{8a}{3\ell} \cdot \frac{F_o}{1 + 0.5\ell/a} \quad \text{for } \ell >> a$$

where $F = 1.14 \times 10^3 a^2 \sqrt{\frac{T}{M}}$ $[cm^3 sec^{-1}]$

is the conductance of a circular orifice of the same diameter a. From these expressions we get ($T = 293^{o}K$, $M = 40$) for room temperature and argon gas, a conductance of the connecting tubing of

$$F_t = 5.2 \text{ cm}^3/\text{sec}.$$

The same author gives a formula for the time interval required to pump down a vessel of volume V from a pressure p_1 to a pressure p_2 via a conductance F_t

$$t = \frac{V}{F_t} \ln \left(\frac{p_1}{p_2}\right)$$

Therefore the time $t_{1/2}$ required to pump down a volume V to half its initial pressure is given by

$$t_{1/2} = \frac{V}{F_t} \ln 2 = 2.73 \text{ sec}.$$

This value can be considered as the 'time constant' of the system gauge-connecting tubing. $t_{1/2}$ should be as small as possible to detect pressure changes in the source quickly and prevent damage to the filament. For the present application this conductance value seems to be adequate especially since the TC gauge itself needs a time τ of 1-3 seconds (Fig. 6) in the pressure range 10^{-2} - 10^{-3} torr to change its reading by a voltage increment which corresponds to a change of pressure of a factor of 2.

2.1.3. Calibration of source pressure measurement.--Keeping in mind the adaptation of the present Unoplasmatron gas source to a metal vapor ion source two parameters are of special importance, namely gas pressure in the source and gas flow through the extraction hole. The source pressure p_s determines the temperature level at which the metal source has to be kept, and the gas flow Q_s through the extraction hole determines the mass loss per unit time and therefore the charge lifetime and efficiency of the metal source.

As follows from the previous section the pressure in the Tc gauge should be very close to the pressure in the source if steady state molecular

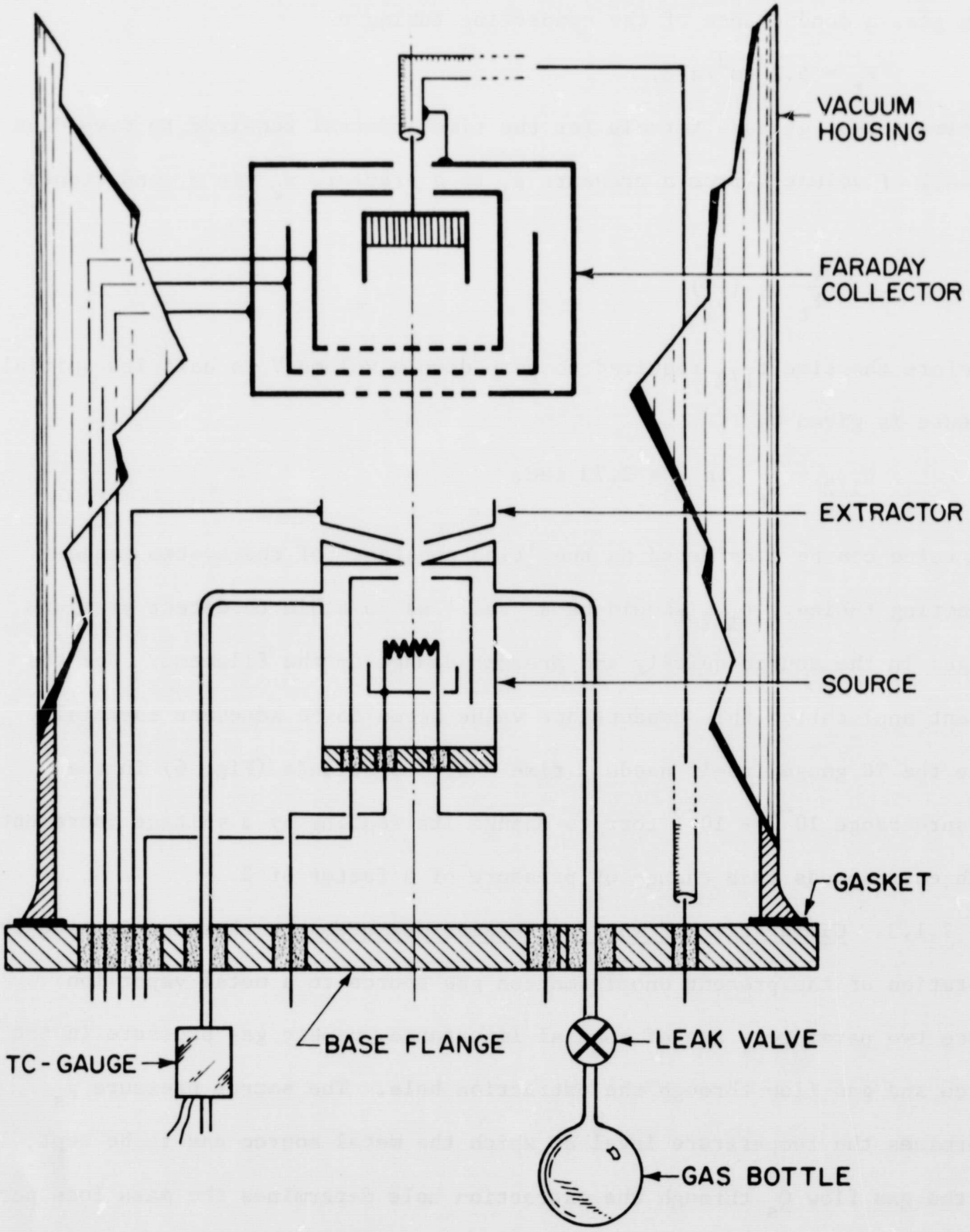

Fig. 5 Ion Source Test System

flow conditions prevail. However, the pressure measurement by means of a TC gauge has its limitations. Fig. 7 shows the calibration curve given by

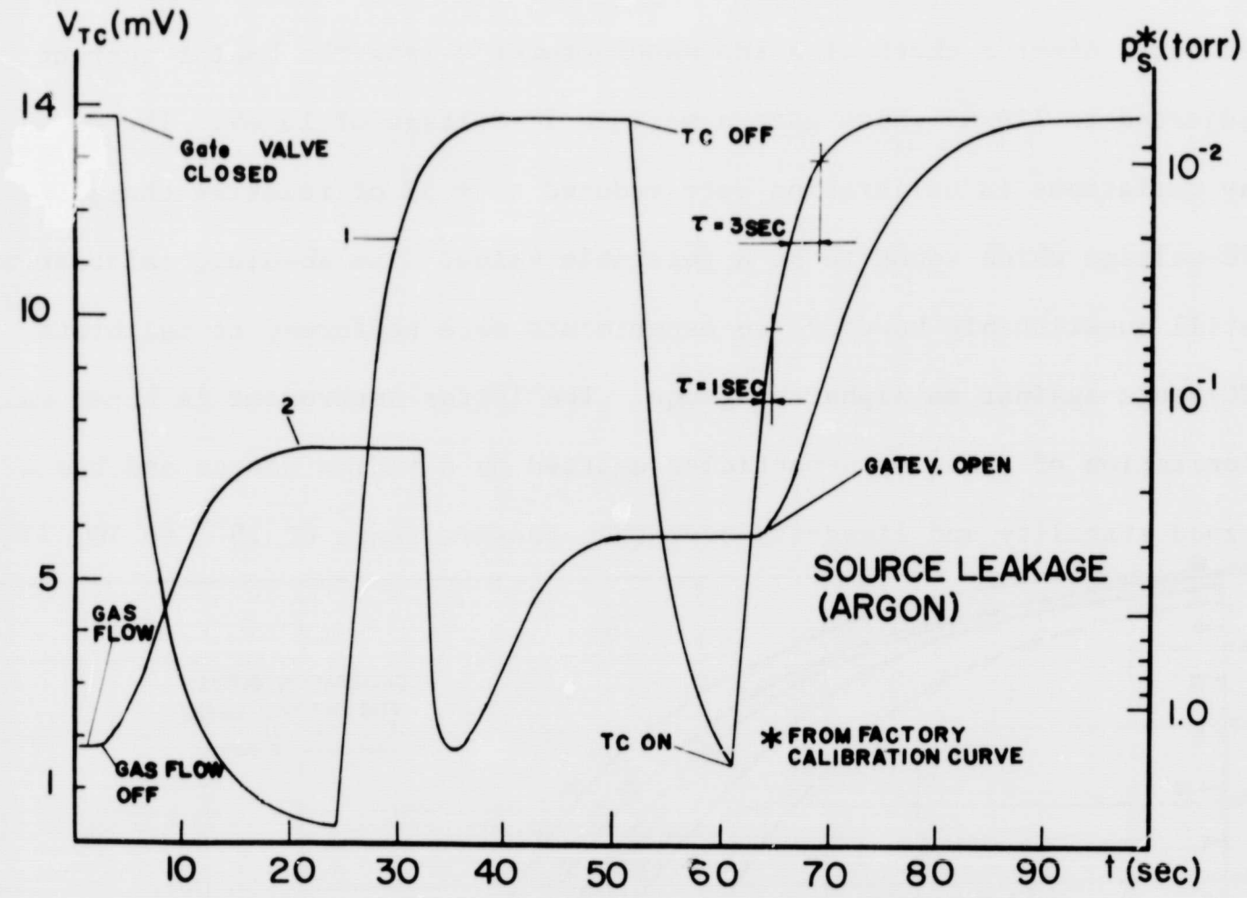

Fig. 6 Leak Rate of Unoplasmatron Extraction Opening (Curve 1)
Timelag of Thermocouple Gauge (Curve 2)

the manufacturer (NRC) for the model 521 TC gauge. It shows that in the pressure range of 10^{-3} to 10^{-2} torr the TC-voltage is dependent on room temperature over the whole pressure range but has only slight dependence on the pressure. In the 10^{-3} region a change of 5^{o}C in room temperature gives a change in pressure reading of about a factor of 2. When the first tests with gauges of this model were performed the calibration changed as much as 50% from day to day even with the room temperature kept constant. It was discovered that the TC-heater current of 161 mA specified by the manufacturer on each of three purchased gauges resulted in a TC-voltage at "zero" pressure ($< 10^{-3}$ torr) of 24 mV instead of the 14 mV maximum voltage in Fig. 7.

This probably caused the thermojunction to overheat and malfunction, supported by the fact that the gauge which had been operated longest at 161 mA had burned out. After a check with the manufacturer's labs the heater current was adjusted to 119 mA which gave a maximum TC-voltage of 14 mV. The day-to-day variations in calibration were reduced to $\pm$ 5% of relative change of the TC-voltage which seems to be a tolerable value. The absolute calibration was still questionable however, so experiments were performed to calibrate the TC-gauge against an Alphatron gauge. The latter instrument is based on the ionization of a gas by α-particles emitted by a radium source and has a very good stability and linearity over the pressure range of 10^{-4} to 100 torr

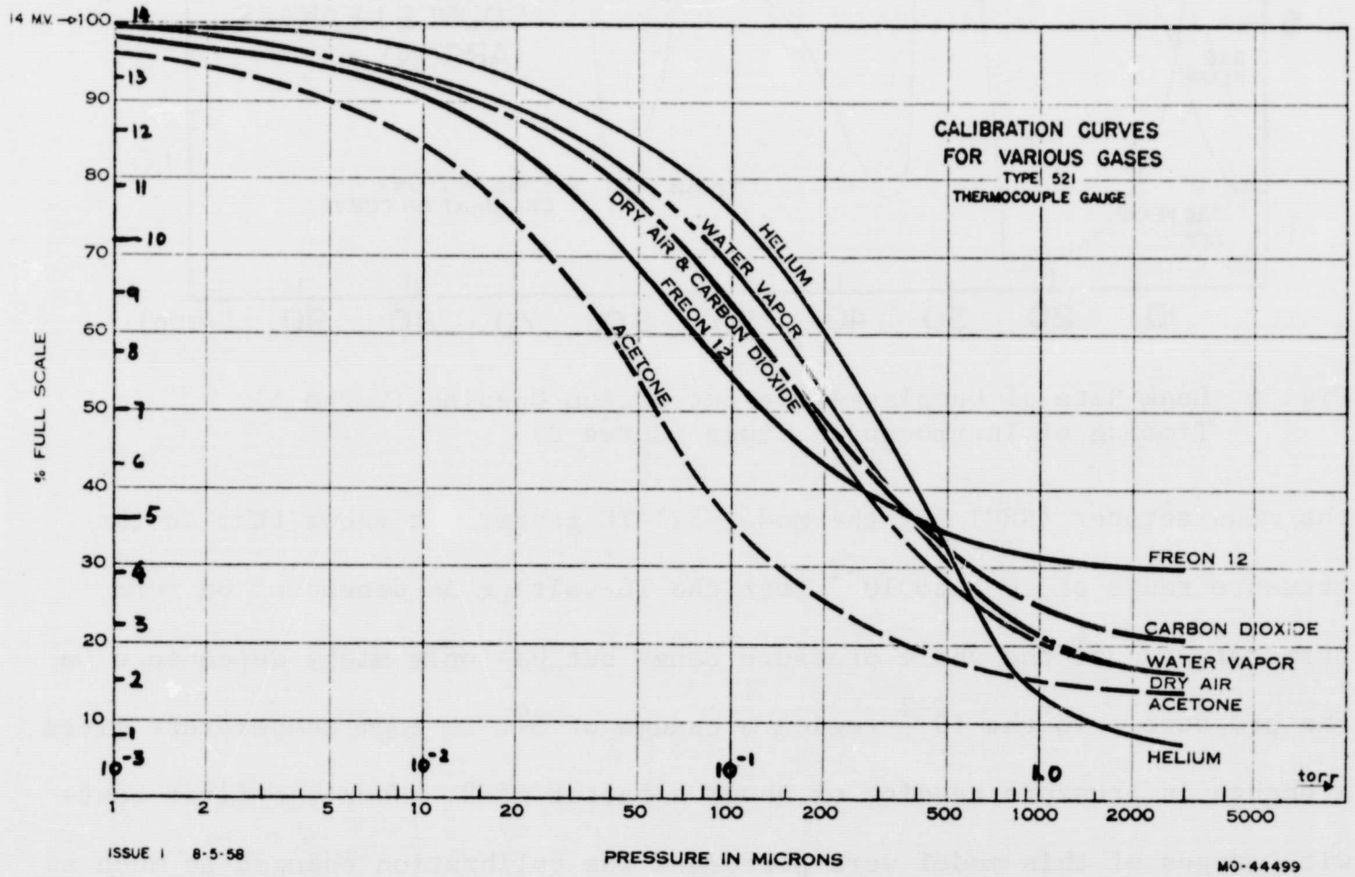

Fig. 7 Calibration of a NRC TC521 Thermocouple Vacuum Gauge

but it is of little use in the present experiment since its large volume of about 250 cm^3 gives it a timelag of about 20 seconds with respect to pressure changes in the ion source.

Fig. 8 shows TC voltage (% of 14 mV) against Alphatron reading (curve a) in the pressure range 0.2 torr → 5 torr and TC voltage against dry air pressure (curve b) from the NRC manual (Fig. 7). Due to lack of pumping speed in the test system curve (a) could not be traced below 0.2 torr. From the available data in Fig. 7 however, it is obvious that at 1 torr the thermocouple reads about a factor of 1.68 too low in pressure if the Alphatron reading is corrected for Argon gas (Ref. 3). From the same figure it appears that this factor would decrease to at least 1.45 for lower pressures (below 10^{-1} torr).

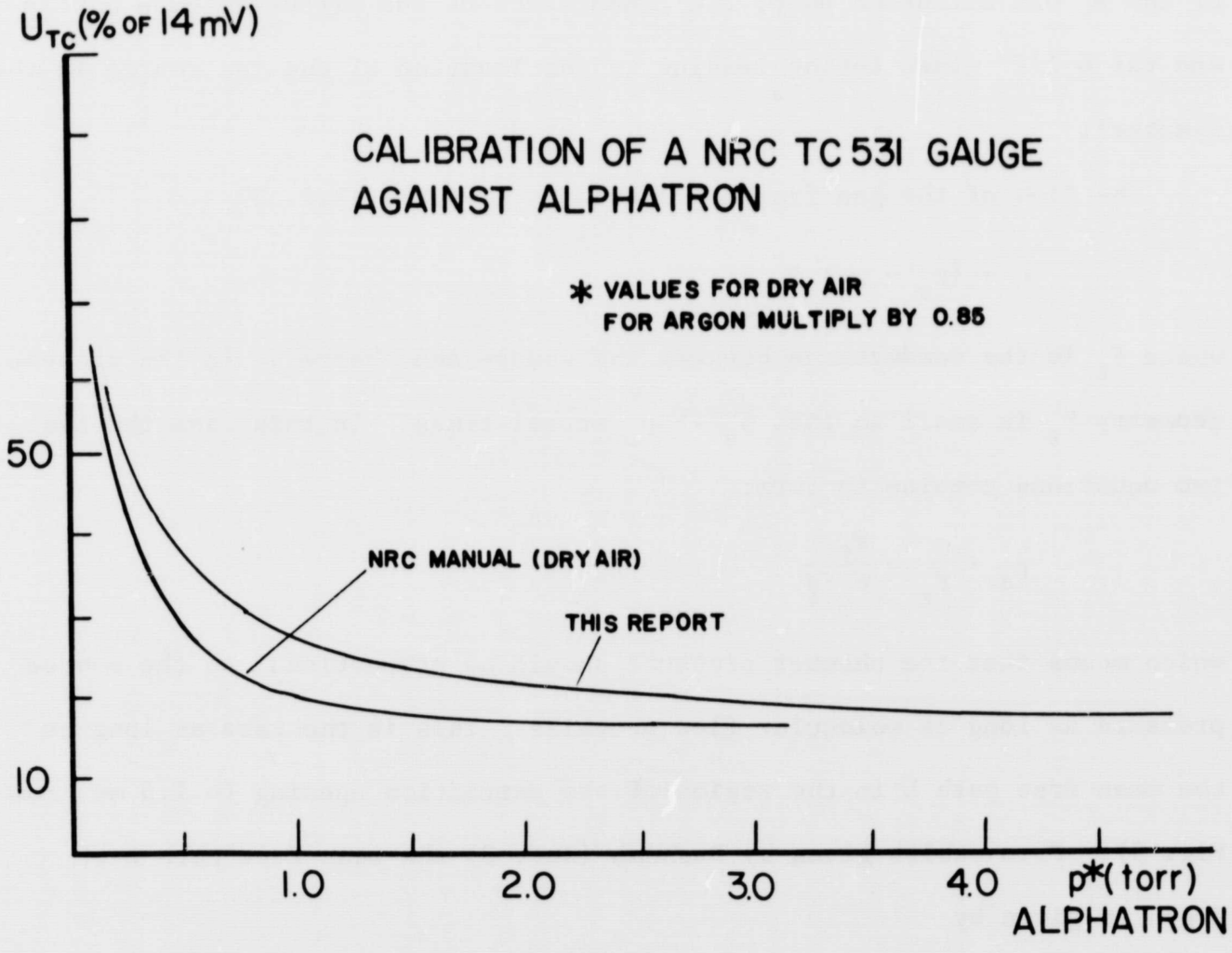

Fig. 8 Calibration of a NRC TC531 Gauge against NRC Alphatron Gauge

Summarizing we can say that in the pressure range 1 → 10^{-2} torr thermal

drift and heater instability limit the absolute accuracy of the thermocouple gauge to about ± 25%. Below 10^{-2} torr the accuracy is further decreased by the flattening out of the characteristic.

Another indirect method to measure source pressures is to measure the pressure p_c in the vacuum chamber (Fig. 5). This pressure has a certain relationship to the gas flow from the source (Q) given by the equation (Ref. 3)

$$p_c = \frac{Q}{S_c}$$

where S_c is the pumping speed in the vaccum chamber (determined by the speed of the 6" oil diffusion pump, the conductance of the diffusion pump baffle and the 6 1/2" glass tubing leading to the location of the ion source in the chamber).

The flow of the gas from the source is given by (Ref. 3)

$$Q = (p_s - p_c)\, F_t .$$

where F_t is the conductance between the source and chamber. In the present geometry F_t is small so that $p_s >> p_c$ at all times. In this case the last two equations combine to form:

$$p_s = \frac{Q}{F_t} = \frac{p_c}{S_c F_t}$$

which means that the chamber pressure should be proportional to the source pressure as long as molecular flow prevails. This is the case as long as the mean free path L in the region of the extraction opening (= 1.5 mm from Fig. 4). From tables given by Dushman (Ref. 3) the mean free path L of Argon is given by

$$L = 4.7 \times 10^{-3}/p \quad [cm]$$

which gives a value of $p \simeq 3 \times 10^{-2}$ for source pressure to which the chamber pressure should be proportional. Fig. 9 shows the relationship between

p_c and p_s. p_c was measured with a Bayard-Alpert ionization gauge and p_c with the TC-gauge. One recognizes that an approximately linear relationship holds up to 1 torr. Extrapolation of this curve to values $p_c < 10^{-5}$ torr should give a good approximation for $p_s < 10^{-2}$ torr. Unfortunately, the leak rate of the vacuum chamber limits the ultimate chamber pressure to about 4×10^{-6} which means that for source pressures below 4×10^{-3} the outgassing and leak rate of the vacuum chamber exceeds the inflow of gas through the scource opening.

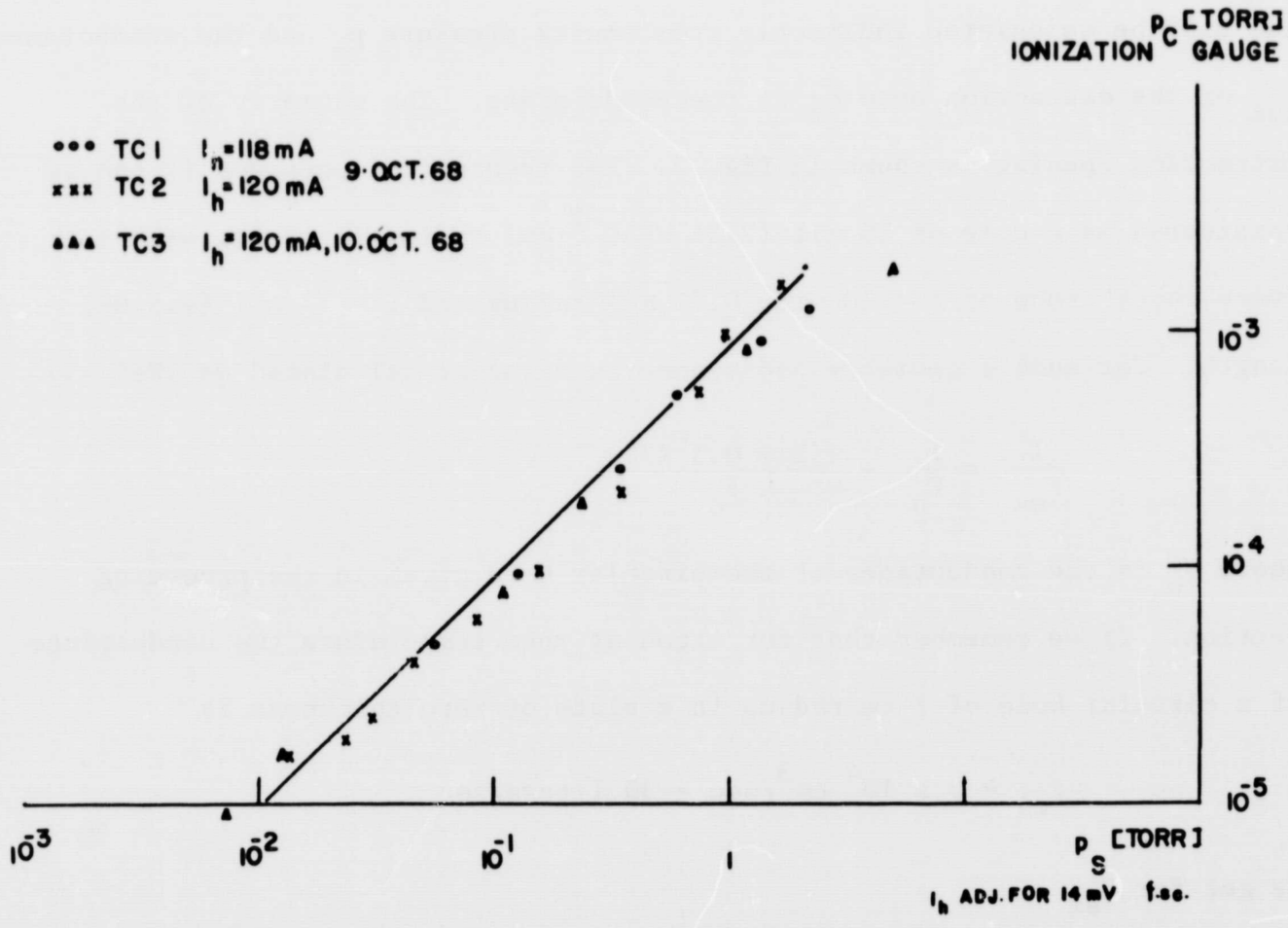

Fig. 9 Relationship between Vacuum Chamber Pressure and Ion Source Pressure

As a conclusion we can say that source pressures in the range of 1.0 → 5×10^{-2} torr can be covered by direct measurement with the TC-gauge with an absolute accuracy of $\pm$ 25%. By measurement of the chamber pressure with an

ionization gauge we can extend this range down to $p_s \approx 5 \times 10^{-3}$. Below that no measurements can be meaningfully taken with the present setup. However, as will be shown, the source operates effeciently only at pressures about 10^{-2} torr, so that the mentioned deficiency in pressure measurement is of no great consequence for the scope of the present work.

2.1.4. Neutral gas loss.--Due to the lack of a mass flow meter with short settling time and sufficient accuracy to measure mass flows in the range of 10^{-2} torr cm^3 sec^{-1} (0.3 μg/sec) the flow of gas from the source can only be calculated indirectly from source pressure p_s and the conductance F_{ex} of the extraction opening in the anode plate. The geometry of the extraction opening is shown in Fig. 3. For theoretical purposes it can be considered as a hole of 10 mil (2.54×10^{-2} cm) radius in series with a "very short" tube of a = 30 mil (0.76 mm) radius and ℓ = 59 mil (1.5 mm) length. For such a geometry the conductance can be calculated as (Ref. 3)

$$\frac{1}{F_{ex}} = \frac{1}{F_o} + \frac{(1 + 0.5\ \ell/a)}{F_o}$$

where F_o is the conductance of the circular hole given in the preceding section. If we remember that for Argon at room temperature the conductance of a circular hole of 1 cm radius in a plate of zero thickness is

$$F_{o1} \approx 3 \times 10^4 \text{ cm}^3/\text{sec} = 30 \text{ liters/sec}$$

we get for F_{ex}

$$F_{ex} = \frac{3 \times 10^4 a^2}{1 + 1 + 0.5\ell/a} = \frac{3 \times 10^4}{3}\ a^2 = 6.25 \text{ cm}^3/\text{sec}$$

From another formula in section (a) we get for the gas flow Q through the exit hole

$$Q = (p_s - p_c)\ F_{ex} \approx p_s F_{ex} = 6.25\ p_s \ [\text{torr cm}^3\text{sec}^{-1}]$$

or $$Q = 6.25 \frac{p_s}{760} \times N_A = \frac{6.25\ p_s \times 2.69 \times 10^{19}}{760} \cong 2.22 \times 10^{17} p_s \ [\text{atoms/sec}]$$

where N_A is the number of atoms per cm^3 at NPT, or

$$Q = \frac{2.22 \times 10^{17}}{N_L} \times 40 p_s \cong 14.0 \times p_s \ [\mu g/sec]$$

N_L....Avogadro's number

(All values for Argon at room temperature)

One gram of Argon passes through the exit hole in a time t_{1g} given by

$$t_{1g} = \frac{10^{-3}}{3.6 \times Q} = \frac{1}{14 \times 10^{-6} \times 3.6 \times 10^{3} p_s} = \frac{19.7}{p_s} \ [h]$$

Principally the gas flow through the extraction hole could be measured by observing the pressure drop in the TC-gauge when the ion source is pumped down from an initial pressure p_s without any gas being supplied through the leak valve (Fig. 5). This has been done (Fig. 10). The source was filled with Argon at a pressure of about 0.3 torr by closing the gate valve to the diffusion pump which evacuated the vacuum chamber and sending a short burst of gas through the exithole into the vacuum chamber. The gas flow Q through the extraction hole is related to the observed pressure drop in the TC gauge by the expression

$$Q_{obs} = \frac{dp}{dt} V$$

where V is the volume of the source plus gauge ($40cm^3$). The Q-values derived from this equation are about 2 times as high as the theoretical Q values given by

$$Q_{th} = F_{tot} \times p_s$$

where F_{tot} is the effective conductance between the vacuum chamber and the TC gauge:

$$\frac{1}{F_{tot}} = \frac{1}{F_t} + \frac{1}{F_{ex}} \quad \text{or } F_{tot} = 2.85\ [cm^3 sec^{-1}]$$

This discrepancy can be caused by

i) inaccuracy in absolute pressure reading

ii) lag of TC gauge; in the pressure range of interest the time required for the pressure to drop to half its momentary value is about the same as the time lag of the thermocouple.

iii) the exit hole is not the only path by which the gas can escape from the source into the vacuum chamber. Two such critical points are the Swagelok-couplings with teflon ferrules by which the gas feed tubing and the pressure measurement tubing are connected to the ion source body.

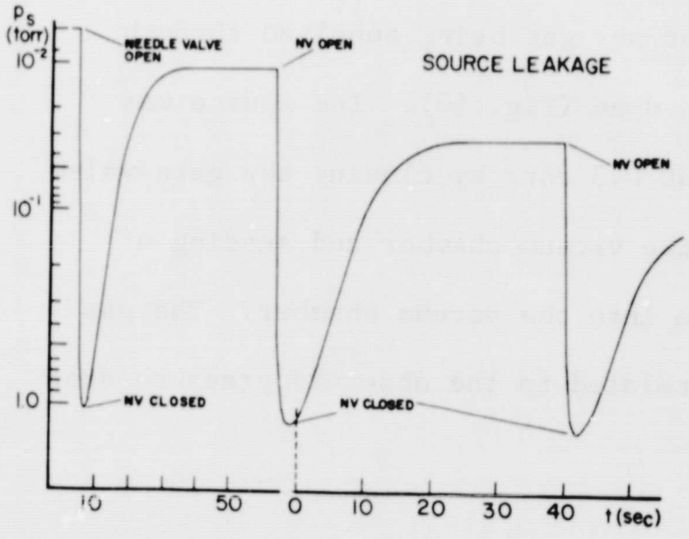

Fig. 10 Decrease of Ion Source Pressure Due to Pumping Speed of Extraction Opening

iv) theoretical values for conductances of certain geometrical configurations are only approximations which may deviate from the actual values by as much as 25% (Ref. 3). An agreement within a factor of 2 can therefore be considered as satisfactory.

From the value of t_{lg} calculated above it can be concluded that even for the case where the theoretical conductance values are too small by a factor of 2 an ion source of the same dimensions as the tested source which operates around 10^{-2} torr could be run about 55h with a charge of 0.5g Argon gas.

2.1.5. Electron emission from the filament.--From the data of Kistemaker (Ref. 2) regarding the operating parameters of a Unoplasmatron-type source it

can be expected that discharge currents in the order of 1A have to be obtained for ion extraction currents of the order of a few μA. With an expected operating pressure of $\leq 10^{-2}$ torr and the application of well known ionization and multiplication mechanisms in gases of low pressure it can be estimated that the filament should be able to supply about 150mA of emission current. From tables given by Kohl (Ref. 4) and in order to match existing power supplies a 0.254 mm (10 mil) dia pure W wire of the order of 10 cm length was chosen as the emission filament. The W wire was wound in the shape of a straight coil (2 mm dia x 1 cm long) with between 15 and 19 windings. The coil was spotwelded to two 4 x 3 x 0.2 mm tantalum strips which in turn were spotwelded to two tantalum filament holders of 1.27 mm (47 mil) dia. Fig. 11 gives theoretical saturation electron currents (Ref. 4) for 10 cm of W wire of the specified diameter as a function of heating current.

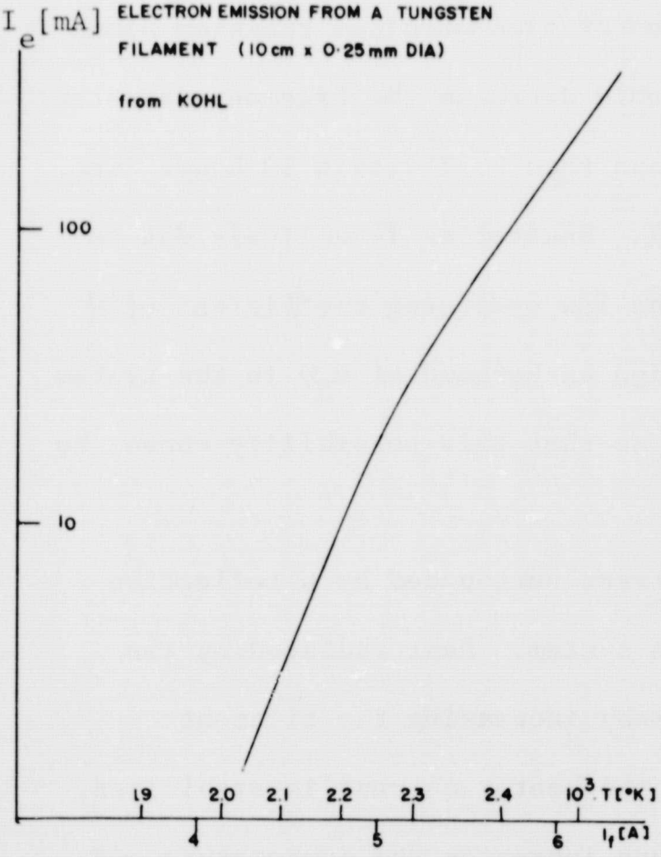

Fig. 11 Electron Emission from a hot Tungsten Filament

To measure the actual emission characteristic the source was mounted in the vacuum chamber (Fig. 5) which was pumped down to about 3.2×10^{-5} torr. According to Fig. 9 this would correspond to a source pressure of 3.5×10^{-2} torr if the gas were flowing through the source. However, since no gas was introduced the high chamber pressure must have been caused by outgassing and leakage in the chamber itself. At this point the TC-gauge showed a reading of less than 3×10^{-3}

torr, so that the source pressure with no gas flow can be estimated somewhere between 1 and 2 x 10^{-3} torr. Fig. 12 shows the voltage-current characteristics obtained in the circuit shown in Fig. 13. The marks on the right edge of Fig. 12 give the theoretical saturation electron currents for various filament heating currents. It is obvious that at 140V Intermediary electrode (IE) voltage the observed values are about 15% higher than the theoretical values. This could have the following causes:

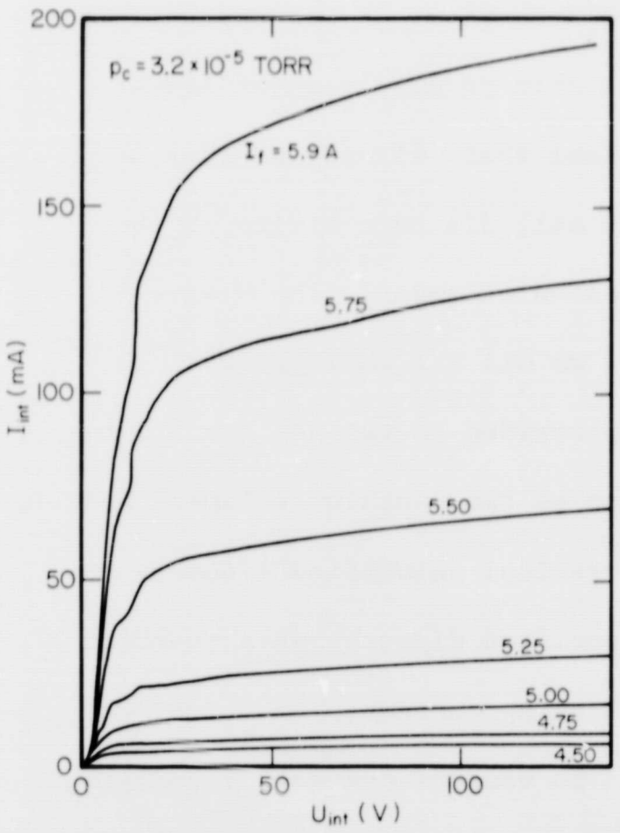

Fig. 12 Voltage-current Characteristics for Circuit of Fig. 13; No gas introduced

i) The filament has become thinner by thermal evaporation or sputtering. Evaporation of clean tungsten alone would decrease the filament diameter less then 0.1% within 10 hours (Ref. 4). Sputtering is unlikely due to the low sputtering coefficient of W by 150V ions. However the considerably high background of H_2O in the system could oxidize the filament rather rapidly so that this possibility cannot be discarded.

ii) A filament with stabilized heater current surrounded by a reflective material is basically a thermally unstable system. Heat radiated by the filament is partially reflected back, thereby increasing the filament temperature and its Ohmic resistance. If the heater current is stabilized, the input wattage is increased which in turn increases the temperature and electron emission. This thermal feedback however is a slow process and

should not be noticeable in our case since the emission characteristic was scanned through in about 10 seconds.

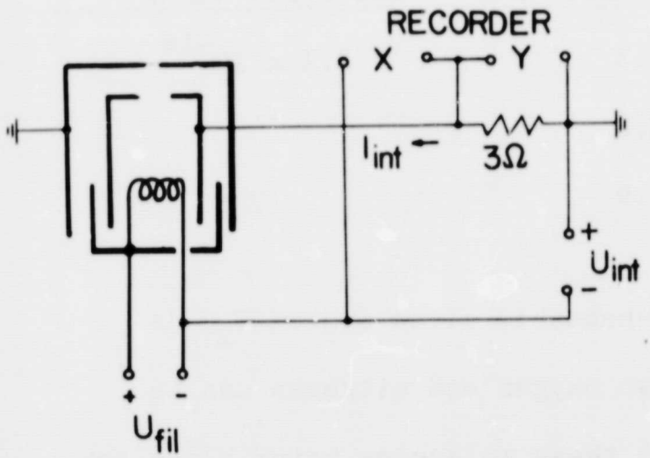

Fig. 13 Wiring Schematic for Discharge between Filament and Intermediary Electrode

iii) A process which would not exhibit any timelag would be ionization of the residual gas in the source by the electrons united from the filament. The ions and electrons formed in this primary ionization process would contribute to the measured current value. At residual gas pressures of 2-3 x 10^{-3} torr which, as mentioned above, can be expected in the source this ionization could not occur below a certian limit of the filament-IE potential. This voltage limit would be determined by the ionization potentials of the molecules present in the residual gas. In fact, the curves in Fig. 12 show a sharp rise of the IE-current in the vicinity of 13V IE voltage. Table I lists the species of molecules most likely to be present in the source together with their ionization potentials (Ref. 5) and 150V electron ionization cross sections (Ref. 6).

TABLE I

Ion Species	Parent Molecule	Ionization Potential (eV)	Cross Section for 150V Electrons (cm^2)
N_2^+	N_2	15.55	2.6 x 10^{-16}
	N	14.54	
O^+	O	13.61	2.4 x 10^{-16}
O_2^+	O_2	12.2	2.8 x 10^{-16}
H_2O^+	H_2O	12.61	

TABLE I (cont'd)

Ion Species	Parent Molecule	Ionization Potential (eV)	Cross Section for 150V Electrons (cm^2)
NO_2^+	NO_2	12.3	3.2×10^{-16}
OH^+	OH	12.8	
CH_2^+	CH_2	11.9	

Since the source is mounted in a non-bakeable glass system H_2O is likely to be present in large amounts, also oxygen and nitrogen can be expected, the ionization potentials of all these molecules being close to the observed discontinuity in the emission characteristics.

For a quantitative evaluation let us assume a residual gas pressure of 3×10^{-3} torr and an average ionization cross section of $2.9 \times 10^{-16} cm^2$ and a filament-IE-distance of $\ell = 1.2$ cm.

The number of electrons per second arriving at the IE is given by (Ref. 7)

$$N_-(\ell) = N_o \, e^{\alpha \ell}$$

where N_o is the number of electrons per second emitted by the filament and α is the primary Townsend coefficient for ionization which is given by

$$\alpha = \sigma n = \sigma \frac{N_A}{760} p \cong 3.55 \times 10^{16} \, p$$

n.....number of molecules/cm^3

N_A....Avogadro's number

σ.....ionization cross section (cm^2)

p.....pressure (torr)

The number of ions produced in the volume is given by (Ref 7)

$$N_A(\ell) = N_o \, \alpha \ell$$

The total current across the electrode gap is the sum of ion and electron current. If we substitute I for N in the preceeding equations and retain the linear term in the exponential function we get

$$I_{tot} = I_+ + I_- = I_o\ (\alpha\ell + 1 + \alpha\ell) = I_o\ (1 + 2\alpha\ell) = I_o(1 + 7.1 \times 10^{16}\ \sigma p)$$

With the values of σ and p above we get

$$I_{tot} = I_o\ (1 + 6.2 \times 10^{-2})$$

From Fig. 12 one would expect about twice that value so that most likely filament aging (by oxidation) and residual gas ionization both contribute to give the measured current value.

Summarizing we can say that an emission current of 150 mA can be obtained by heating a 12 cm long pure tungsten wire of 0.254 mm dia to $> 2400^{o}K$ (Ref. 4). This requires 5.9A and 72 watts (Ref. 4). Filament life in a non-oxidizing atmosphere at pressures below 10^{-3} can be expected to be in excess of 10,000 h (for a 10% decrease in filament diameter).

2.1.6. Gas discharge between filament and Intermediary Electrode-- As the next step Argon gas was introduced into the source and the voltage-current characteristics measured in the same circuit as in Fig. 13. The only difference was that the U_{int} power supply (with automatic crossover feature) was set to an upper current limit of 195 mA.

Figs. 14 and 15 show the U_{int}-I_{int} characteristics with the Argon pressure P_A in the vacuum chamber as a parameter. The corresponding source pressures can be taken from Fig. 9. There are obviously two different regimes in which an arc (negative I-V characteristic) can burn. The first regime is characterized by low gas pressure and low arc voltage. Fig. 14 shows that if the argon pressure in the chamber is increased above 1.2×10^{-5} Torr the curves exhibit portions of negative slope, the arc voltage at

the power supply limited arc current of 195 mA decreases with increasing gas pressure. The curves in Fig. 15 were measured under exactly the same experimental conditions as those in Fig. 14. They were only plotted separately in order not to obscure the graph. In that figure we see a second regime characterized by high gas pressures and high arc voltages which increase with increasing pressure.

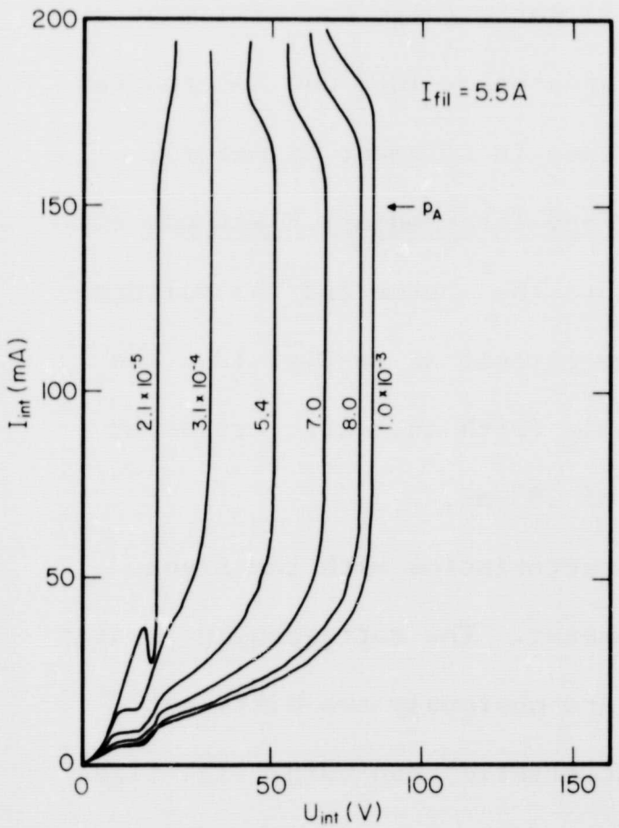

Fig. 15 Voltage Characteristics for Circuit of Fig. 14; Gas Introduced into Ion Source

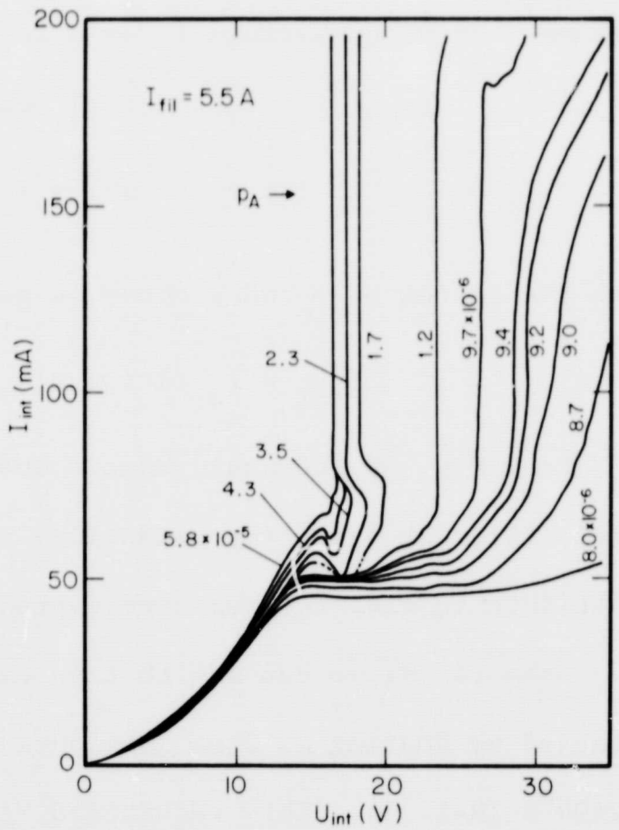

Fig. 14 Voltage-current Characteristics for curcuit of Fig. 13 Gas Introduced into Ion Source

Thermal electron emission from the filament was approximately 50 mA as indicated in Fig. 14 where the U_{int}-I_{int}-curve for $P_A = 8 \times 10^{-6}$ torr saturates at about this value.

From the measurements it is obvious that in Argon gas a 200 mA arc can be struck between the filament and the intermediate electrode at source pressures as low as 10^{-2} torr ($p_c = 1 \times 10^{-5}$). In this case

the arc voltage is about 24V and the power consumption in the discharge approximately 4.8 watts. Including the heater power for the filament a total of about 55 watts is dissipated within the source.

2.1.7. Gas discharge between filament and anode.--If voltage is applied between filament and anode the intermediary electrode being connected to the negative filament lead (see insert in Fig. 16) the corresponding I_A-U_A characteristics for different pressure values are given in Fig. 16. In this figure one sees that irrespective of the gas pressure no measureable anode current is flowing below a filament to anode voltage $U_A \cong 16V$. In this case the electron cloud emitted by the filament obviously is contained within the intermediary electrode cylinder and only a small fraction diffuses through the 3.2 mm dia hole in that electrode and reaches the anode. As U_A increases the anode potential slowly penetrates through the IE-opening and accelerates part of the electron cloud towards the anode. Ionization of the gas takes place and if the gas pressure is high enough a plasma column is formed essentially between filament and anode. If in the schematic in Fig. 16 a resistor of suitable size is connected between IE and filament, the fraction of the electrons which flow to the IE produce a negative bias there so that the IE-current is reduced to a

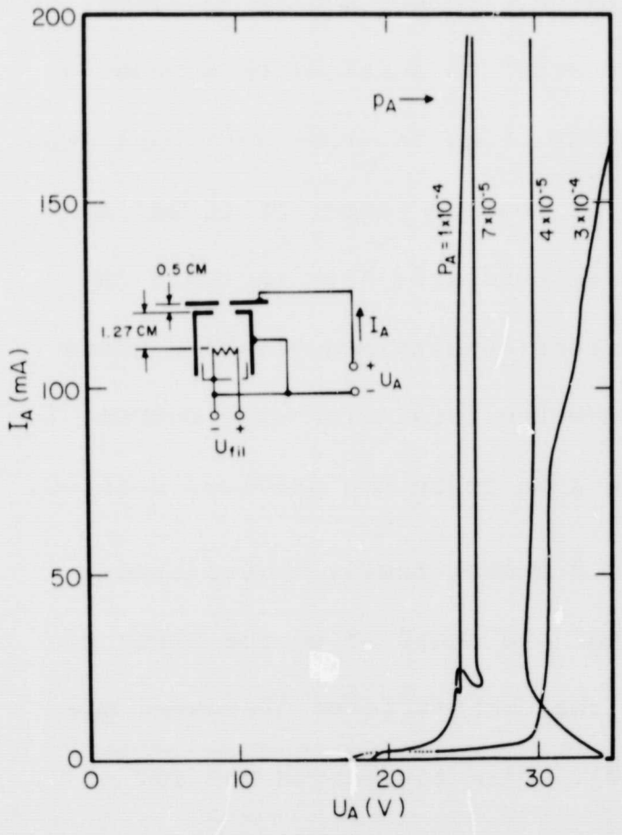

Fig. 16 Voltage-current Characteristics of Gas Discharge between Filament and Anode

negligible value. Fig. 17 shows the influence of such a biassing resistor. It is obvious that below $U_A \cong 32V$ the IE current consists only of a diffusion of electrons from filament to IE. At 32V an arc strikes ($I_A \cong 200$ mA, limited by the arc power supply). Now the electron flow to the IE is greatly increased. It is about 20 mA (10%) of the total arc current if the IE is connected directly to the filament, 7 mA (3.5%) for $R_b = 500\Omega$ and 0.3 mA (1.5%) for $R_b > 2k\Omega$. In this case nearly the whole discharge current flows to the anode. Since all the particles have to pass through the hole in the IE, the discharge is constricted to a diameter of less than 3.2 mm. Compared to the case of an arc burning between filament and IE (1.25 cm dia; see previous section) this means a constriction in cross sectional area of at least a factor of 16 and a correspondingly high increase in current density and plasma density since the total discharge current is the same as in the previous section.

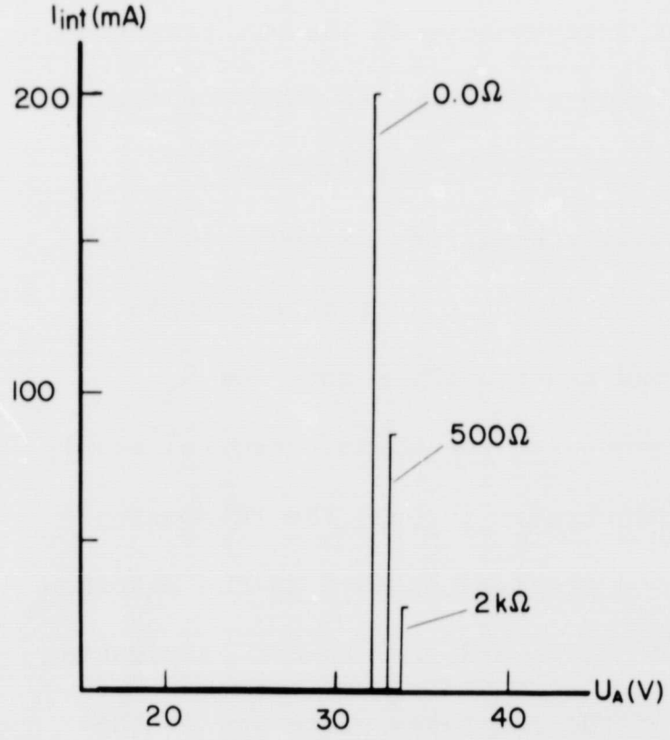

Fig. 17 Current to Intermediary Electrode versus anode Voltage

In this section it has been shown that a geometrically constricted 200 mA arc can be maintained between filament and anode at source pressures in the vicinity of 10^{-2} torr. Compared to the unconstricted discharge the arc voltage is a few volts higher ($U_A \simeq 30V$). Directly behind the ion extraction hole in the anode (Fig. 1) the current density can be estimated to $2.5A/cm^2$ and the plasma density to about 0.82×10^{11} ions/cm^3. Power

dissipation at the anode is about 60 watts.

2.1.8. Extraction of positive ions and electrons from the source.-- To measure charged particles extracted by a suitable extraction voltage U_{ex} the source extractor and collector electrodes shown in Fig. 5 are connected as shown in Fig. 18. The anode of the source is kept on ground potential so that filament and arc supplies can be kept close to ground. A power supply which is capable of delivering $\pm$ 10kV (α2mA) is connected between extractor electrode and anode. Consequently, the Faraday cage and the electrometer are operated at high voltage level. A Keitheley 601-3 battery operated electrometer is put into an insulating plexiglass box and used to measure the collector current I_c (Fig. 18).

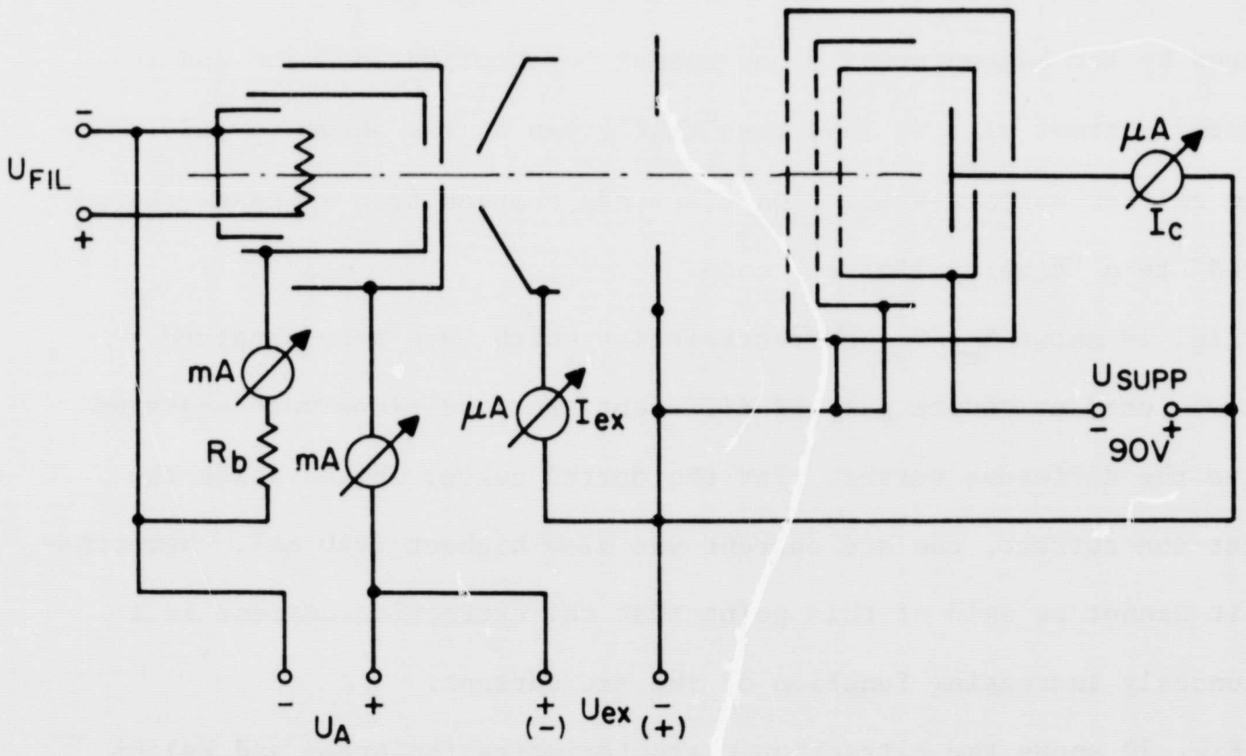

Fig. 18 Circuit for Measuring Extraction Characteristics of Unoplasmatron

Theoretically the maximum current of ions of mass M which can be extracted from a plane emitting surface of area A by a flat electrode at the potential V with respect to the emitter and a distance d apart from it is given by the Langmuir-Child Law (Ref. 7).

$$I_+ = A \frac{\sqrt{2}}{9\pi} \frac{e}{M} \frac{V^{3/2}}{d^2}$$

or

$$I_+ = 3.81 \times 10^{-11} A \frac{V^{3/2}}{d^2\sqrt{M}} \qquad [\text{amps}]$$

where V is measured in volts and M in amu.

This law is valid as long as the plasma density is such that the required ion current can be supplied by ion diffusion to the emitting surface. If the extraction value rises above a certain level the current required by the Langmuir-Child Law cannot be supplied any more and the extracted current will be less than that given by the above formula. The system emitter surface-extraction electrode changes from a "space charge limited" to a "density limited" mode.

Fig. 19 shows I_{ex}-V_{ex} characteristics which have been obtained. Argon was used as source gas and different arc conditions were adjusted to give the different curves. For the dotted curve, which yields the highest ion current, the arc current was also highest (240 mA). Nevertheless it cannot be said at this point that the extraction current is a monotonously increasing function of the arc current.

Fig. 20 shows the extraction characteristics for Argon and Helium respectively in a log-log plot. Due to the different ionization potentials of A and He the arc parameters are quite different for the two gases. Pressure arc current and filament current were adjusted however in order to

give maximum extraction current. It is obvious that both curves have a linear section with a slope of about 3/2 (dotted line) below an extraction voltage of about 300-400V. In this section the Langmuir-Child Law is obviously valid. According to the same formula the He^+ current should be about 3.3 times as high as the A^+ current whereas one reads a factor of only 2.5 from Fig. 20. A more detailed investigation has to be undertaken to explain this effect.

By reversal of the polaritites of the power supplies as indicated in Fig. 18, electrons can be extracted from the source. Fig. 21 shows extraction characteristics for ions and electrons. Note that in this case extraction current decreases monotonically with the arc current. For $I_A <$ 115 mA however, this trend reverses and below 100 mA it is impossible to strike an arc. The ion currents extracted from the same discharge

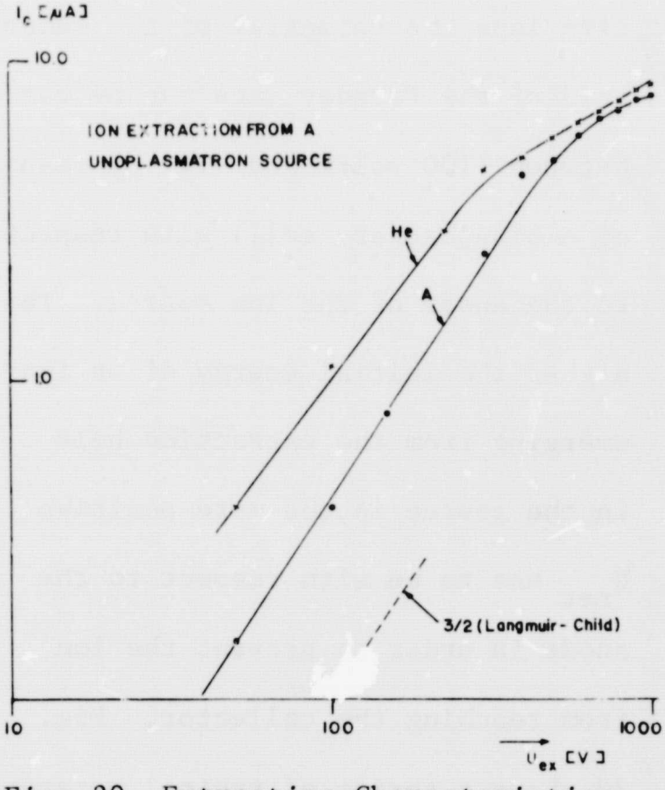

Fig. 20 Extraction Characteristics for Helium and Argon

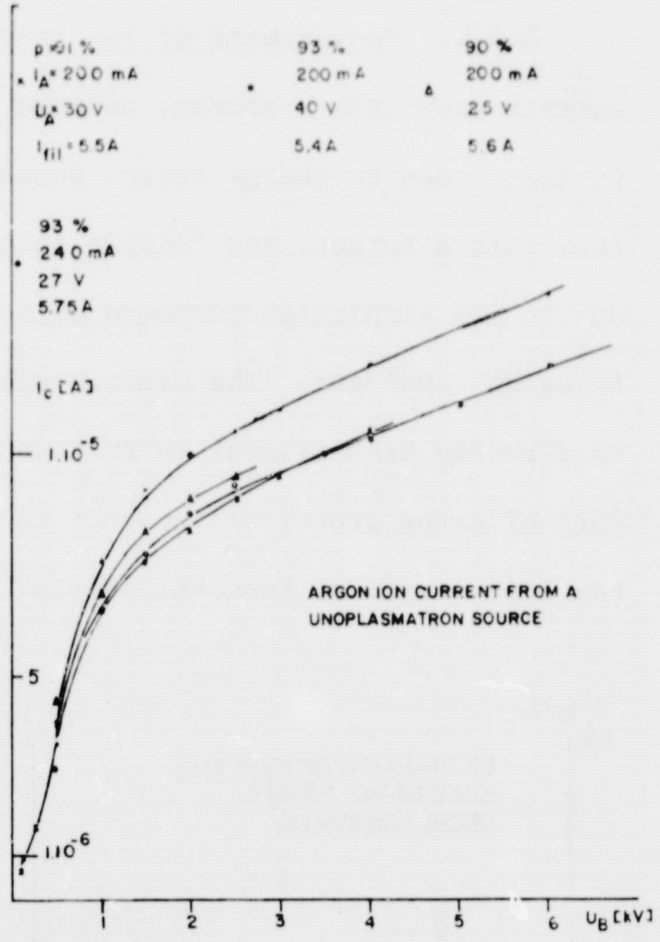

Fig. 19 Extraction of Argon Ions from a Unoplasmatron

show the same trend.

2.1.9. Measurement of ion energy distribution.--In this attempt to extract ions from a source, analyze them in a suitable analyzer according to their mass to charge ratio, focus them into a small spot and inject them into a target, the "single focusing" mass analyzer will be used due to its simplicity compared to a chromatically corrected "double focusing" analyzer. The minimum spot size obtainable with this analyzer is directly proportional to the energy width of the ion beam. It is therefore of great practical interest to investigate the energy distribution of the ions extracted from the source.

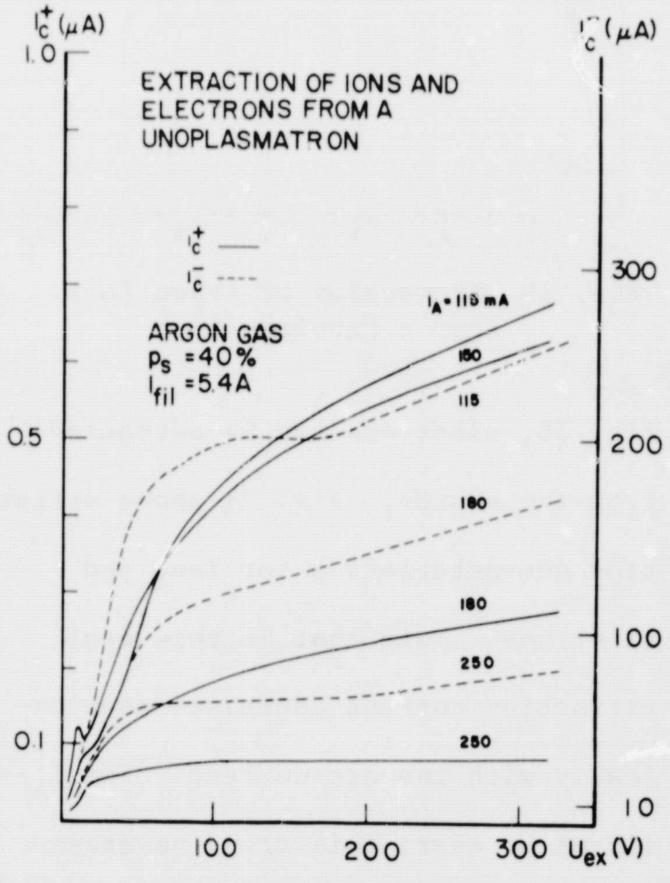

Fig. 21 Extraction Characteristics for Ions and Electrons

Fig. 22 shows the circuit used to measure particle energy distributions by the retarding potential difference (RPD) method. For positive ions the potential of the second grid of the Faraday cage can be varied between +100 volts and -9V (by means of a bias battery cell) with respect to the anode of the ion source. The higher the initial energy of an ion emerging from the extraction hole in the source is, the more positive U_{ret} has to be with respect to the anode in order to prevent the ion from reaching the collector. Fig. 23 shows a series of typical retardation

curves for different arc parameters. The percentage units of the source pressure indicated at each curve refer to Fig. 6. One can see in Fig. 23 that the ordinate values of all curves with the exception of the curve (3) are approximately proportional to each other. Curve (3) extends to much larger values of $U_{ret} + U_{ex}$ which means that there is an appreciable fraction of high energy ions present in the beam. This curve is distinguished from the others by an abnormally high arc voltage (52V, 1A). Maximum ion current

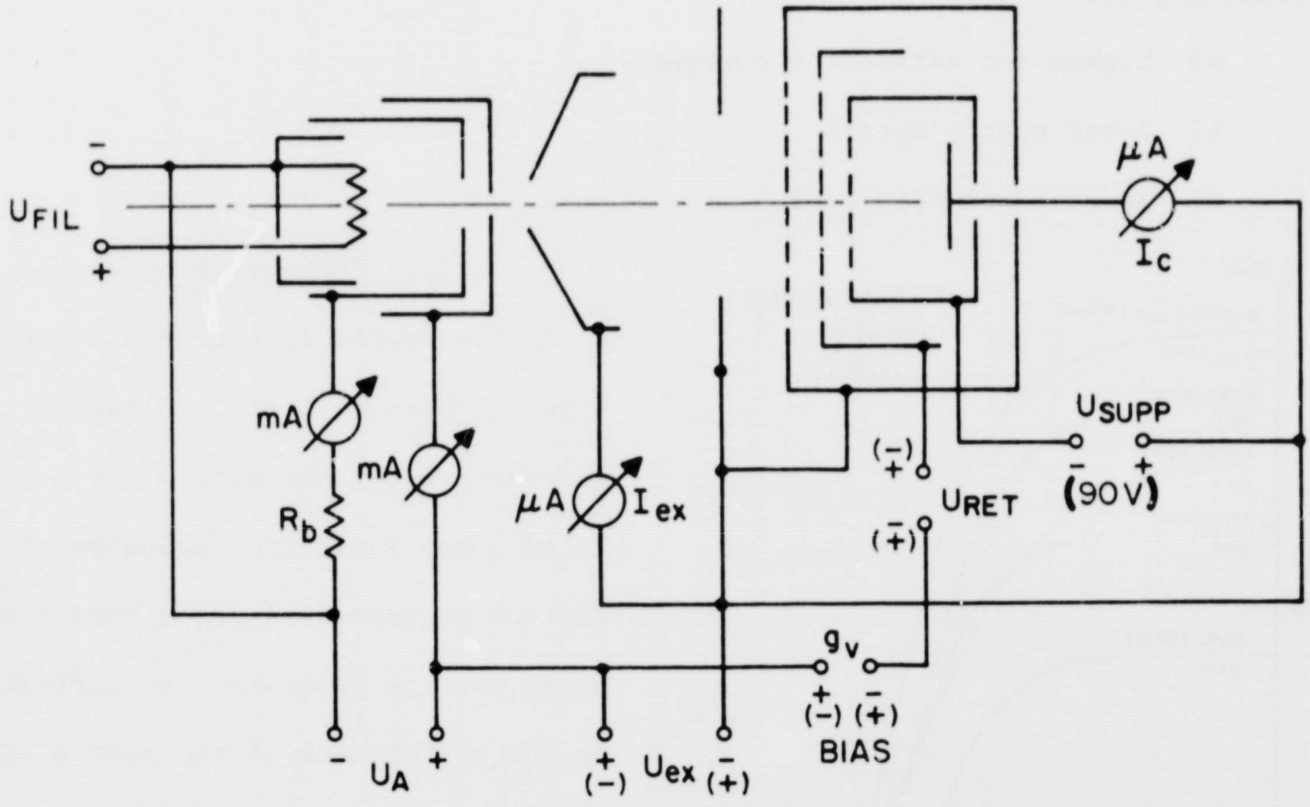

Fig. 22 Circuit for RDP Measurement of Ion (electron) Energy Distribution

is indicated by curve (5) (I_A = 140 mA, U_A = 29V). Graphical differentiation of the retardation curves gives the number of ions with an initial energy between U_{ret} and $U_{ret} + \Delta U$ (differential energy distribution). This has been done in Fig. 24 for ions and electrons. Two representative cases are shown, namely, the "high arc" case (high arc voltage $U_A \approx 50V$, high arc current > 300 mA) and the "low arc" case (low arc voltage $U_A \approx 27V$,

low arc current I_A = 110-140 mA). It is obvious that although the energy width at half height is about the same in both cases ($\Delta E_{1/2} \cong$ 17V) the 'low arc' shows a sharp cutoff of the ion emission current at about U_{ret} = 28V, whereas the 'high arc' emits an appreciable amount of ions with energies higher than 50eV. The most probable ion energy for both cases is approximately 16 eV.

It is obvious that the 'low arc' is the preferable regime for the following reasons:

a) higher ion extraction current

b) lower energy spread

c) lower power dissipation

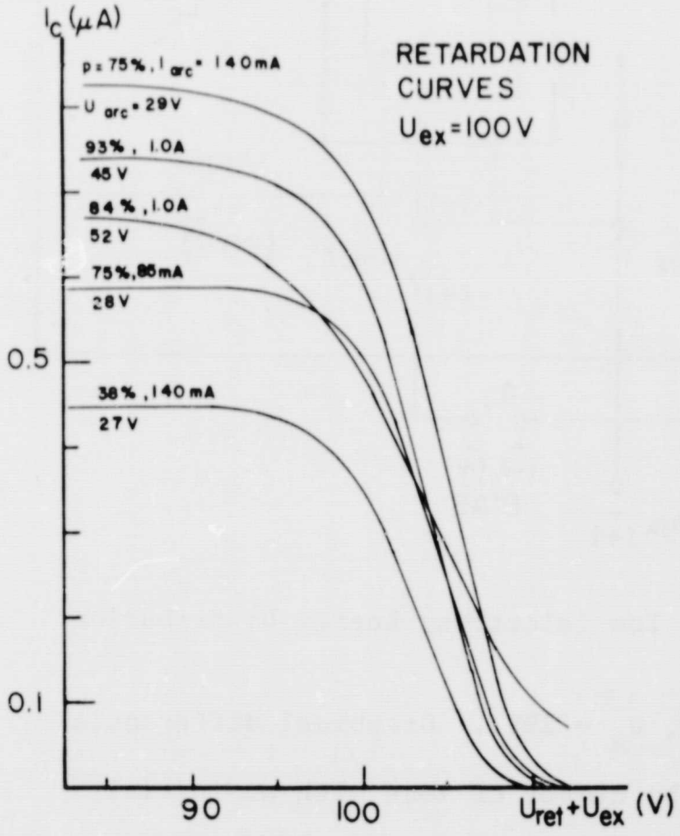

Fig. 23 Retardation Curves as Measured with the Circuit in Fig. 22.

2.1.10. Summary of section 2.1.

A gas ion source of the Unoplasmatron type has been designed and built. The purpose for building a gas source is to investigate the influence of various parameters (i.e. linear dimensions, source pressure, arc current) on the performance of the source and to be able to optimize the future metal ion source.

It has been shown that stable arc conditions can be obtained at source pressures as low as 1×10^{-2}. In this case the arc itself consumes a power of about 5 watts. Including the filament current a total power

of about 55-60 watts is dissipated within the ion source. For argon the flow of neutrals through the exit hole of the source is in the order of 0.5 µg/sec which should should make it possible to run the source for about 500 hours with a charge of 0.5 gram of a material of medium mass number.

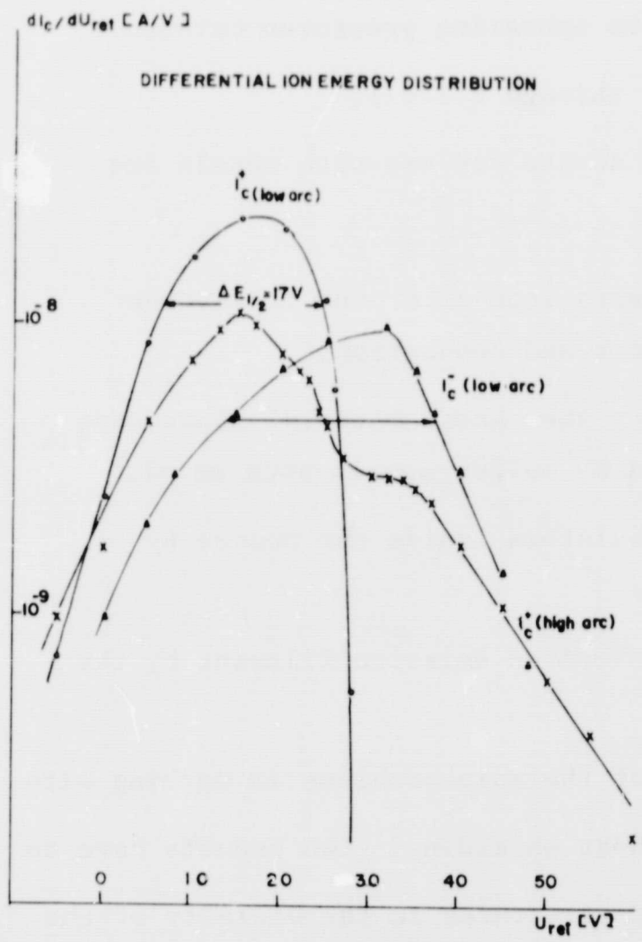

Fig. 24 Differentiated Retardation Curves (uncorrected differential ion energy distribution)

10µA of A- ions have been extracted from the source with an extraction voltage of 2 kV. (although no mass analysis of the ion beam has been undertaken so far it can be assumed that by far the largest fraction consists of singly charged ions of the gas introduced into the source.) The source efficiency (ions/neutrals emitted) is about 2-3% for Argon.

The total energy width of the extracted ion beam can be made lower than 25V under certain conditions. Two regimes of the discharge can be obtained: the 'low arc' characterized by low power dissipation, high emission current and low energy spread and the 'high arc' with high anode power dissipation, low emission current and large energy spread of the ions.

2.2. High Temperature Metal Unoplasmatron

The mechanism of a Unoplasmatron discharge remains the same whether it is sustained in an atmosphere of metal vapor or in permanent gases. Since it is our aim to produce ion beams of elements such as Mg, Pb, Ca, In, and Ga, it is necessary to reach operating temperatures between 600°K and 1500°K (ref. 8). This corresponds to operating pressures between 10^{-2} and 10^{-1} torr (see sections 2.1.7. through 2.1.9.).

The problems in adapting a gas ion source for use with metals are mainly of an engineering nature:

1) to put additional heating elements into or around the source and reduce heat losses by radiation and conduction,

2) to find a suitable container for the charge material since many materials are chemically attacked by molten metals such as Al,

3) to avoid coating of all the insulators inside the source by condensed charge material,

4) to prevent "poisoning" of the electron emission filament by the metal vapor.

2.2.1. Radiation shielding.--One of the main problems in working with high temperature structures is that of heat shielding. Two aspects have to be considered: first, to keep parts and structures in the vicinity of the ion source on low temperature, and second to minimize heat losses from the ion source surface by radiation and conduction.

According to the Stefan-Boltzmann Law a body with surface area A (in cm^2) and emissivity ε radiates away

$$\frac{dQ}{dt} = A\varepsilon \times 5.67 \left(\frac{T}{1000}\right)^4 \qquad \text{[watts]}$$

through the surface, where T is the surface temperature in degrees Kelvin.

From the dimensions of the low temperature gas source investigated during this contract we can estimate a surface area of about 25 cm^2 for the high temperature source. At an operating temperature of 1500°K the tantalum anode, which will be the outmost surface of the source has an emissivity of $\varepsilon \simeq 0.2$ so that we can expect a theoretical power loss of $\frac{dQ}{dt} \simeq 140$ watts from an unshielded source. This is assuming clean, polished, and uncontaminated Ta-surfaces. A real surface however may have an emissivity which is higher by a factor of 2 or 3 so that the power consumption increases accordingly. To achieve the same operating temperature with less power it is possible to surround the hot ion source body with closely spaced thin sheets of heat reflecting material. Energy radiated away from the heated center body is partially reflected by the innermost shield so that the temperature of the center body increases. Alternatively, the same temperature can be achieved with reduced power input into the center body. Increasing the number of shields further reduces the amount of power needed to keep the source at a certain temperature. If one assumes that the emissivities of the center body and all the heat shields are identical and independent of the temperature, the power required to keep the center body at a specified temperature above the ambient is given by

$$Q' = \frac{Q'_o}{n+1} \quad ,$$

where n is the number of shields and Q'_o the power consumption without shields (n = 0). One shield therefore cuts the power requirement by a factor of 2, 2 shields by a factor of 3, etc.

For real bodies however, the emissivity ε is a complicated function of temperature so that the shielding action is not proportional to the number

of shields. Fig. 25 shows experimentally determined ε values for clean tantalum metal (Ref. 4). For temperatures around 1500°K a straight line approximation can be used:

$$\varepsilon \cong 0.125 \left(\frac{T}{1000}\right) \quad .$$

ε values derived from this formula agree within 10% with the measured values. In the case of W the applicability of a straight line approximation has been confirmed experimentally in the Particle Optics Lab (Ref 9).

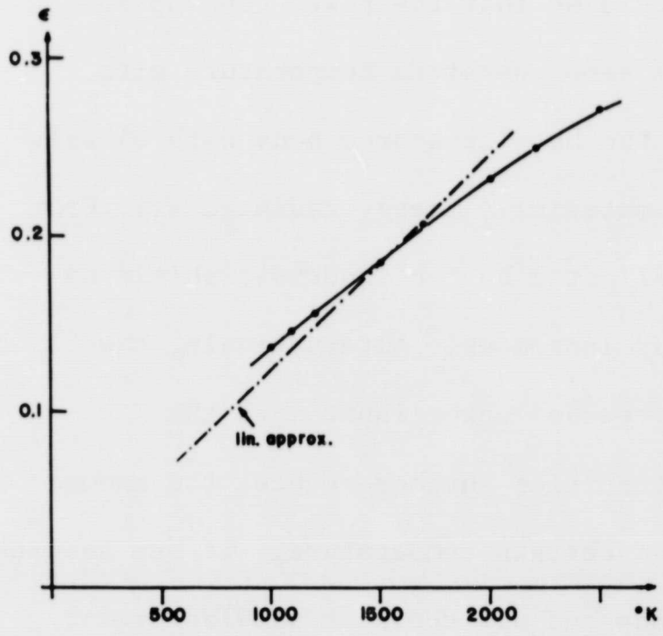

Fig. 25 Total Thermal Emissivity of Tantalum

The power radiation of tantalum can therefore be approximated by the formula

$$\frac{dQ}{dt} = 0.71\ A \left(\frac{T}{1000}\right)^5 \quad .$$

To measure the effectiveness of heat shields a scaled down model of the ion source has been constructed. It consists of a tantalum tube (one end covered) as a center body (Fig. 26). A 15 cm long 10 mil tungsten filament mounted in the inside can dissipate about 80 watts if heated by a current of about 6 amps. The current is fed via two alumina inslated 50 mil Ta-leads through the open end of the tube. Two heat shields can be pushed over the center body leaving one end of the tube unshielded. Distance between heat shields is about 25 mil. 1/8" dia holes were punched in both heat shields so that an optical pyrometer (single color L & N 8622-C) can be focused

onto the surface of the center body as well as the first shield in order to measure their respective temperatures.

If the temperature of a surface is determined by single color pyrometry, a correction has to be applied to the pyrometer reading which takes into account the varying spectral emissivity of a real body for the wavelength under consideration (red, 6530Å). Fig. 27 shows the correction as a function of the pyrometer reading. The graph has been drawn according to data given by Kohl (Ref.4)

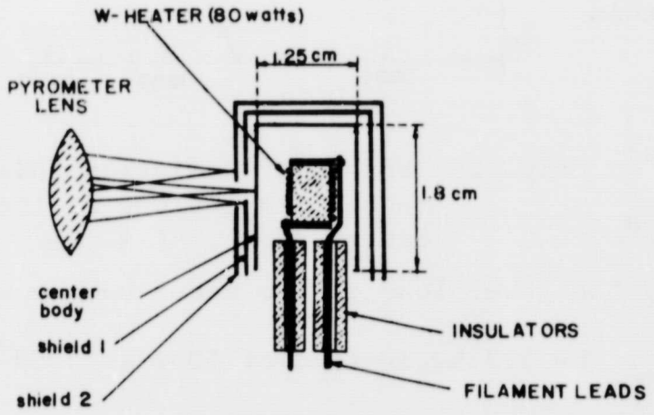

Fig. 26 Test Body for Measuring Effect of Radiation Shielding

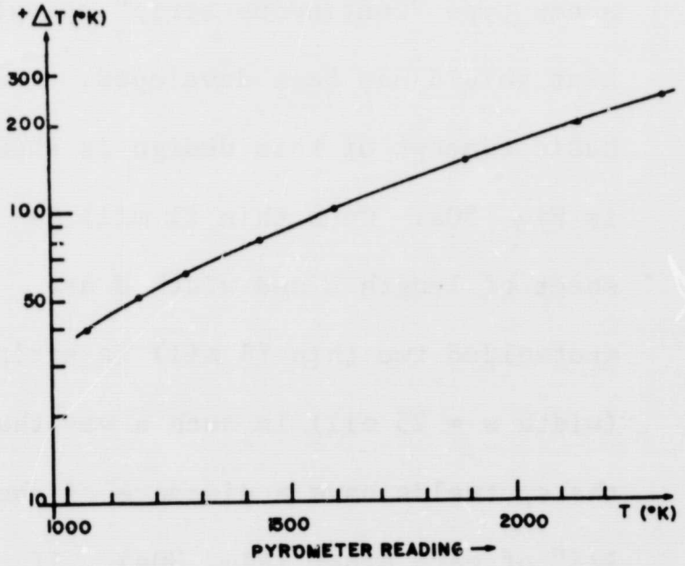

Fig. 27 Pyrometer Correction for Tantalum

Fig. 28 shows the temperature-power diagram of the test source without shield (a), with one shield (b), and with two shields (c). Notice that without heatshield the power dissipated is proportional to T^5 as expected. From the dimensions and the material properties of the test source structure one can calculate a heat loss of 84 watts at 1500°K. A further reduction by a factor of about two can be expected if the contact area between shields can be minimized by careful mechanical construction.

2.2.2 Temperature of Radiation Shields.--On the same model the temperature of the heat shields was determined pyrometrically. The results are shown in Fig. 29. As can be seen the temperature drop between opposite surfaces is approximately 200°C at 1500°K. With a shield spacing of 25 mil ≅ 0.6 mm this gives a temperature gradient of about 3.3×10^3 °C/cm. If the same temperature gradient had to be sustained by a solid thermal insulator (i.e alumina) the power loss of the model source would be 2.7 kw instead of 50 w at 1500°K.

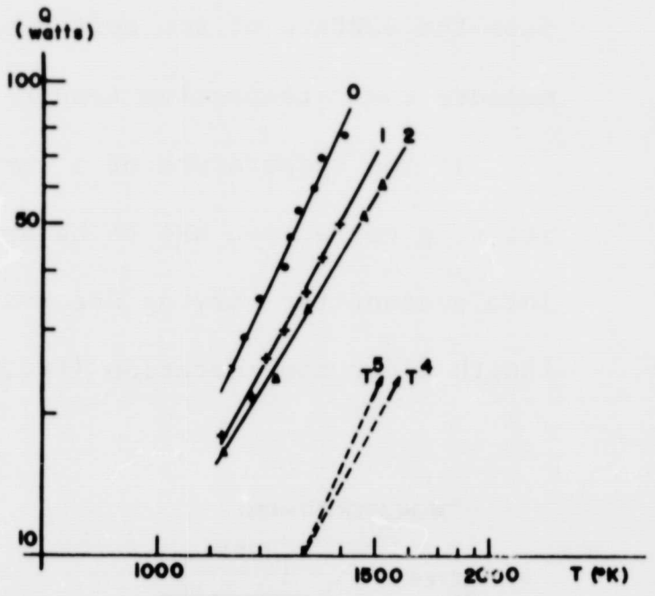

Fig. 28 Effect of Radiation Shields on the Temperature of the Center Body in Fig. 26

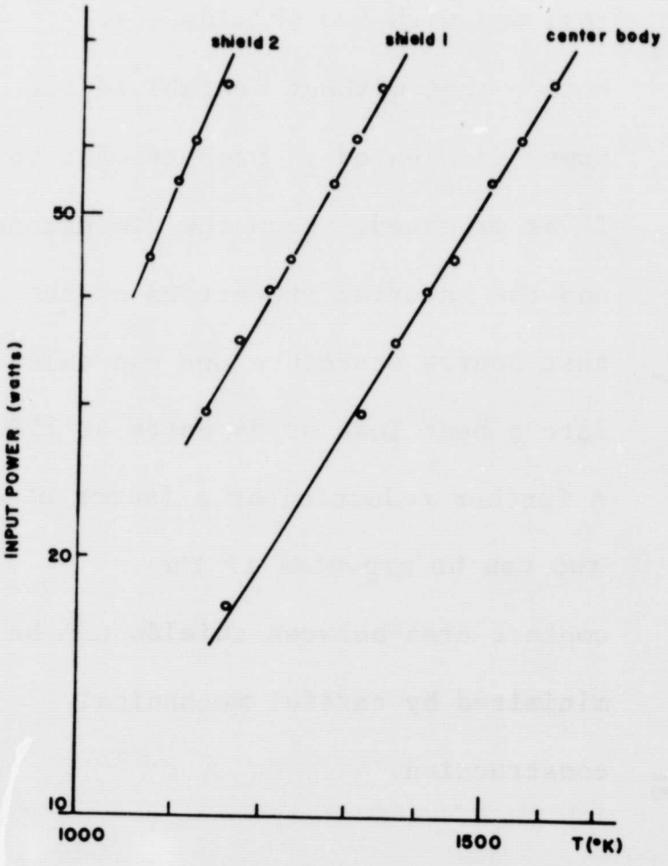

Fig. 29 Temperature of the Radiation Shields in Fig. 26

2.2.3. Spiral heat shield.--Based on the measurements on an array of individual cylindrical heat shields a new type "continuous strip" spiral heat shield has been developed. The basic concept of this design is shown in Fig. 30a. On a thin (1 mil) Ta sheet of length L and width H are spotwelded two thin (1 mil) Ta strips (width w = 25 mil) in such a way that the spotwelds have a distance of about 1/8" of each other (Fig. 30a). If this sheet is rolled around a cylindrical mandrel of radius R with the

strips on the inside, a multilayer spiral body is formed, the cross section of which is shown schematically in Fig. 30b. The Ta strips have warped into a wave-like pattern which keeps consecutive spiral layers at a well defined (but very small) distance from one another.

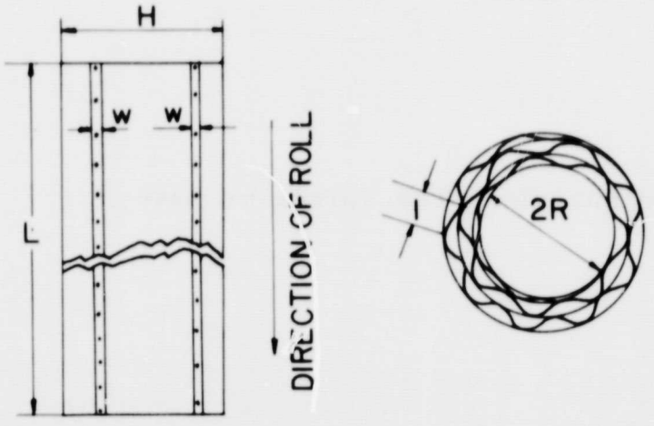

Fig. 30 "Spiral" Radiation Shield

Heat transfer in such a system occurs by radiation between consecutive spiral layers, by conduction along the whole length of the rolled-up sheet, and by conduction between the adjacent layers across the warped Ta strips. A simplified treatment of the conductive contribution to the heat transfer is outlined below.

t.....thickness of Ta foil and strips

w.....width of Ta strips

N....number of spiral turns

R.....average spiral radius

n....number of warps per turn

η.....heat conductivity of Ta

ΔT...Temperature difference between the outside and the inside of the spiral structure

δT...average temperature difference between consecutive spiral layers

The heat conduction Q_s along the rectified spiral is given by

$$Q_s = \eta Ht \frac{\Delta T}{L} = \frac{\eta Ht \Delta T}{2R\pi N} \qquad (1)$$

assuming a constant temperature gradient along the spiral surface. From Fig. 29 of section 2.2.2 one sees that there is an almost constant temperature difference (at least between the three hottest surfaces). Therefore our assumption seems to be a good approximation.

The heat conduction across the warps $\dot{Q}_w$ can be written as

$$\dot{Q}_w = 2\eta \cdot 2wtn \frac{\delta T}{\ell} \tag{2}$$

where ℓ is half the length of a warp. If the distance between layers is small, ℓ can be approximated by $\ell \cong \frac{R\pi}{n}$. Therefore,

$$\dot{Q}_w = \frac{4\eta wtn^2 \delta}{R\pi} \tag{3}$$

Assuming again a constant temperature gradient along the spiral we have $\delta T = \Delta T/N$ and finally,

$$\frac{\dot{Q}_w}{\dot{Q}_s} = \frac{8wn^2}{H} \tag{4}$$

showing that warp conduction is predominant for $w/H > 10^{-2}$.

The spiral radiation shield for the high temperature ion source described in 2.2.4. had the dimensions

$R \cong 1.0$ cm	$w = 0.1$ cm
$H = 3.0$ cm	$N = 8$
$t = 2.54 \times 10^{-3}$ cm	$n = 12$

With a value of $\eta = 0.71$ watts/^{o}C. sec. cm and an operating temperature difference $\Delta T = 1000^{o}$C the results are

$$\dot{Q}_w = 4.1 \text{ watts}$$

$$\dot{Q}_s = 0.026 \text{ watts}$$

Due to the many contact points between layers, the effectiveness per layer of this type of shield is not as high as that of accurately built cylindrical shields. However, by tightly winding and by spacing the spotwelds appropriately,

layers can be reliably spaced 5-7 mils apart. Therefore the heat resistivity per unit volume of the spiral is far superior to an array of individual cylindrical shields. The extreme simplicity in manufacturing such a spiral renders it useful in the high temperature metal ion source. As is further described in section 2.3.1. the spiral shield resulted in a power reduction of at least a factor of 3 at operating temperatures $> 1000^{o}K$.

2.2.4. Constructional details of the high temperature Unoplasmatron-- An overall cross sectional view of the high temperature ion source is given in Fig. 31. The discharge volume itself is formed by the Ta-anode (12) and (21) and by the Ta feedthrough plate (15). The components situated in the discharge volume itself are shown in Dwgs # 32 and 34 (Appendix A). A W-filament (Dwg #35) is spotwelded to two of the Ta leads (23 in Fig. 31). An electron repeller plate is spotwelded to a third lead. The intermediary electrode (Ta) is pushed into two other leads which have been slotted for this purpose (see Dwg #32, Appendix A). A heater element (Dwg #36, Appendix A) is placed around the intermediary electrode. The intermediary electrode is centered and spaced inside the anode cavity by three alumina insulators (19) (Dwg #34) pushed over three mounting straps (Dwg #36). Gases can be fed into the source volume by means of an optional Ta tube (Dwg #34).

Electrical connections (23) lead into the discharge volume and are electrically isolated against the anode (15) and (21) by ceramic insulators (24). To prevent vapor from leaking out of the source cavity, the Alumina ceramic tubes (24) are press fitted into the 1 mil undersized holes in (15) and the Ta-wires (23) are warped by making crosswise indentations with a wire cutter before pressing them into the insulators (24). A tight fit between the removable anode cap and the feedthrough plate is produced by

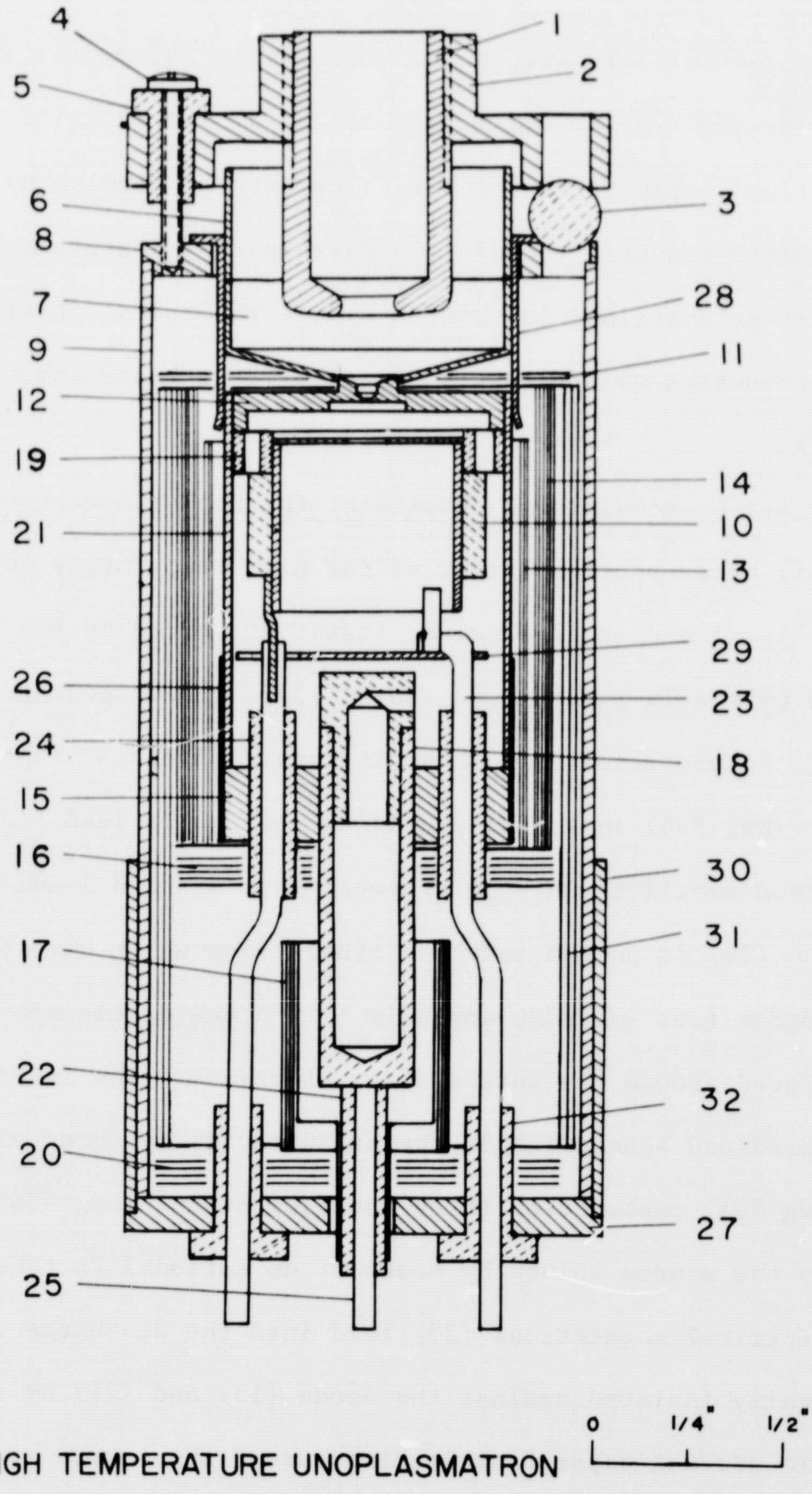

Fig. 31 High Temperature Unoplasmatron; Assembly Drawing

two layers of a 1 mil Ta foil (26) wound tightly around both and spotwelded to the feedthrough plate. The oven (18) with a volume of 0.25 cm^3 is machined from Boron Nitride and pushed through a 1/4" diameter hole in the center of the feedthrough plate. It is heated by 5-6 turns of a Ta-strip (1 mil x 25 mil) wound tightly around its outside (see Dwg #21 and Fig. 32). The spiral type heat shield (17) reduces radiative heat losses from the oven and the heater. The shielding assembly (16) minimizes radiative transfer from the discharge chamber to the oven and its surrounding heat shields. The current loop for the oven strip heater is formed by the contact wire (25), the heater strip itself, the heat shields (17), and the source housing (9).

The anode cylinder is surrounded by spiral heat shields (13 and 14) and a plane 3-layer shield (11). Ions are extracted through a hole in the center of the anode front plate (12). The plasma penetrating through the hole is allowed to expand onto a cuplike structure (see Dwg #1, Appendix A). The edge of this expansion cup, together with the anode cone (7), forms one equipotential surface of a Pierce extraction geometry. The other electrode is the"extraction electrode" (1). This electrode is machined from Ta and insulated against anode potential by means of three alumina balls (3). A thread cut into the extraction electrode (1) and its support (2) allows adjustment of the spacing between the anode and the extractor. The anode is centered and spaced by three brackets and distance pieces (28). The source structure is mounted in a two piece stainless steel housing (9), (27) and (30), held together by a temporarily spotwelded strap. Electrical connection to the extraction electrode is made by a stainless steel wire fed through a ceramic tube mounted to the outside of the source housing

(Dwg #37, Appendix A).

The inside of the source volume is shown in Fig. 33. The intermediary electrode with its surrounding heater assembly and contacts are clearly visible. Fig. 34 shows the ion source with oven and heat shield in place. On top of the structure part of the expansion cup and Pierce-cone is visible. A total view of the fully assembled ion source is given in Fig. 35. It has been mounted on a $1\frac{1}{2}$" nominal VARIAN blank flange. Total length from the top of the extraction electrode to the bottom of the flange is 4 3/4". The diameter including the insulator for the extraction electrode is 1.30", just clearing the base of a VARIAN 1 1/2" rotable flange insert. To conveniently mount the ion source on existing facilities (High voltage accelerators, Implantation systems) and at the same time to carry off the heat produced by the source, a vacuum tight housing has been constructed (Dwgs #23 to 28, Appendix A). Fig. 36 shows the vacuum housing with the source attached to it. If the source is operated near maximum temperature, a small fan (ca. 15-20 cf/m) should be mounted on-axis with this housing.

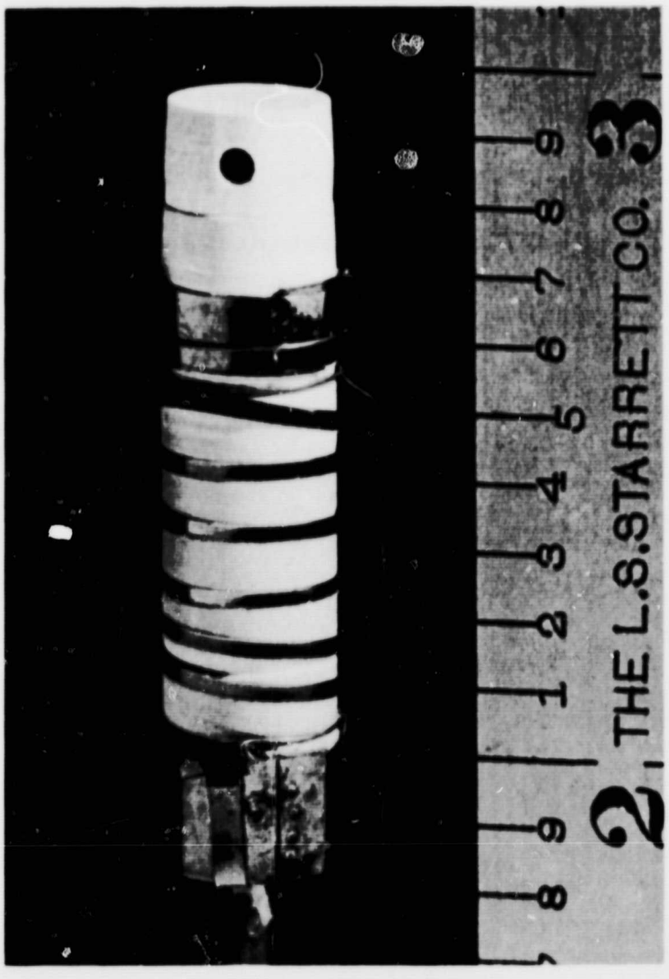

Fig. 32 High Temperature Unoplasmatron, Oven

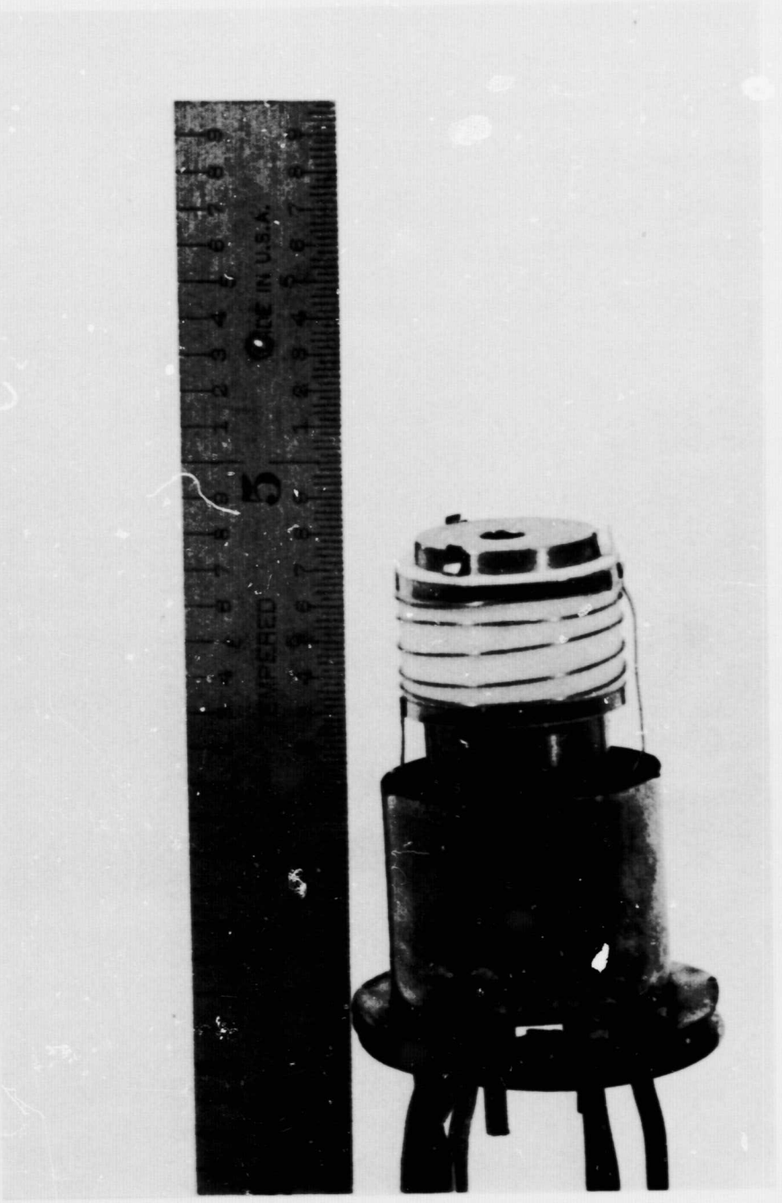

Fig. 33 High Temperature Unoplasmatron, Anode Removed

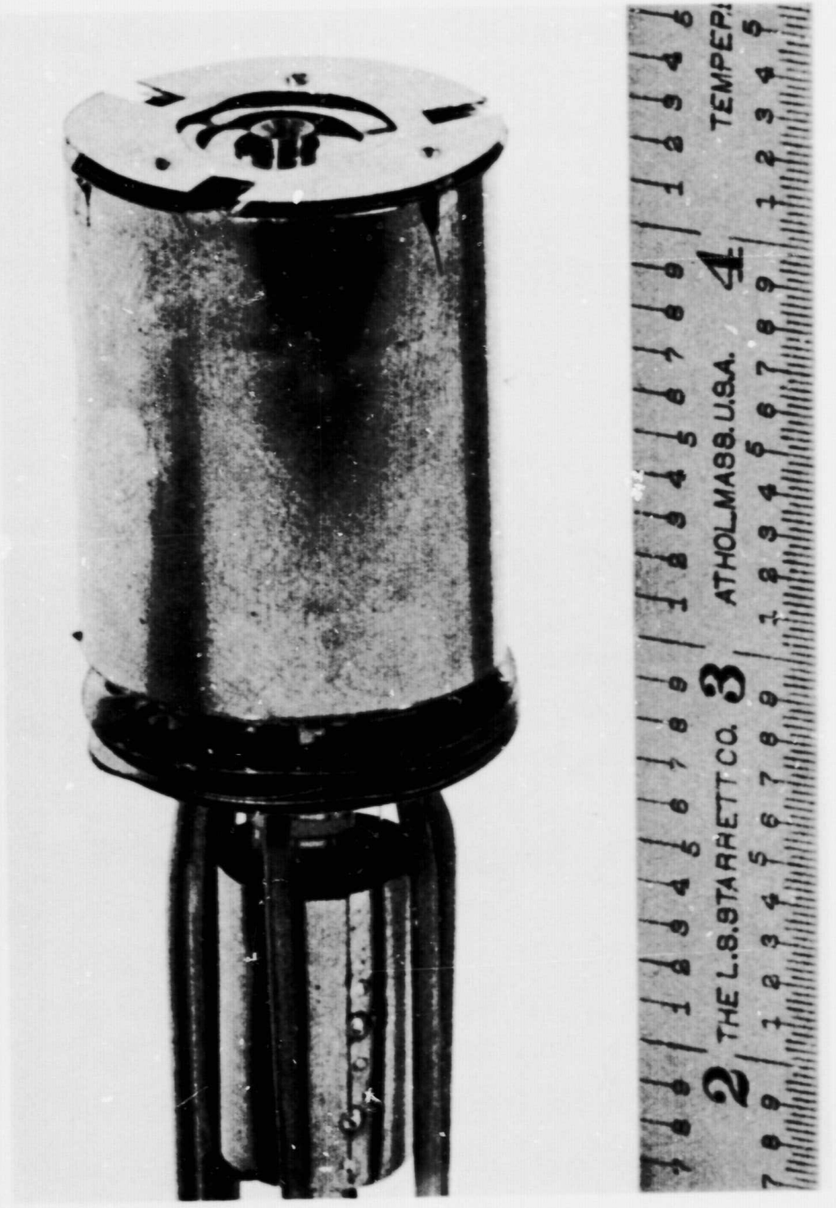

Fig. 34 High Temperature Unoplasmatron Anode and Heat Shields in Place

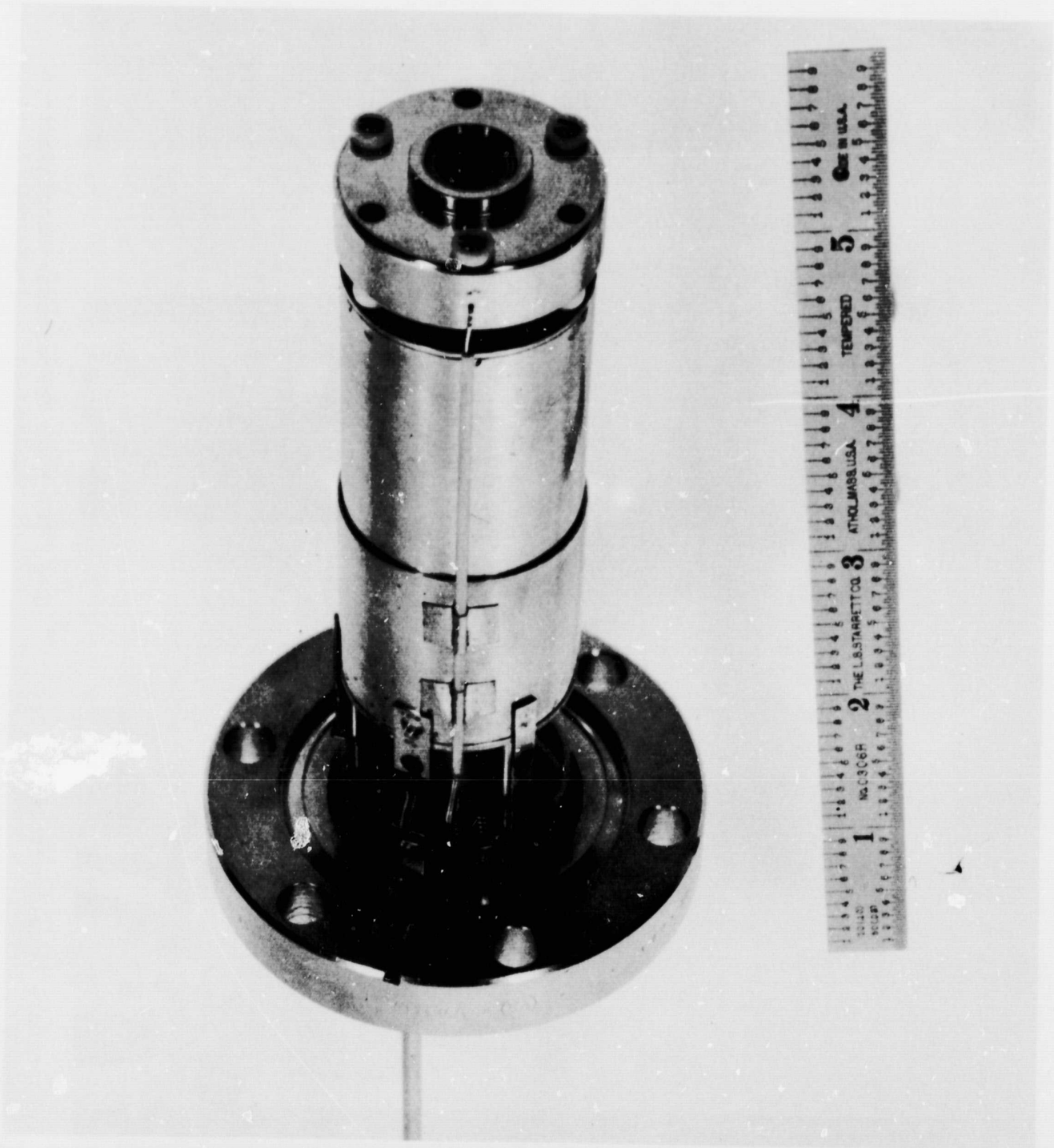

Fig. 35 High Temperature Unoplasmatron, Fully Assembled

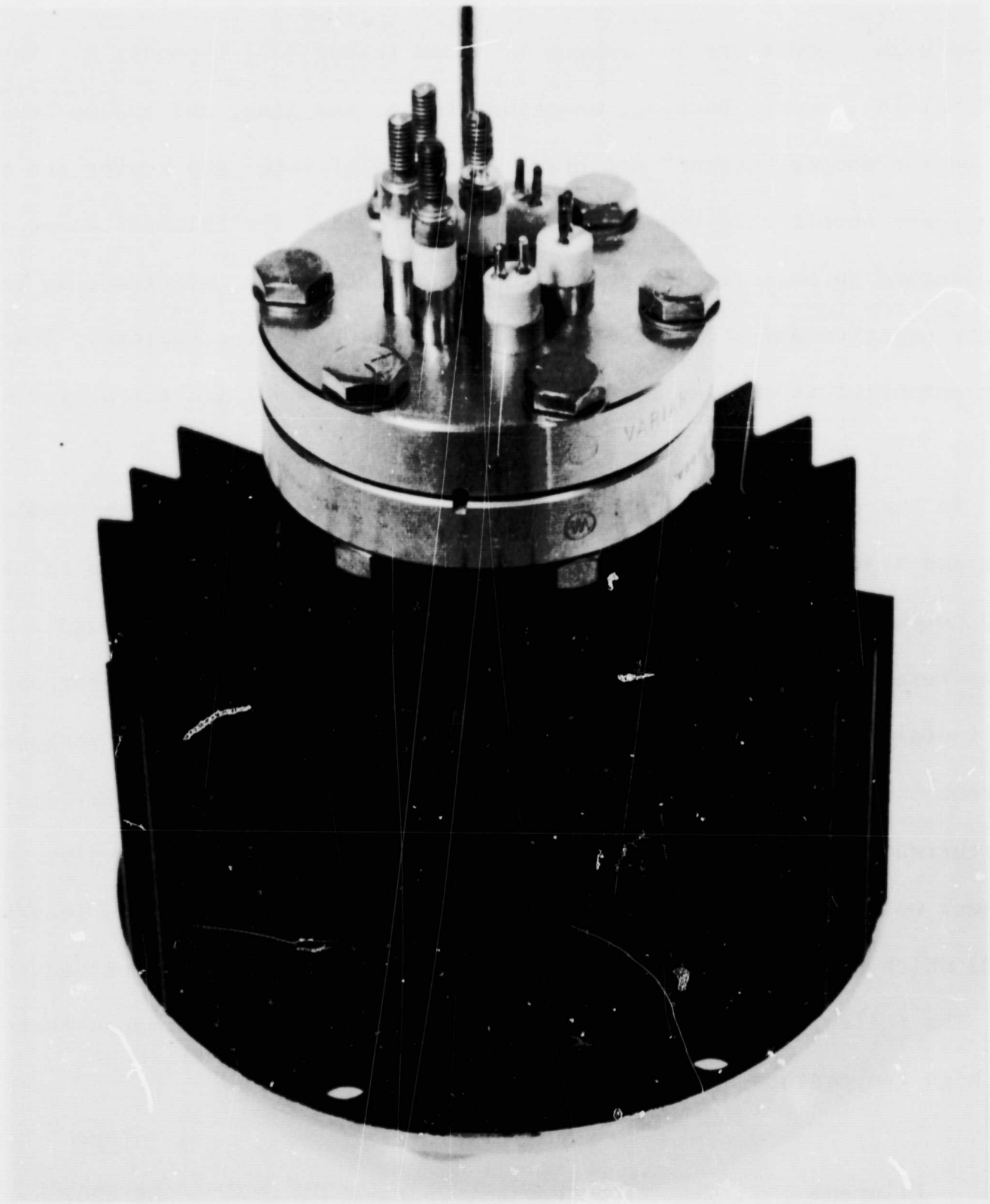

Fig. 36 High Temperature Unoplasmatron, Mounted in Vacuum Housing

2.2.5. Electrical circuit.--The basic circuit diagram for the operation of the high temperature ion source is shown in Dwg #33, Appendix A. The anode, heat shields, source housing, mounting flange, gas line, and vacuum housing are on ion source "ground" potential. One end of both the heater and the oven power supplies is connected to source ground. The filament power supply is floating on negative arc potential. The intermediary electrode is connected to the negative end of the filament via a 5K self biasing resistor. The extraction potential is applied between anode (source ground) and extraction electrode.

In the present work, current regulated DC power supplies are used as oven and heater supplies. In this arrangement a fairly repeatable relationship between power supply setting and source temperature is observed. It seems feasible however to drive oven and heater with AC power (autotransformers) and install a suitable temperature monitoring device. Since the extracted ion current is strongly dependent on the arc current (see section 2.1.7.), the arc current should be derived from a current stabilized power supply. In the present work the arc supply has a current regulation of 0.02% (no load/full load) which seems to be more than adequate for the elements processed so far.

The following power supplies were used during the performance tests of the high temperature source:

	Manufacturer	Type
Filament	Hewlett-Packard	HP 6207
Arc	Hewlett-Packard	HP 6207B
Oven	MIT built	15V/2A
Heater	Perkin Eng. Corp.	M60V
Extraction	DEL electronic Corp.	DEL 10HPT11

2.3. High Temperature Unoplasmatron Performance

2.3.1. Thermal characteristics.--A series of measurements were taken to obtain the temperature-power input relationship of the high temperature source. For this purpose two Pt-Pt/Rh (13%) thermocouples were inserted into the source structure: the first directly into the extraction cup of the anode and the second in the interior of the oven through a small hole drilled specially for that purpose. The readings of both thermocouples gave a lower limit to the true equilibrium operating temperatures for anode cavity and oven interior; the anode TC was lower because the expansion cup is the only unshielded part of the anode front (see Fig. 31) and therefore is colder than its surroundings and the oven TC was reduced because the oven heat shield had to be shortened in order to make room for the TC. Fig. 37 gives the temperatures of expansion cup and oven with and without the anode heat shield installed as a function of the total power input (filament and heater). The oven heater was not used in this series so that the measured oven temperatures were due mainly to heat conduction. At maximum operating temperature (1500^{o}K) a small amount of additional oven power (18 watts) was sufficient to equalize source and oven temperature.

2.3.2. Argon experiments.--To compare the performance of the high temperature version of the Unoplasmatron with the previously built gas Unoplasmatron (section 2.1.8.) Argon gas was fed into the high temperature source via a metering valve. The heat shields (11 and 13 in Fig. 31) were removed to keep the temperature at a value comparable to the operating temperature of the gas Unoplasmatron. Source pressure could not be measured directly but gas dynamical considerations show that the relationship between the source pressure and the vacuum chamber pressure can be described very closely as in Fig. 9.

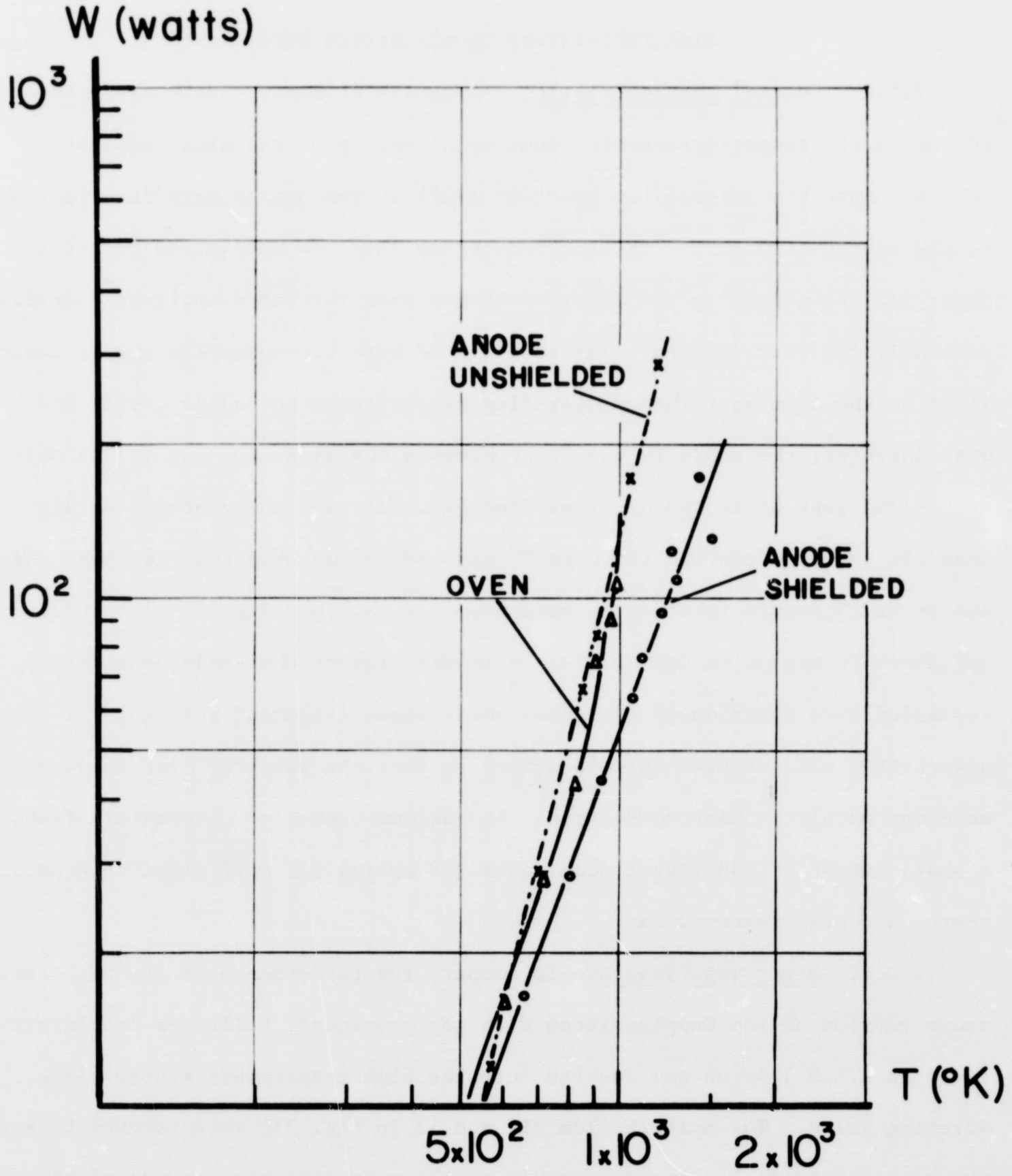

Fig. 37 Temperature of High Temperature Unoplasmatron versus Power Input

The extracted ion current was measured in a setup indentical to the one shown in Fig.18.

After optimization ofthe extraction current the following arc parameters were measured:

I_{fil} = 5.0 A $\quad$ I_{Arc} = 240mA $\quad$ $p \cong 6 \times 10^{-3}$ torr

U_{fil} = 14.3V $\quad$ U_{Arc} = 70V

The I_{ex}-U_{ex} characteristic is shown in Fig. 38. If the arc current is set to zero (no arc burning) a residual extraction current I_{ex} of $\approx$ 0.17μA is measured at U_{ex} = 2KV. This can be attributed to surface ionization of alkaline impurities of the Ta anode and extraction cup. No mass separation was performed prior to current measurement. However, if the Argon supply is shut off, I_{ex} is reduced to about 0.17 μA at 2KV which is the same value previously attributed to surface ionization. Taking this background current into account, the extraction characteristics of the low temperature (Fig. 21) and high temperature (Fig. 33) Unoplasmatron are very similar.

2.3.3. Lead experiments--For the Pb-run the heat shielding was installed again and the oven was filled with ca 0.15g of Pb metal. It was found that the best results can be obtained if the heater filament is not used and all the power is supplied by emission filament, arc, and, if necessary, oven. The U_{extr}-I_{extr} characteristic and the arc parameter for a particular run are given in Fig. 39. An increase in the arc current causes the extraction current to increase as well. Increasing the oven power has the same effect. Readjustment of the emission filament current is the simplest way to obtain stable discharge conditions if other arc parameters are varied. Fig. 40 shows the dependence of total extracted ion current on oven heater power for two different arc current settings. Current can obviously be extracted from the

source (with normal arc pararmeter prevailing) with no oven power at all. This is due to an inhomogeneous temperature distribution in the oven which causes the anode side to be hottest and the rear end coldest. If the arc current is set to zero a background ion current of ca 0.2μA at V_{extr} = 1KV is measured. Again this is interpreted as surface ionization of impurities contained in the Ta building material.

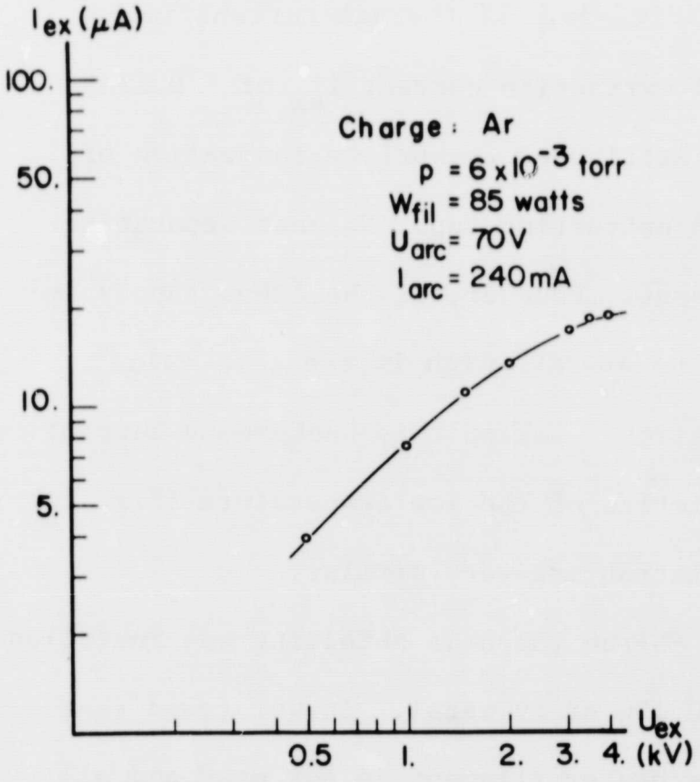

Fig. 38 High Temperature Unoplasmatron; Extraction Characteristics for Argon

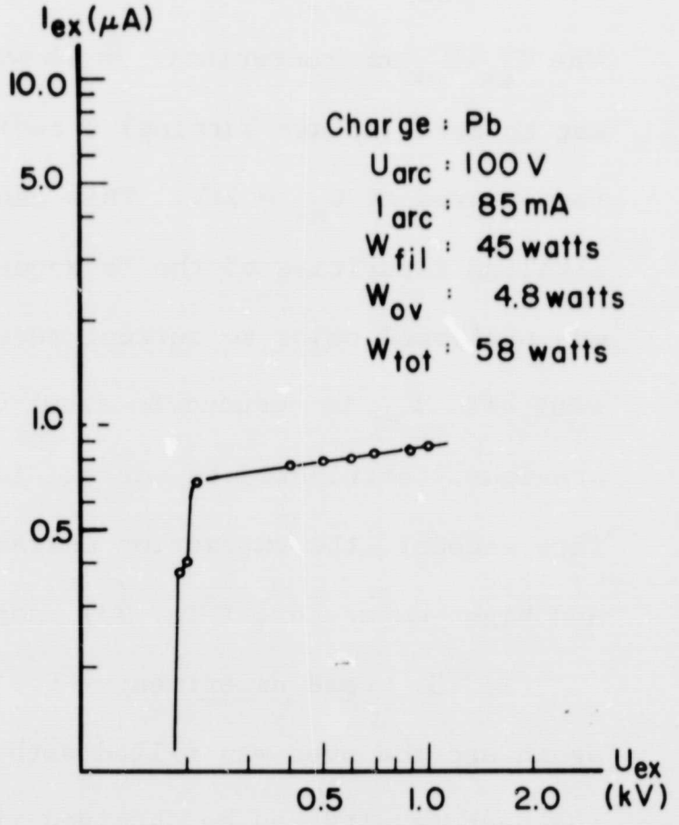

Fig. 39 High Temperature Unoplasmatron Extraction Characteristics for Lead

If the source is recycled (cooled to room temperature) and restarted four times, contamination of the insulators (Fig. 31) makes it difficult to maintain the starting voltage for the arc (150 volts). Sandblasting of the insulators makes the source ready to operate again for three more cycles. After this the insulators must be exchanged. In this run the source totaled

an operating time of about 32 hours after which nearly half of the original Pb charge still remained in the cold portion of the oven.

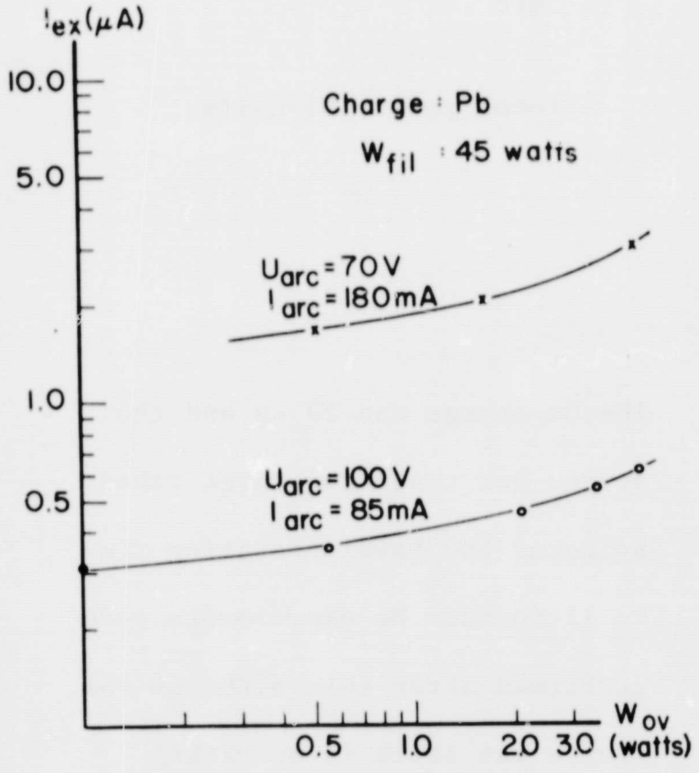

Fig. 40 High Temperature Duoplasmatron; Extracted Lead Current Versus Open Power

2.3.4. Gallium experiments.-- A complete discussion of the Ga results is difficult without mass analysis of the ion beam since at least three factors contribute to the extraction current:

a) surface ionization of alkaline impurities contained in the Ta on the Ta surfaces of the anode and the expansion cup as well as on the filament. (Since the work functions of polycrystalline Ta and W are 4.1eV and 4.55eV respectively, most alkalais should be completely ionized even at low temperatures.)

b) Surface ionization of Ga (Ionization potential I ≅ 5.9eV) at the emission and heater filaments and Ta surfaces of the discharge volume

c) Ionization of Ga in the arc discharge

By setting the arc current to zero the contribution of item (c) could be singled out. This fraction (Fig. 41, curve 3) can very likely be attributed to Ga ions alone.

To single out the contribution of Ga to the background current (no arc burning) more detailed analysis is required, preferably including mass analysis of the beam.

The parameters of the Ga-run were:

Filament:	I_f = 4.5A	I_{arc} = 170mA
	U_f = 12.5V	U_{arc} = 90V
Heater:	I_h = 3.2A	total power 101 watts
	U_h = 8.5V	
Oven:	I_o = 0.8A	
	U_o = 5V	

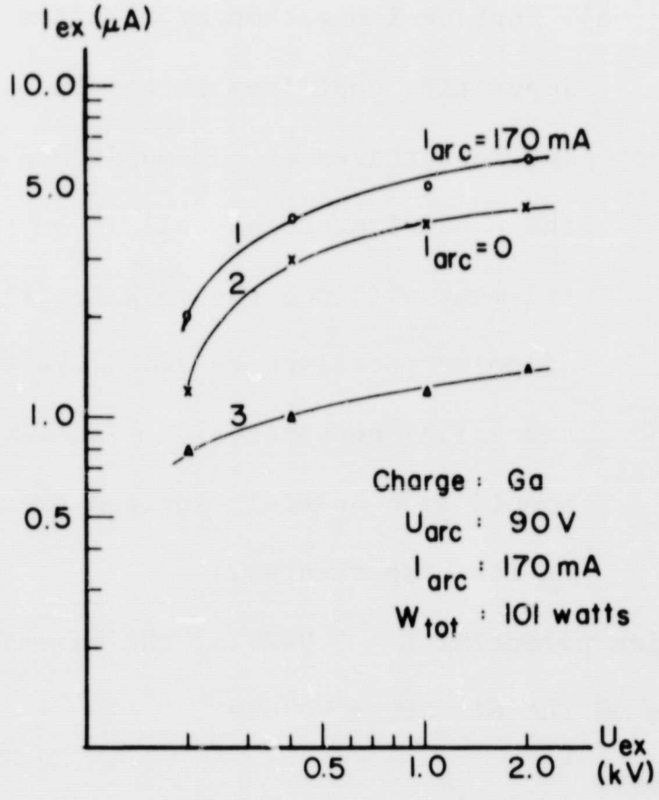

The Ga charge was 50 mg and the source was restarted three times bringing the total operating time to 11 hours. No experiments were performed after this although the source was still in operating condition.

Fig. 41 High Temperature Unoplasmatron; Extraction Characteristics for Gallium

3. MASS SEPARATION AND FOCUSING SYSTEM

In order to bombard the surface of a solid species in a 2-dimensional pattern with a spatial resolution of the order of microns, a suitably demagnified ion optical image of the ion emitting area (i.e. exit hole area of

the ion source) has to be projected onto the solid surface with a mass analyzing stage incorporated in the imaging system. Since the ion species selected for bombardment may constitute only a fraction of the total beam extracted from the ion source (section 2.2.) it is advisable to perform mass separation early in the imaging process rather than carry all the unwanted species through the system and risk contamination of apertures. It is therefore proposed to arrange the mass analyzer stage directly following the extraction-acceleration system described in 2.2.4. Keeping the simplicity of design in mind, the demagnifying stage will most conveniently consist of a one or a multi-stage system of rotationally symmetric electrostatic lenses. Given this fact, stigmatic focusing is required from the mass analyzer. A theoretical treatment of the focusing properties of a new class of such analyzers is given below. Based on these results the basic parameters of a low energy ion bombardment system capable of producing spot sizes of the order of a micron are given.

3.1. Stigmatic Focusing Mass Analyzer

The focusing properties of a cylindrically symmetric magnetic field which can be describee by the equation

$$H = \frac{C}{r} \tag{3.1}$$

have been investigated. In this equation H is the field intensity, r is the distance fron the axis of symmetry, and C is a constant of proportionality. Such a field can be obtained by using plane inclined pole faces. The case of a symmetric magnetic sector-field with arbitrary sector angle ϕ_m, straight boundaries, and perpendicular beam entrance and exit (see Fig. 42) was treated. Special cases of this general arrangement have been reported (Refs. 10, 11, 12).

If ions emerge from a point source S on the virtual intersection line

of the pole pieces a certain value for the particle momentum can be found for which the beam is focused at an image point I. The focusing is stigmatic (meaning a point is focused into a point and not into a line as in most magnetic analyzers). This advantage, together with the fact that plain pole faces are easy to machine and do not require critical adjustments, makes it desirable to investigate this configuration closely and compare it with other mass analyzing systems.

3.1.1. First order design parameters.--We define a dimensionless measure K for the momentum to charge ratio of the particle as

$$K = \frac{p}{qC} \tag{3.2}$$

p.....momentum of the particle

q.....charge of the particle

The condition for stigmatic focusing in a sector with deflection angle $\phi_m = 2\phi$ is

$$K[K\sin^2\phi e^{-K\cos\phi}\ I(K,\phi) + \sin\phi\cos\phi + \cos\phi\ e^{-K\cos\phi}\ I(K,\phi)] - \sin\phi = 0 \tag{3.3}$$

$$\text{where } I(K,\phi) = \int_0^{\phi} \cos\psi\ e^{K\cos\psi}\ d\psi\ . \tag{3.4}$$

Equation (3.3) obviously has to be solved numerically in order to find the value of K for stigmatic focusing. The result is given in Fig. 43.

Once the value of K is found the dimensions of the trajectory are determined. We find for the maximum distance r_m from the axis

$$r_m = L\sin\phi\ e^{K(1 - \cos\phi)} \tag{3.5}$$

where L is the "object distance" (Fig. 42) which is equal to the "image distance".

The distance $\overline{AB}$ (Fig. 42) which determines the size of the pole faces is found to be

$$\overline{AB} = 2KL \sin\phi \; e^{-K\cos\phi} I(K,\phi). \tag{3.6}$$

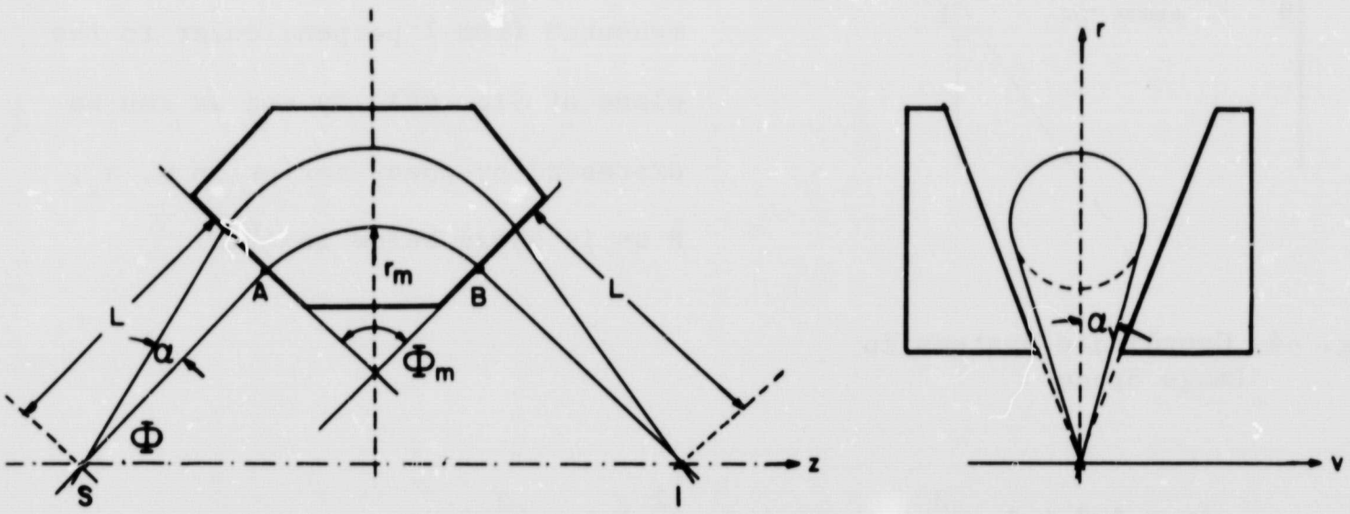

Fig. 42 Coordinate System for Wedge Magnets

The object-image distance $\overline{SI}$ is given by

$$SI = 2L \; (K\sin\phi \; e^{-K\cos\phi} \; I(K,\phi) + \cos\phi) \tag{3.7}$$

Fig. 43 shows K, $\frac{\overline{SI}}{r_m}$ and $\frac{L}{r_m}$ as functions of ϕ_m.

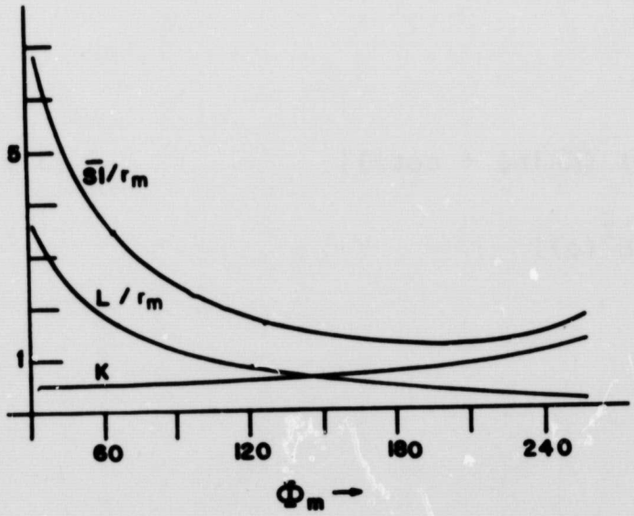

Fig. 43 First Order Parameters of Wedge Magnets

3.1.2. Second order aberrations.-- Let us define a rectangular coordinate system (x, y, z) in the image space (Fig. 44). A particle which starts from the source point S, with angular displacement opening α, α_z (see Fig.42) against the median trajectory and a relative momentum difference $\beta = \frac{dK}{K}$ with respect to the median momentum will generally not pass through I

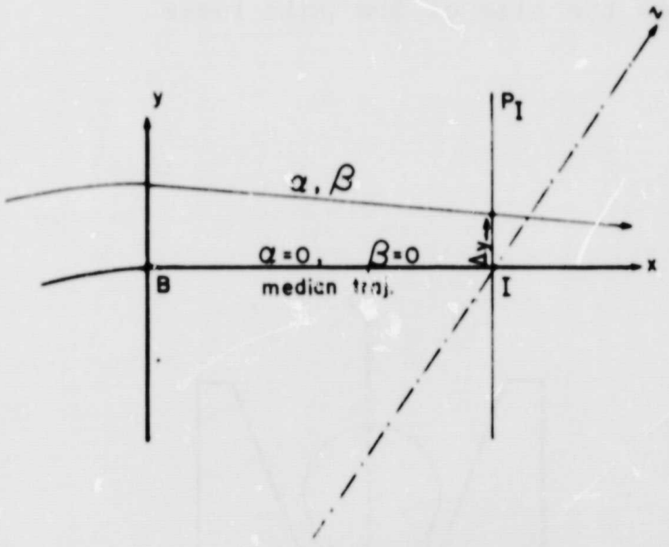

Fig. 44 Coordinate Systems in Image Space

(Fig. 42). If we define an "image plane" P_I perpendicular to the median trajectory in I, this particle will hit P_I with coordinates Δy, Δz (Δz measured from I perpendicular to the plane of Fig. 44). Δy and Δz can be expressed by power series in α, α_z, β as is shown below in (3.8)

$$\Delta y = A_2\beta + A_{11}\alpha^2 + A_{12}\alpha\beta + A_{22}\beta^2 + A_{33}\alpha_z^2 + \ldots\ldots$$

$$\Delta z = B_{23}\beta\alpha_z + \ldots\ldots \qquad (3.8)$$

The coefficients A_{ij} and B_{ij} are called "aberrations". Ideal imaging obviously would occur if all aberrations $A_{ij} = B_{ij} = 0$.

We get the following expressions for the aberrations:

$$A_2 = 2L\ E\ (\phi)\ (K\sin^2\phi + \cos\phi)$$

$$A_{11} = 2L\ \cos\phi\ F(\phi)\ (K\sin\phi + \cot\phi)$$

$$A_{12} = 2L[E(\phi)\ \cos\phi\ (K\sin\phi - \cot\phi) + KH(\phi)\ (K\sin\phi + \cot\phi)] \qquad (3.9)$$

$$A_{22} = LK[(K\sin^2\phi + \cos\phi)\ G(\phi) - 2\ \cos^2\phi\ E^2(\phi)]$$

$$A_{33} = L\ R(\phi)\ (K\sin\phi + \cot\phi)$$

$$B_{23} = 2L\ E(\phi)\ \cot\phi\ (K\ \sin^2\phi + \cos\phi)$$

where the following abbreviations have been used:

$$E(\phi) = e^{-K\cos\phi}[I(1 - K\cos\phi) + JK]$$

$$F(\phi) = Ie^{-K\cos\phi}\ K\sin\phi + \cos\phi$$

$$G(\phi) = e^{-K\cos\phi}[\cos\psi\ (K\cos\phi - 2)\ I + 2(1-K\cos\phi)\ J + K\Sigma]$$

$$H(\phi) = e^{-K\cos\phi}\ [I\ \sin^2\phi + \frac{1}{K^2}\ \sin\phi\ e^{K\cos\phi} + (\cos\phi + K\sin^2\phi)\ (J - I\cos\phi)]$$

$$R(\phi) = \sin\phi\ e^{-K\cos\phi}\ [I(\frac{1}{\sin^2\phi} + K\cos\phi) - \frac{\phi}{2}\ (1 - \frac{2}{\phi^2})\ \cos\phi\ e^{K\cos\phi}]$$

$$I = \int_0^\phi \cos\psi\ e^{K\cos\psi}\ d\psi$$

$$J = \int_0^\phi \cos^2\psi e^{K\cos\psi}\ d\psi$$

$$\Sigma = \int_0^\phi \cos^3\psi e^{K\cos\psi}\ d\psi$$

Figs. 45, 46, 47 show the dependence of the aberrations (3.9) on the deflection angle ϕ_m. The numerical values given in units of r_m (from equation (3.5)).

The total width Δy of the image of a point source at S measured in the image plane is calculated for variances of $\alpha = 0.1$ and $\beta = 0.01$. The results are given in Fig. 45. The corresponding mass resolution R_m which follows from the image width Δy and the 'dispersion' A_2 has been calculated and plotted in Fig. 47.

A comparison of the properties of the type of magnetic field treated above and other magnetic analyzers is given in the next chapter. Here only two aspects are discussed.

a) the aberration A_2 which is also called "momentum dispersion" is approximately constant for deflection angles $\phi_m < 195^o$ and has the value $2r_m$, the same as a homogeneous magnetic sector of the same deflection angle

and deflection radius r_m.

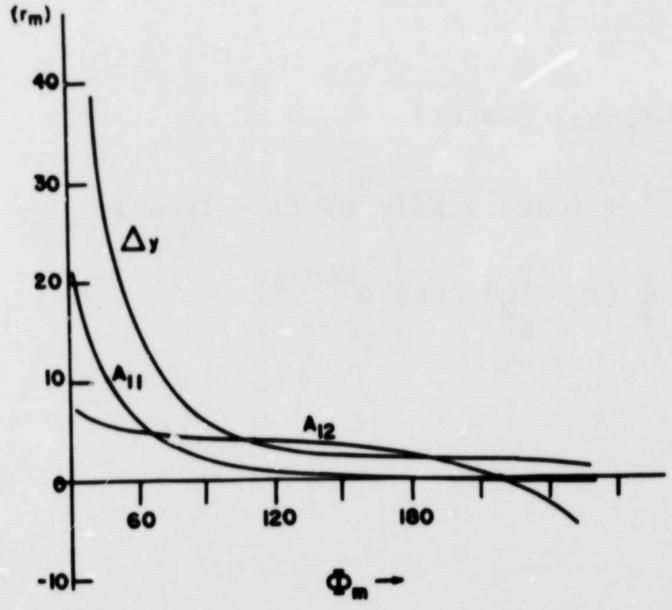

Fig. 45 First and Second Order Aberrations (Δy, A_{11}, A_{12}) of Wedge Magnets

b) for $\phi_m = 180^o$ the aberration due to the opening angle α in the deflection plane vanishes. This case is therefore characterized by high angular acceptance and excellent focusing. O'Connel (Ref. 12) calculated this special case and claims fourth order directional focusing. Fourth order terms however have not been included in the present calculations.

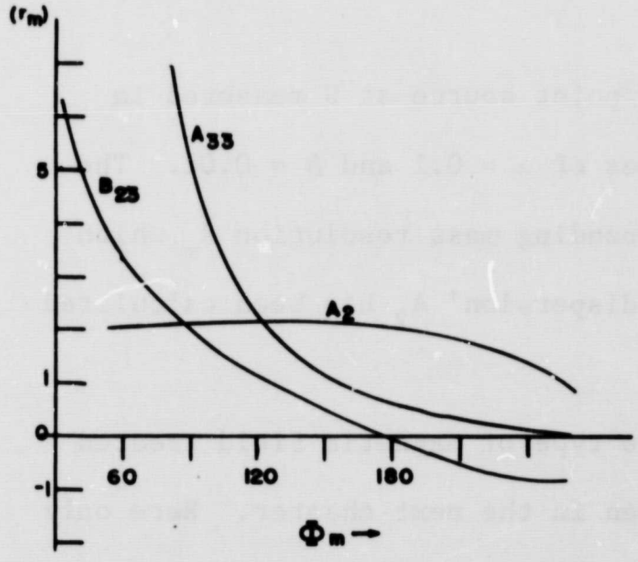

Fig. 46 First and Second Order Aberrations (A_2, A_{33}, B_{23}) of Wedge Magnets

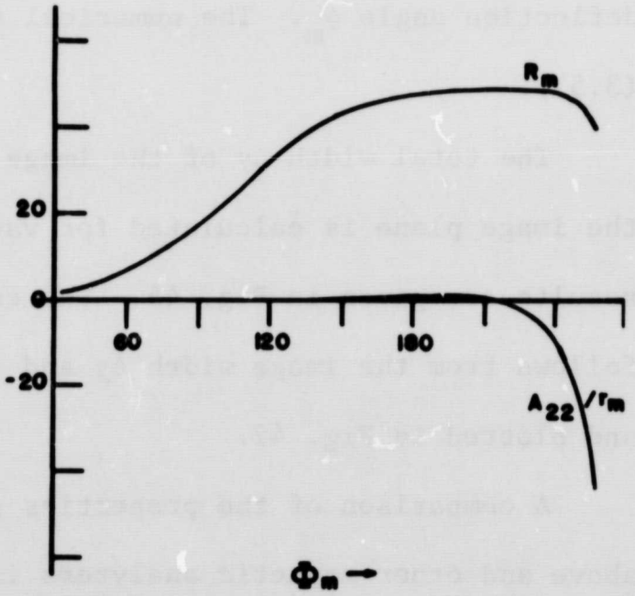

Fig. 47 A_{22}-Aberration and Resolution of Wedge Magnets

3.1.3. Comparison of the wedge magnets with other types of stigmatic focusing magnets.--A mass analyzer which is to be used in an ion implantation

or bombardment system has to meet certain basic requirements:

a) stigmatic point to point focusing

b) high transmission

c) sufficient mass resolution throughout the periodic system.

For mass analysis of ion beams with the intensities and energies usually encountered in bombardment and implantation work, magnetic deflection type analyzers are the most feasible. Two types of stigmatic focusing magnets have been thoroughly investigated in literature and have also found wide practical application. The first is the homogeneous sector field with non-perpendicular beam trajectories at the entrance and exit boundaries. If the parameters of this ion optical system are chosen properly the point to point focusing is caused by that component of the fringing fields at the magnet boundaries which is perpendicular to both the ion beam and the magnetic field between the pole faces. Hintenberger (Ref. 13) gave an extensive treatment of the ion optical properties of homogeneous magnetic fields including all second order aberrations.

Stigmatic focusing has also been achieved by inhomogeneous sector fields with rotational symmetry. If the logarithmic field gradient in the radial direction (from the axis of symmetry) is equal to $n = 1/2$ the optical constants in the deflection plane and the sagittal plane become identical. The stigmatic focusing for all corresponding pairs of object and image planes is the result. For the case of rotationally symmetric fields with arbitrary field gradient, optical parameters and aberrations have been calculated by Tasman, Boerboom and Wachsmuth (Ref. 14).

In section 3.1. we have investigated the focusing properties of magnetic sector fields with cylindrical symmetry and a 1/r dependence of the magnetic

field. Such a field is conveniently produced by plane pole faces which intersect at an arbitrary angle. This angle influences the transmission but does not change other optical properties of the system. Therefore in the construct . of such an instrument mechanical tolerances are not as stringent, and adjustment and alignment should be easy compared to the cases mentioned above.

One important parameter of imaging analyzers is the value of the spherical aberration because in most instruments this is the predominant image defect. We will consider here the "total spherical aberration" defined as the quadratic sum of meridional and sagittal second order spherical aberration coefficiencs.

Fig. 48 gives this spherical aberration as a function of the deflection angle for the homogeneous (A_h), the rotationally symmetric stigmatic focusing ($A_{1/2}$) inhomogeneous and the wedge field (A_w). For simplicity of magnet construction and especially for ease of adjustment it is assumed that in all three cases the magnet boundaries are straight lines. It is evident that the inhomogeneous and the wedge field are practically equivalent and for deflection angles above 150^o have a spherical aberration which is smaller by a factor of 4 to 5 than what can be achieved with the fringe field focusing homogeneous field.

The transmission is a second important parameter which determines the quality of an analyzer. It is proportional to the square of the opening angle an ion beam can have without being intercepted by the pole faces or the walls of the vacuum envelope. Fig. 49 shows the transmission of the homogeneous (T_h) and inhomogeneous ($T_{1/2}$) fields in relation to the wedge field (T_w) (Transmission = 100%) for the case of equal mean pole face distances in all three analyzers.

It is obvious that the transmission of the wedge field exceeds the transmission of the n = 1/2 inhomogeneous field by a factor of 3 to 4, whereas for deflection angles larger than 150° the homogeneous field is apparently superior to the other two cases. A more detailed investigation of stigmatic focusing homogeneous magnets shows however that for deflection angles of 150° and larger the particle beam has to cross the magnet boundaries at angles larger than 40° which introduces problems of fringe field shielding and makes aberrations other than the sperical aberration predominant.

From the preceding it can be concluded that the wedge type magnet is superior to the homogeneous magnet because of its lower aberration coefficients and to the inhomogeneous n = 1/2 field because of the higher maximal achievable transmission.

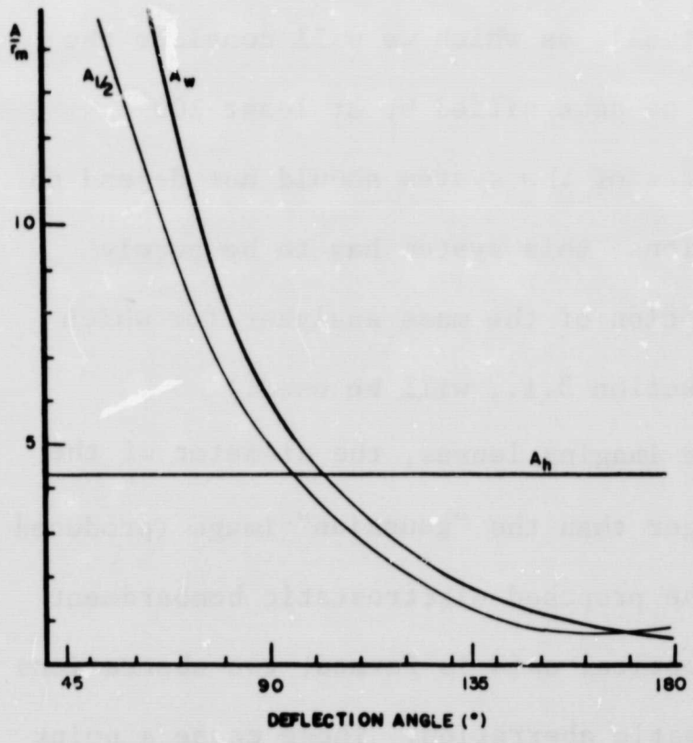

Fig. 48 Comparison of Total Spherical Aberration for Different Types of Stigmatic Focusing Magnets

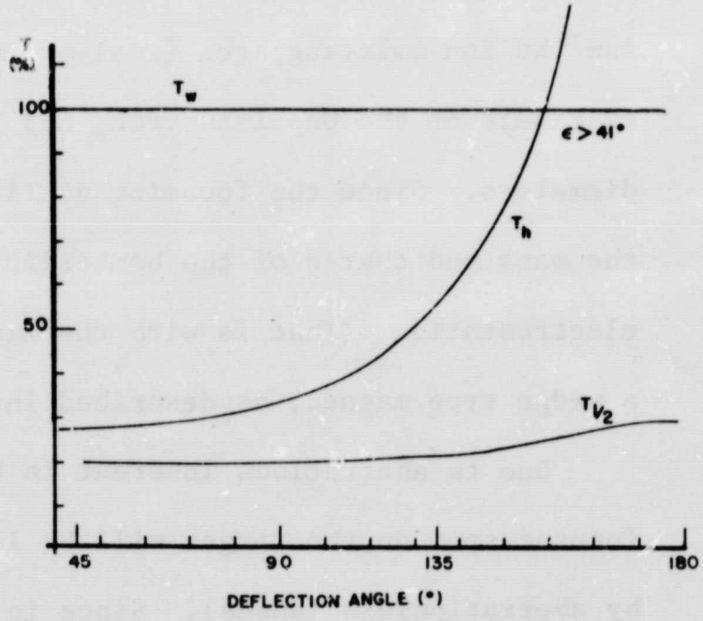

Fig. 49 Comparison of Maximum Transmission for Different Types of Stigmatic Focusing Magnets

3.2. Electrostatic Demagnifying and Deflection System

In order to bombard the surface of a solid with ions of a selected species in a pattern with a spatial resolution in the order of one micron, the ion beam emerging from a suitable source has to be mass analyzed, accelerated if necessary, and focused into a spot with a diameter of 1µm. In addition, a deflection system has to be provided which can move the spot across the target area. The total span of the deflection will generally be large compared to the spot size.

The high temperature Unoplasmatron described in section 2.2. can be modified so that the exit hole has a diameter of 10^{-2} cm. The total ion current will thereby be reduced according to the ratio of the areas. The brightness β however will remain approximately constant. For a spot size of 1µm the ion emitting area (real or virtual), as which we will consider the exit hole of the Unoplasmatron, has to be demagnified by at least 100 diameters. Since the focusing qualitites of the system should not depend on the mass and charge of the bombarding ions, this system has to be purely electrostatic. (That is with the exception of the mass analyzer for which a wedge type magnet, as described in section 3.1., will be used.)

Due to aberrations inherent in the imaging lenses, the diameter of the focused spot on the target will be larger than the "gaussian" image (produced by aberrationless lenses). Since in the proposed electrostatic bombardment system only a very small image on the optical axis is formed, two aberrations predominate, namely spherical and chromatic aberration. These cause a point to be imaged as a circular disc with diameters d_s and d_c respectively.

Using the simplifying assumption that gaussian diameter d_g, spherical aberration disc d_s, and chromatic aberration disc d_c superimpose linearly,

the total diameter d of the focused spot is

$$d = d_g + d_s + d_c \qquad (3.2.1)$$

(It is often assumed that the aberrations add in quadrature (Ref. 15).) The size of the aberration discs is given in a third order approximation by (Ref. 15):

$$d_s = 2C_s\alpha^3 \quad [cm]$$
$$d_c = 2C_c\frac{\delta V}{V}\alpha \quad [cm] \qquad (3.2.2)$$

C_s.....spherical aberration coefficient [cm]

C_c.....chromatic aberration coefficient

α .....beam opening (half angle) in image space

$\delta V/V$...relative energy spread of ions

It is possible to correct the third order spherical aberration totally by use of non-rotationally symmetric multi-element electrostatic lenses and corrector pieces (Ref. 17). For ease of construction and adjustment however, it is more convenient to use rotationally symmetric lenses.

C_s can be written in the form (Ref.17)

$$C_s = K_s \cdot f \quad [cm] \qquad (3.2.3)$$

K_s.....spherical aberration constant, determined by lens geometry only

f .....focal length [cm]

Theoretically, C_s can be made arbitrarily small by size scaling all linear dimensions of the lens but keeping the lens voltages constant. In practice however, the minimum size of the lens is determined by the maximum admissible field strength between the lens electrodes (100-150 KV/cm). This also sets a lower limit for f of ~1cm for most electrostatic lenses (Hanszen

and Lauer, Ref. 16). The only way to further reduce the spherical aberration of rotationally electrostatic space charge free lenses is to optimize K_s by choosing a suitable lens geometry. This has been done by Butler (Ref. 19) for accelerating two potential lenses. He systematically varied the potential distribution within the lens and with the aid of a computer calculated the corresponding aberration. For accelerating two potential lenses no such optimizing procedure has yet been attempted. Primarily due to convention, the symmetrical unipotential lens has been the most frequently used type in electron and ion optical systems (Refs. 18, 20). Values of $12.5 < K_s < 20$ can be achieved with such lenses (Ref. 18). With asymmetrical einzellenses however, lower values can be obtained (Ref. 21). Septier (Refs. 18, 22) describes an unsymmetrical lens with a minimum aberration constant $K_s \approx 2.5$. This lens is shown in Fig. 50. It is nearly identical to that described by Hanszen and Lauer (Ref. 16). In Ref. 18, as in most references, K_s is given for the case of large magnification where the object is near the focal point on the side of higher field strength (left side in Fig. 50). In the present work however, the lenses work at magnifications $<< 1$. In this case the object is far away on the right side of Fig. 50 and the image is formed near the left focal point, just outside the lens field. The corresponding value of C_s for small magnification can be derived from the value C_o for large magnification (referred to the opposite lens side) by the "reverse ray tracking" method (Ref. 16).

In Fig. 51 a point object is situated at I, near the focal point, F, on the left side of an einzellens. Its image is located at O, far beyond F'. In this case the lens operates at high magnification from left to right and low magnification from right to left. ($M << 1$.) The size of the spherical

aberration disc around O is given by

$$d_s(\infty) = 2C_o\alpha'^3 \qquad (3.2.4)$$

For this case K_s is known from the work of Septier (Ref. 18). Therefore, for an assumed minimum focal length of f = 1cm, $C_o \cong 2.5$ cm. Now the rays can be traced in reverse direction (right to left in Fig. 51). In this case the aberration disc (diameter $d_s^r(o)$) can be considered the image of $d_s(\infty)$

$$d_s^r(o) = Md_s(\infty) = 2MC_o\alpha'^3$$

$$\text{or} \qquad d_s^r(o) = 2C_oM^4\alpha^3 \qquad (3.2.5)$$

(3.2.5) gives the size of the aberration disc for the Septier-lens operated in reverse direction at low magnification.

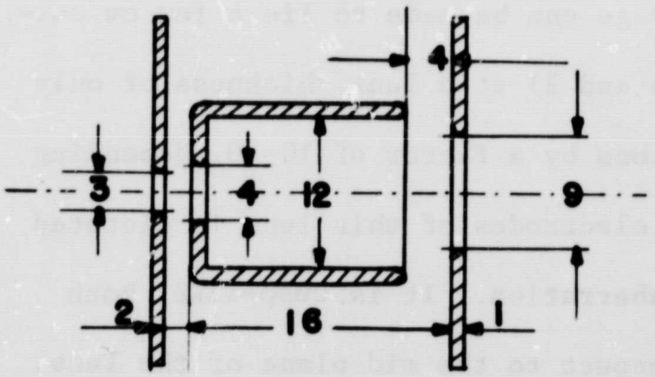

DISTANCES IN mm

Fig. 50 Electrostatic Lens with Low Sperical Aberration

The chromatic aberration coefficient of the same lens can be calculated using data from a graph of the position of the cardinal elements for a very similar lens (pg. 273 of Ref. 16). From there it follows that C_c is very nearly constant for small magnifications.

$$C_c = 0.33 \text{ cm} \qquad (3.2.6)$$

For symmetrical einzellenses optimum values for C_c between 20 cm and 2.5 cm have been reported (Refs. 23, 24).

The Septier lens used in demagnification is therefore well suited to concentrate a high current of ions and electrons into a very small spot.

The position of this spot is very close to the image side focal point which is only about 1mm beyond the last lens electrode. There would be no room for a deflection system to move the focused spot across the target. In addition, the maximum permissible field strength in the lens would limit the energy of the particles which can be focused to about 10-15 KeV.

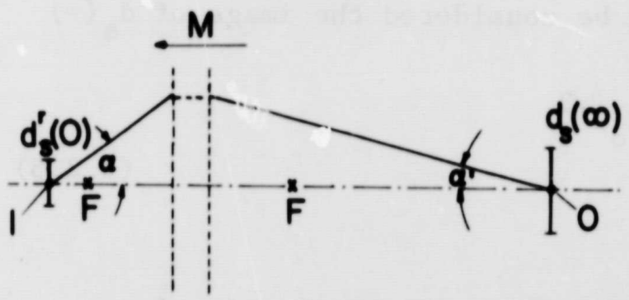

Fig. 51 Reverse Ray Tracing

For these reasons a minimum aberration lens, described by Butler (Ref. 19) and successfully employed by Crewe (Ref. 25) in a scanning electron microscope, was chosen as the last stage of the demagnifying system. This lens has two advantages other than its minimized spherical aberration; 1) the image can be made to lie a few cm outside the lens, maintaining low aberration and 2) at a lens thickness of only 2 cm it can increase the energy of 2KeV ions by a factor of 10-20, depending on the image position. The shape of the electrodes of this lens is dictated by the requirement of minimum spherical aberration. It is cusp-like, both electrodes being mirror symmetric with respect to the mid-plane of the lens. The field at the points of enterance and exit of the beam is zero, so that exit and entrance openings cause minimum disturbances of the ideal field shape. The electrodes are conveniently machined on a tape controlled lathe according to the shape described in Ref. 26.

For reasons which will later become obvious, it is proposed to perform demagnification in a three-lens system consisting of two consecutive Septier lenses in demagnification and a Crewe lens as final focusing and postacceleration stage (Fig. 52). As pointed out above (3.2.1), linear superposition

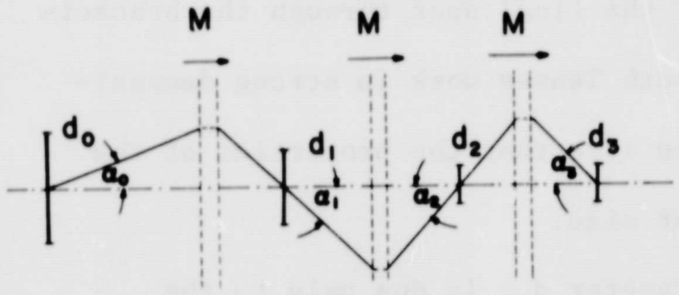

Fig. 52 Three stage Demagnifying System

of gaussian image, spherical, and chromatic aberration discs in both the intermediate and the final image will be assumed. Therefore the sizes of the consecutive images d_1, d_2, d_3 (Fig. 52) are given by (3.2.7) below:

$$d_1 = d_{1g} + d_{1s} + d_{1c}$$

$$= M_1 d_o + 2C_o M_1^4 \alpha_1^3 + 2C_c' \alpha_1$$

$$d_2 = d_{2g} + d_{2s} + d_{2c} = M_2 d_1 + 2C_o M_2^4 \alpha_2^3 + 2C_c' \alpha_2$$

$$d_3 = d_{3g} + d_{3s} + d_{3c} = M_3 d_2 + \frac{C_s}{2} M_3^4 (V_o/V_1)^{3/2} \alpha_3^3 + 2C_c'' \alpha_3 (V_o/V_1 - 1)$$

$$= M_1 M_2 M_3 d_o + [2C_o M_2^4 M_3^4 (1 + M_1^4) + \frac{C_s}{2} M_3^4 (V_o/V_1)^{3/2}] \alpha_3^3 +$$

$$+2[C''_c (V_o/V_1 - 1) + C_c' M_3^2 (1 + M_2^2)] \alpha_3 \qquad (3.2.7)$$

$C_c' = C_c \frac{\delta V}{V}$ .....chromatic aberrations of Septier lens times relative energy spread of ions

C_c''..... chromatic aberrations of Crewe lens times relative energy spread of ions

C_s ..... spherical aberration coefficient of Crewe lens

V_1 ..... ion energy before postacceleration

V_o ..... ion energy after postacceleration

M_1, M_2, M_3 .... magnifications of the three stages

Aberration expressions have been taken from Ref. 25 for the third lens.

The first lens enters into the dize d_3 of the final spot through the brackets $(1 + M_1^4)$ and $(1 + M_2^2)$ in (3.2.7). If both lenses work in strong demagnification, both brackets approach the value 1 so that the properties of the first lens do not influence the final spot size.

The current I_3 in the final spot, diameter d_3, is due only to the current which would flow through the gaussian image in an aberration lens (Ref. 16). It can be written as

$$I_3 = \frac{\pi^2}{4} \beta \frac{V_o}{V_1} \alpha_3^2 d_{3g}^2 \qquad (3.2.8)$$

β.....Brightness of the ion source

The factor $\frac{V_o}{V_1}$ comes from the fact that the brightness of an electron optical image is proportional to the energy of the particles.

Using (3.2.7) and (3.2.8) :

$$I_3 = \frac{\pi^2}{4} \beta \frac{V_o}{V_1} \alpha_3^2 [d_3 - (2C_o M_2^4 M_3^4 + \frac{C_s}{2} M_3^4 (V_o/V_1)^{3/2}) \alpha_3^3 -$$

$$- 2(C_c''(V_o/V_1 - 1) + C'_c M_3^2 \alpha_3]^2 \qquad (3.2.9)$$

d_3 is the desired spot size, therefore it can be considered a constant. Other constants in (3.2.9) are β, C_o, C'_c, V_o/V_1. To optimize the beam current I_3 in a spot of diameter d_3, I_3 has to be differentiated with respect to the independent variables α_3, M_2, M_3, C_s, C_c'', and the derivatives set to zero. Since no analytical expressions for the elements of the Crewe-lens are available a convenient operating point for this lens is chosen fixing M_3, C_s, C_c'' amd leaving as independent variables only α_3 and M_2. The operating point of the Crewe lens is chosen mainly with respect to the working distance (S = 2cm) making it possible to put a deflection stage between the last

electrode and the target. For a working distance of 2 cm it follows from Ref. 25 that

$$\begin{aligned} S &= 2 \text{ cm} \\ V_o/V_1 &= 18 \\ C_c'' &= 0.45 \times \delta V/V \text{ cm} \\ C_s &= 9 \text{ cm} \\ &\text{object distance} = 1 \text{ cm} \end{aligned} \tag{3.2.10}$$

Plugging in the numerical values of all the constants and assuming a relative energy spread of $\delta V/V = 10^{-3}$ results in:

$$I_3 = \frac{9\pi^2}{2} \beta\alpha_3^2 \left[d_3 - (7.25M_2^4 + 76.5)\,\alpha_3^3 - 1.61 \times 10^{-2}\,\alpha_3\right]^2 \tag{3.2.11}$$

Differentiation of (3.2.11) with respect to α_3 and M_2 shows that there is no extremum of I_3 for physically possible values of α_3 and M_2 but that I_3 increases monotonically as M_2 decreases. A very small M_2 however would mean an extremely long object distance for an instrument consisting of only one demagnifying stage in front of the Crewe lens. An alternative procedure is therefore to build as short an instrument as possible, keeping the overall magnification M_1, M_2 constant. As Mulvey points out in Ref. 16, this can be achieved by arranging two lenses of equal demagnification $M_1 = M_2 = \sqrt{M_1M_2}$ in series. The total length l from object to second intermediate image follows from elementary geometrical optics:

$$\ell = 2\left(\frac{f}{\sqrt{M_1M_2}} + 2f + \Delta\right) \tag{3.2.12}$$

M_1M_2.....overall magnification of 1st and 2nd stage

f.....focal lengths of 1^{st} and 2^{nd} stage (equal)

Δ.....distance of principal planes of 1^{st} and 2^{nd} stage (equal)

Since $M_2 = M_1$ has a small value, (3.2.11) now is a function of α_3 alone. However, no maximum for I_3 is found for physically acceptable values of α. An alternative way is chosen to approximately optimize I_3. It is possible to write

$$d_g = h d_3 \tag{3.2.13}$$

where h is a constant < 1. From (3.2.11) the diameter of the chromatic aberration disc is

$$d_c = 1.6 \times 10^{-2} \alpha_3 \tag{3.2.14}$$

It is further assumed that the chromatic disc is larger than the spherical disc so that

$$d_c \cong (1 - h)\, d_3 \tag{3.2.15}$$

This expression as well as (3.2.13) is plugged into (3.2.11) so that, neglecting all constants

$$I_3 = \alpha_3^{\,2}\, d_g^{\,2} = (1 - h)^2\, h^2\, d_3^{\,4} \tag{3.2.16}$$

Optimization with respect to h gives

$$h = 1/2$$

which means that the gaussian image diameter should be half the total spot size for optimum conditions. From (3.2.13) follows the optimized α_3

$$\alpha_3 = 3.57 \times 10^{-3}$$

Therefore the diameters of the aberration discs are

$$d_c = 0.5 \times 10^{-4}$$

$$d_s = 3.4 \times 10^{-4} << d_c$$

The magnifications follow from (3.2.13) with h = 1/2

$$M_2{}^2 M_3 = \frac{d_{3g}}{d_o} = 0.5 \times 10^{-2} \qquad (3.2.18)$$

or $$M_2 = M_1 = 0.67 \times 10^{-1}$$

and with α_3 and d_{3g}

$$I_3 = \beta \times 1.41 \times 10^{-12} \text{ A} \qquad (3.2.19)$$

The current density on the target is

$$J_3 = \beta \times 1.8 \times 10^{-4} \text{ A/cm}^2 \qquad (3.2.20)$$

Using the brightness values for the metal Unoplasmatron $\beta = 0.1$, the maximum current density in the 1µm diameter final spot is

$$J_3 = 18 \text{ µA/cm}^2$$

A 4 plate electrostatic condenser immediately following the second electrode of the postacceleration lens can be used to deflect the spot across the target surface. The parallel condenser plates have a length of 1 cm and a distance of 0.3 cm which leaves a space of 1 cm between the condenser and the target. The voltage V_p between two opposite condenser plates which is required to deflect the spot by an amount Δ on the target is given by Klemperer (Ref. 27).

$$V_p = \frac{V_o \Delta d}{\ell(S - \frac{\ell}{2})} = 0.2 V_o \Delta \qquad (3.2.21)$$

V_o.....particle energy

d..... plate distance

ℓ .....plate length

S .....working distance

For a particle energy of 40 KeV and a maximum deflection of 1000 μm for instance, the deflection voltage required is 800 volts.

Fig. 53 shows a schematic of the ion bombardment system including mass analyzer and ion source. The exit slit S" with a width of 10^{-2} cm of the mass analyzer serves as object point for the demagnification system. Since the ion source exit hole is also 10^{-2} cm in diameter the magnet has to form a near perfect stigmatic image with unit magnification at S". The "wedge" magnets described in section 3.1. are well suited to this purpose since they exhibit unit lateral and angular magnification as well as stigmatic focusing. Therefore

$$\alpha_o = \alpha_m$$

α_m .... beam opening at the ion source

The angles α_o admitted by the demagnification system follow from (3.2.17) and (3.2.18).

$$\alpha_o = \frac{V_o}{V_1} M_1^2 M_3 \alpha_3 = 3.54 \times 10^{-4} = \alpha_m \qquad (3.2.22)$$

In section 3.1. the spherical aberration of wedge magnets is given

$$\Delta y = A_{11} \alpha_m^2 .$$

If r_m is chosen to be 20 cm, Fig. 45 shows that for wedge magnets of nearly all deflection angles, the image defect due to spherical aberration is much smaller than the gaussian image. the magnet geometry can therefore be chosen according to size and accessability considerations.

For $\phi_m = 90^o$

$r_m = 20$ cm (3.2.23)

The magnet aberration is

$$\Delta y \cong 2 \times r_m \times \alpha_m^2 = 5.04 \times 10^{-6} \text{ cm}$$

which is negligible compared to S'' = 10^{-2} cm.

The other magnet parameters follow from form. (3.2.23) and section 3.1. as

K = 0.55

L = 17.2 cm

SI = 48 cm (source image distance)

ρ = 11.0 cm (radius of curvature of trajectory at r_m)

H = 5.86 k Gauss (magnetic field strength at r_m)

Ions are produced in the ion source (see Fig. 53) and preaccelerated to 2.2 KeV by the extractor electrode. Mass analysis of the ion beam is then performed in the analyzer magnet. The actual mass selection takes place at the mass selector slit of width 0.1 mm. With this slit width a mass resolution M/ΔM of $\sim$ 2000 and an energy resolution of $\Delta V/V \sim 0.25 \times 10^{-3}$ is obtained. The mass selector slit which can also be shaped as a circular diaphragm serves as the object for the following demagnification system. The first two lenses form a demagnified image of the mass selector diaphragm without changing the energy of the ions. Mass selector slit, first and second demagnifying lens have equal distances of 14.9 cm. The postacceleration lens accelerates the ions to a final energy of 40 KeV and focuses them onto the target.

Lower bombardment energies are obtained by changing all acceleration and lens voltages in proportion. The aperture stop which determines the final aperture of the beam and thereby the size of target spot can be located at the entrance of the postacceleration lens or near the entrance of the second

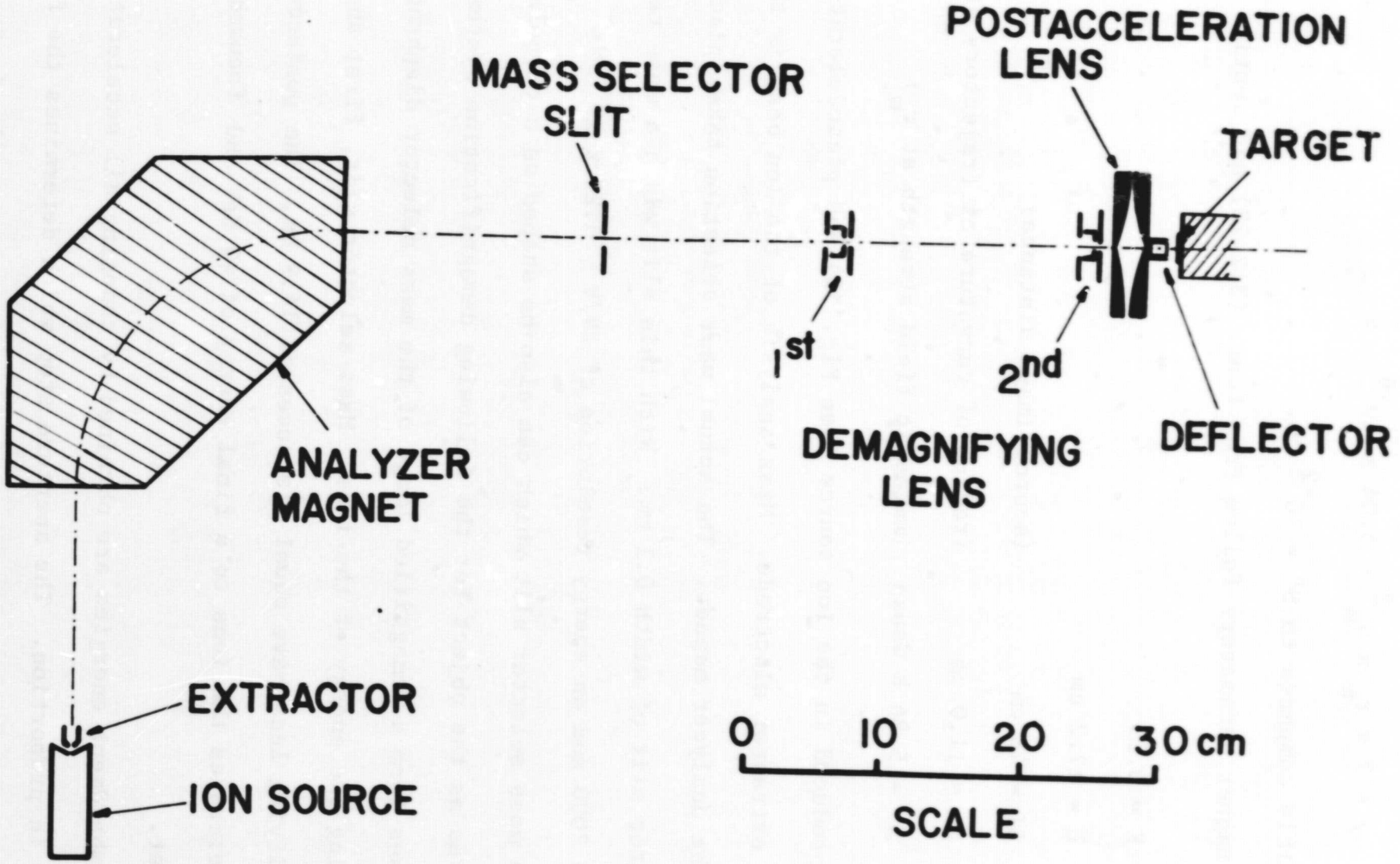

Fig. 53 40 KeV Heavy Ion Bombardment System with Mass Selection Capable of Selective Area Ion Bombardment with a Resolution of 1 μm.

demagnifying lens. The latter choice has the advantage of a more convenient size of the aperture diameter d_A

$$d_A = 2\ell M_2 M_3 \frac{V_o}{V_1} \alpha_3 \cong 0.16 \text{ cm}$$

4. EXPERIMENTS TO DEMONSTRATE THE FEASIBILITY OF THE ION BOMBARDMENT METHOD

Two types of experiments were carried out to show the feasibility of the ion bombardment method.

Fig. 54 shows the effect of a 20 minute bombardment of 2KeV Argon ions (1 μA/cm) on a 4:1 dilution KTFR photoresist. The thickness was less than 1000 Å. The black area has been exposed to the ion beam and the white vertical strip is the shadow of a 2 mm wide current measurement electrode mounted 3 mm in front of the target. A penumbra effect is visible at the edges of the shadowed area.

Fig. 55 shows a comparison of the ion beam bombardment effects and standard ultra-violet light activation of the photoresist on another region of the same wafer so that the photoresist properties were uniform. The resolutions in the two cases cannot be compared from these photographs because of the different mask-substrate distances.

In another series of bombardments 3KeV Ca^+ ions were implanted in epitaxial SiO_2 films on Si to see the effect of interstitial Ca^+ on the mobility of Na impuriites. The results of this experiment as well as the photoresist experiment are still being evaluated at the ERC Cambridge.

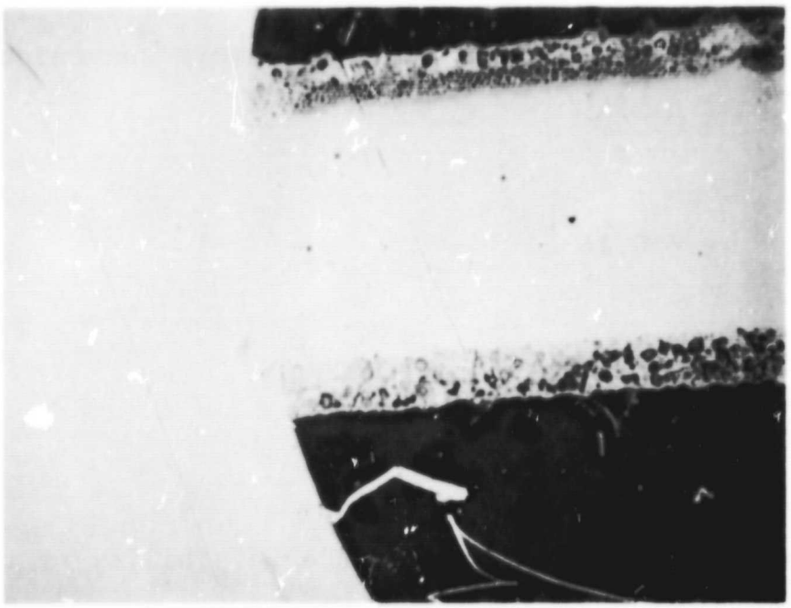

Fig. 54 Photoresist Bombarded with Ar-ions

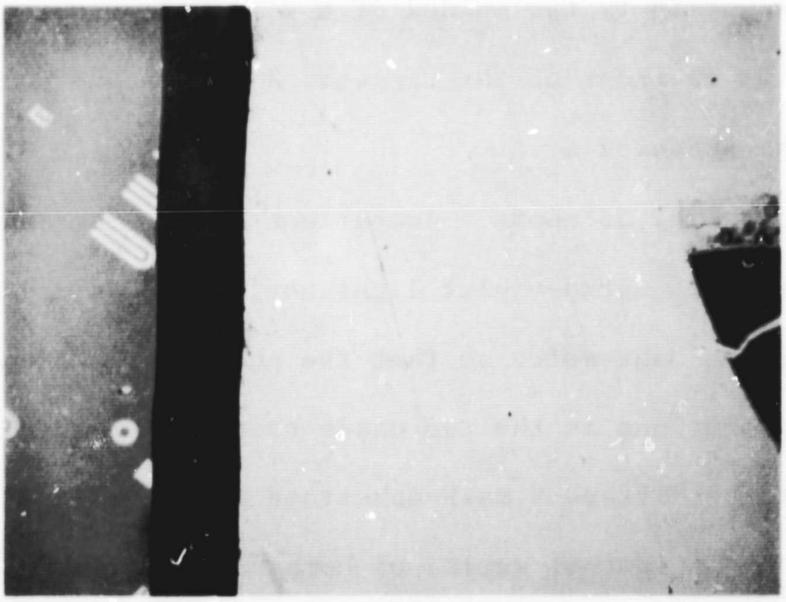

Fig. 55 4:1 Diluted KTFR Photoresist exposed to UV-light (left side) and 2KeV Ar^+ ions (right side)

5. PUBLICATIONS

A talk was given by one of the authors (F.G.R.) at the 1969 Particle Accelerator Conference in Washington, D.C. under the title "A Mass Analyzer System for the High Voltage Terminal of a van de Graff Heavy Ion Accelerator". An article with the same title appeared in the IEEE Transactions on Nuclear Science, Vol. NS-16, No. 3, June 1969 pp.35-37.

REFERENCES

1 von Ardenne, M., "Tabellen zur Elektronenphysik, Ionenphysik und Übermikroskopie", Deutscher Verlag der Wissenschaften, Berlin, 1956.

2 Kistemaker, J., Rol, J.P., and Politek, J., Nucl. Instr. and Meth., 38 (1965) p.1.

3 Dushman, S., Scientific Foundations of Vacuum Technique. J. Wiley and Sons (New York), 1949.

4 Kohl, W.H.: Handbook of Materials and Techniques for Vacuum Devices. Reinhold Publishing Corp. (New York), 1967.

5 Field, F.H., and Franklin, J.L.: Electron Impact Phenomena. Academic Press Inc. (New York), 1957.

6 Kieffer, L.J., and Dunn, G.H., Rev. Mod. Phys. 38, (1966) pp 1-35.

7 Llewellyn-Jones, F.: The Glow Discharge. Methuens Monographs on Physical Subjects (London), 1966.

8 Honig, R.E.: "Vapor Pressure Data for the More Common Elements", RCA Rev., 18, June 1957, pp. 195-204.

9 Crawford, C.K.: "Electron Impact Ionization Cross Sections", Air Force Technical Report AFML-TR-67-367, December 1967.

10 Richardson, H.O.W., Proc. Phys. Soc. (London) 59, (1947), p.59.

11 Koefoed-Hansen, O., Lindhard, J., and Nielsen, O., Kgl. Dan. Vid. Selsk. Mat-Fys. Medd. 25, No. 16 (1950).

12 O'Connel, J.S., Rev. Sci. Instr. 32, No. 12 (1961), p.1314.

13 Hintenberger, H., and König, L.A., Z. Naturforschg. 12a, (1957), p. 773.

14 Tasman, H.A., Boerboom, A.J.H., and Wachsmuth, H., Z Naturforschg. 14 a, (1959), p. 822.

15 von Ardenne, M., Z Physik 108, (1938) p. 338.

16 Septier, A., ed.: Focusing of Charged Particles. vol. I, Academic Press (New York), 1967.

17 Seeliger, R.,Optik 5, Heft 8/9, 1949, p.490.

18 Grivet, P.: Electron Optics. Pergamon Press (New York), 1965.

19 Butler, J.W., in "Electron Microscopy 1966", vol. I (Proc. of the 6th International Congress for Electron Microscopy, Kyoto, Japan, 1966), Ryozi Uyeda, ed., Maruzen Co. Ltd., Tokyo, 1966.

20 Liebl, H., J. Appl. Phys., 38, 5277, December 1967.

21 Hanszen, K.J., Z. Naturforsch. 13a, 1958, p. 40a.

22 Septier, A. CERN 60-39.

23 Boersch, H., Z. Physik 139, 1954, p.115.

24 Bruck, H., and Grivet, P., Rev. Opt. 29, 1950, p.164.

25 Crewe, A.V, Wall, J., and Welter, L.M., J. Appl Phys., 39, No. 13, 1968, pp. 5861-5868.

26 Crewe, A.V., Eggenberger, D.N., Wall, J., and Welter, L.M., Rev. Sci. Instr., 39, No. 4, 1968.

27 Klemperer, O.: Electron Optics. Cambridge University Press, 1953.

APPENDIX A

Construction Drawings for the High Temperature

Unoplasmatron Ion Source

Dwgs. No. 1-39

METAL ION SOURCE
DWG # 01
ANODE PLATE

DETAIL A

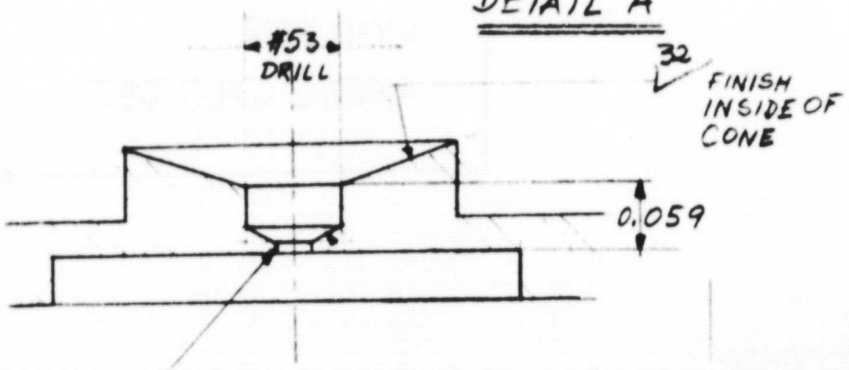

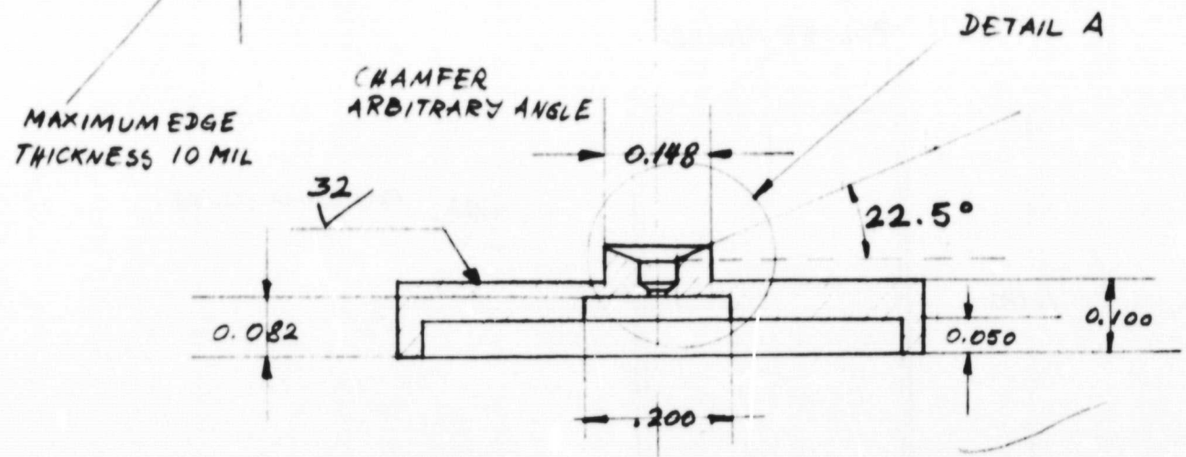

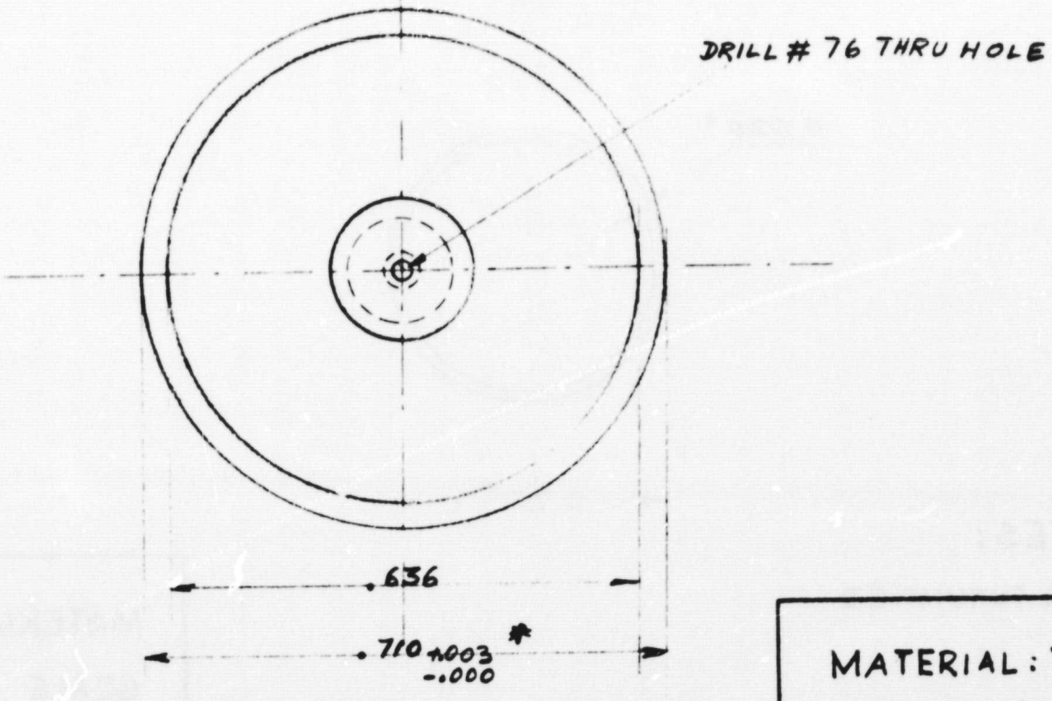

* MAKE TIGHT FIT WITH DWG # 02

MATERIAL : Tantalum
SCALE : 4:1

METAL ION SOURCE

DWG #02

ANODE CYLINDER

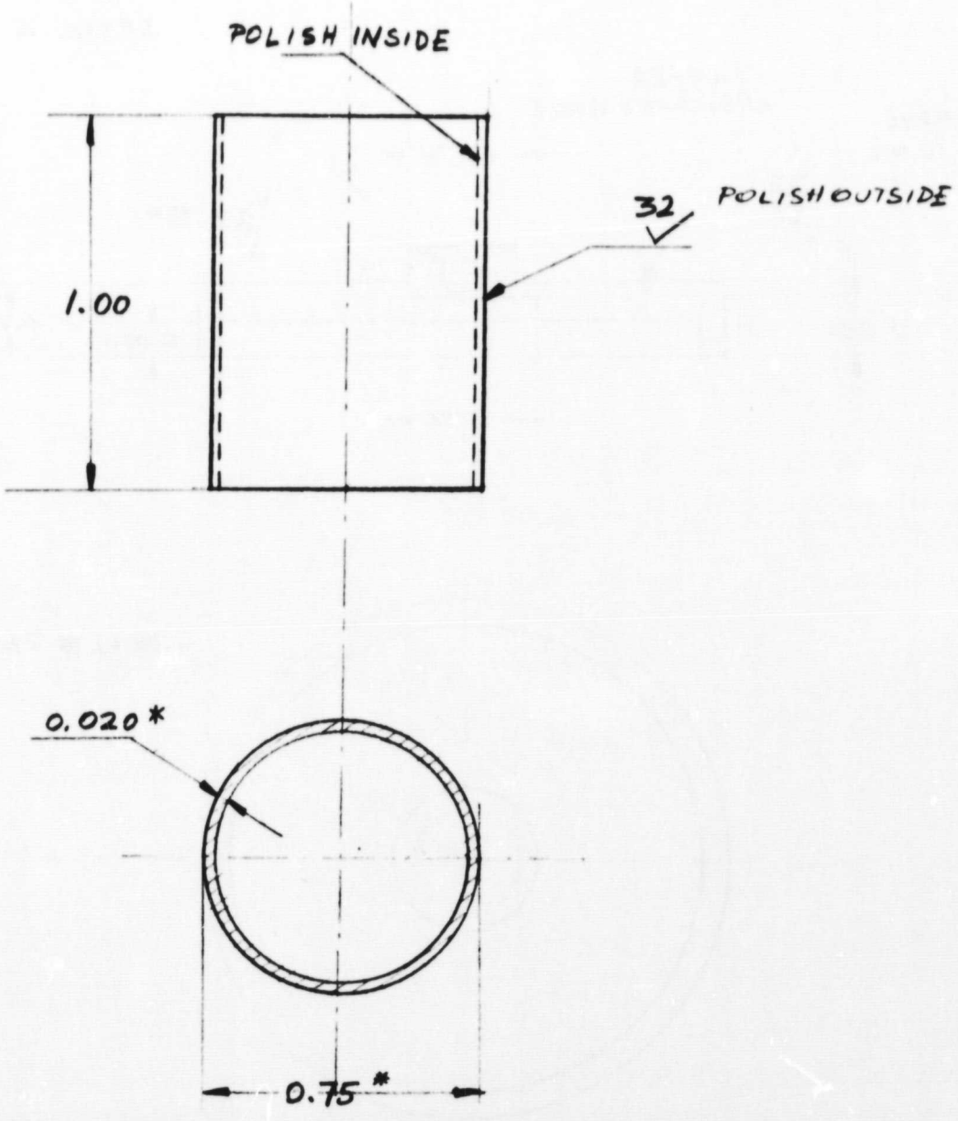

NOTES:

* AS FURNISHED

MATERIAL: Tantalum

SCALE 2:1

METAL ION SOURCE
DWG # 03
ANODE FRONT HEAT SH.

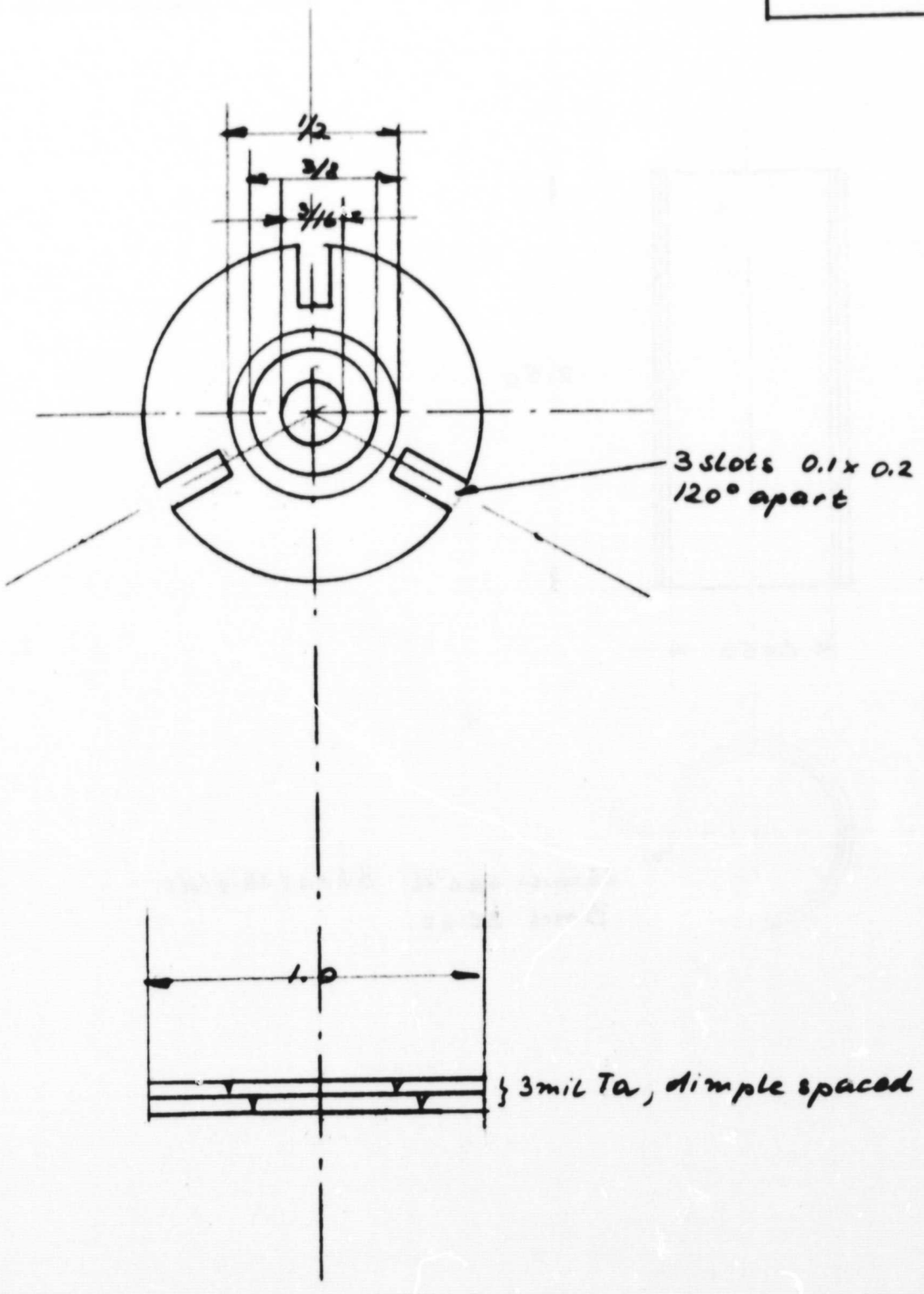

METAL ION SOURCE
DWG# 04
OUTER HEAT SHIELD

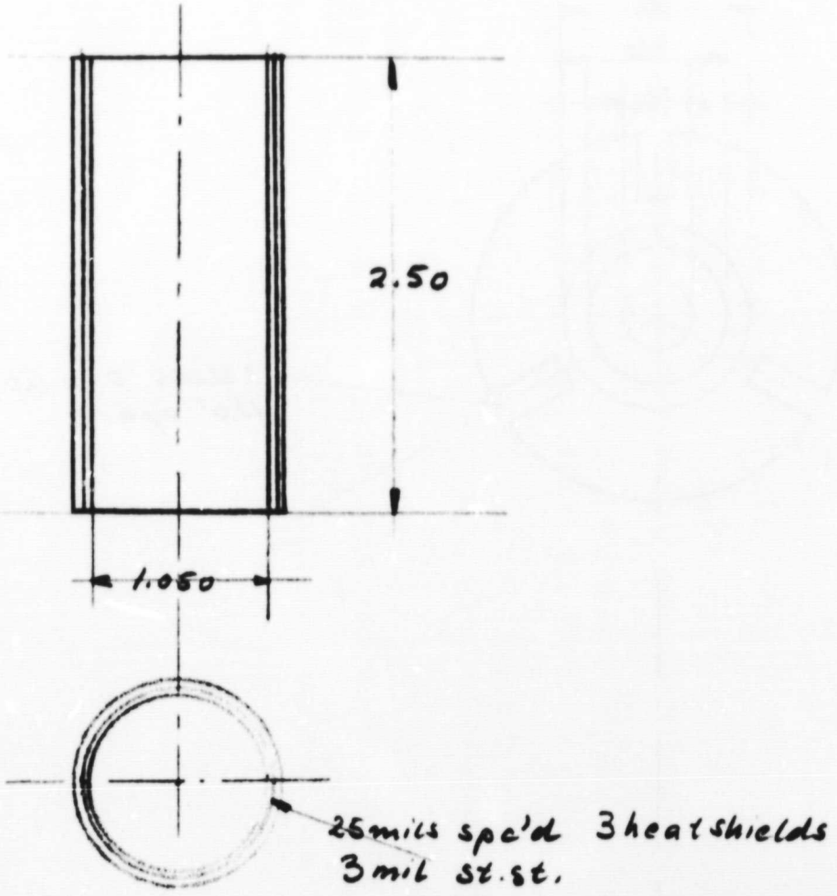

METAL ION SOURCE
DWG # 05
ARC CHAMBER HEAT SHIELDS

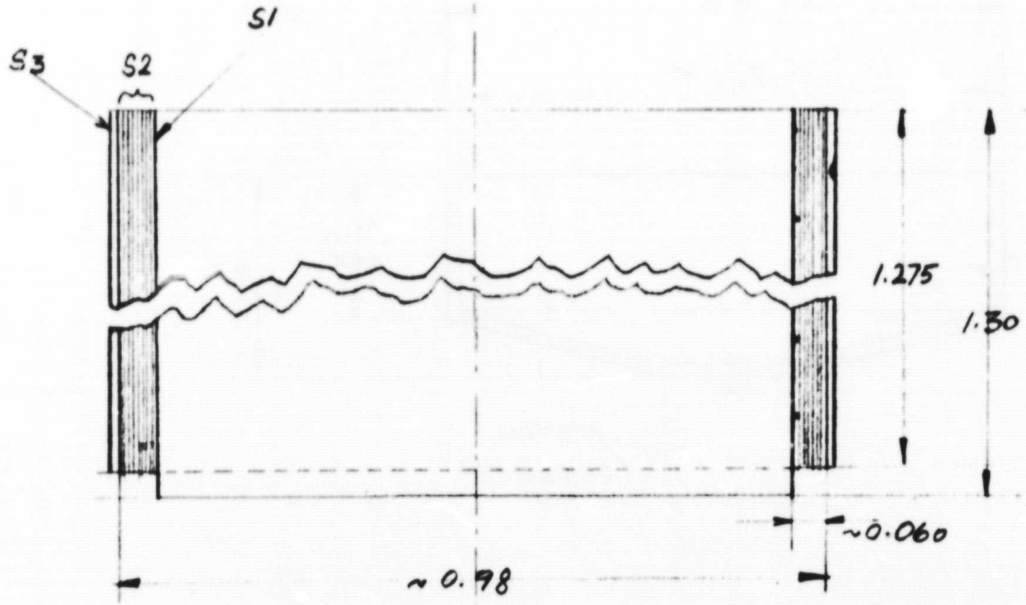

SHIELD	I.D	MAT.
S1	0.860	3mil Ta
S2		1mil & ½ mil Ta. spotwelded to S1 ~ 7 spiral wdgs ~ 18.7" long
S3		3mil ST. ST.

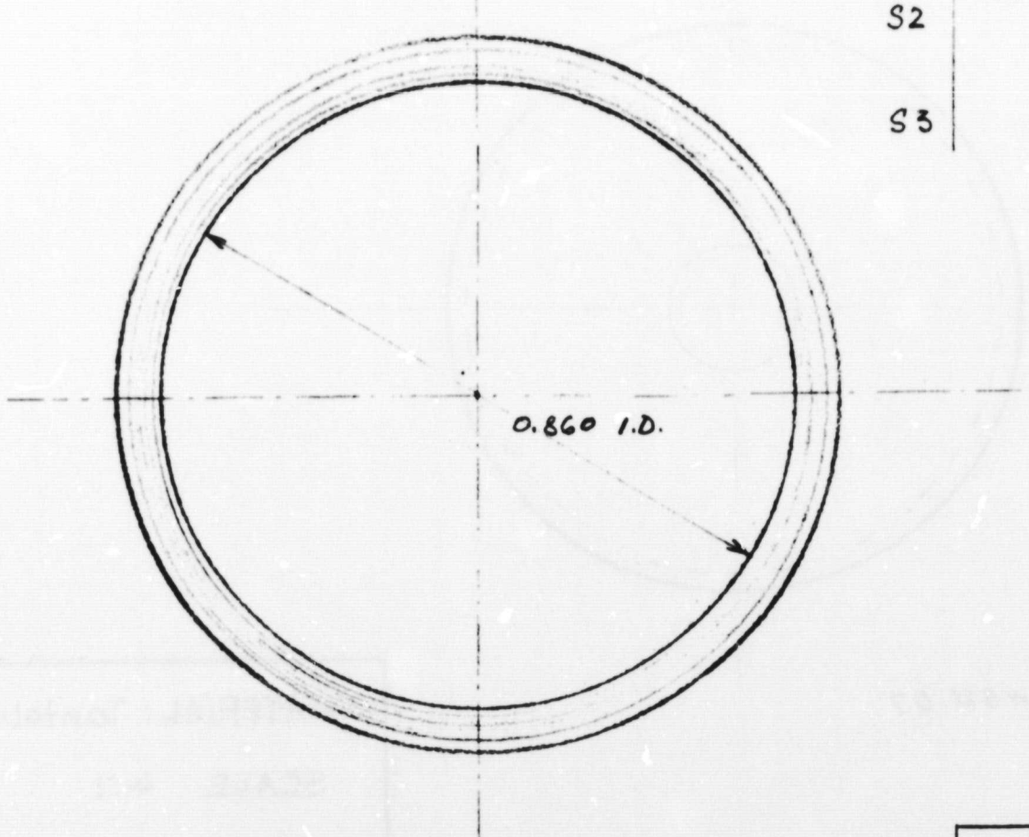

SCALE 4:1

METAL ION SOURCE

DWG # 06

ANODE CONE

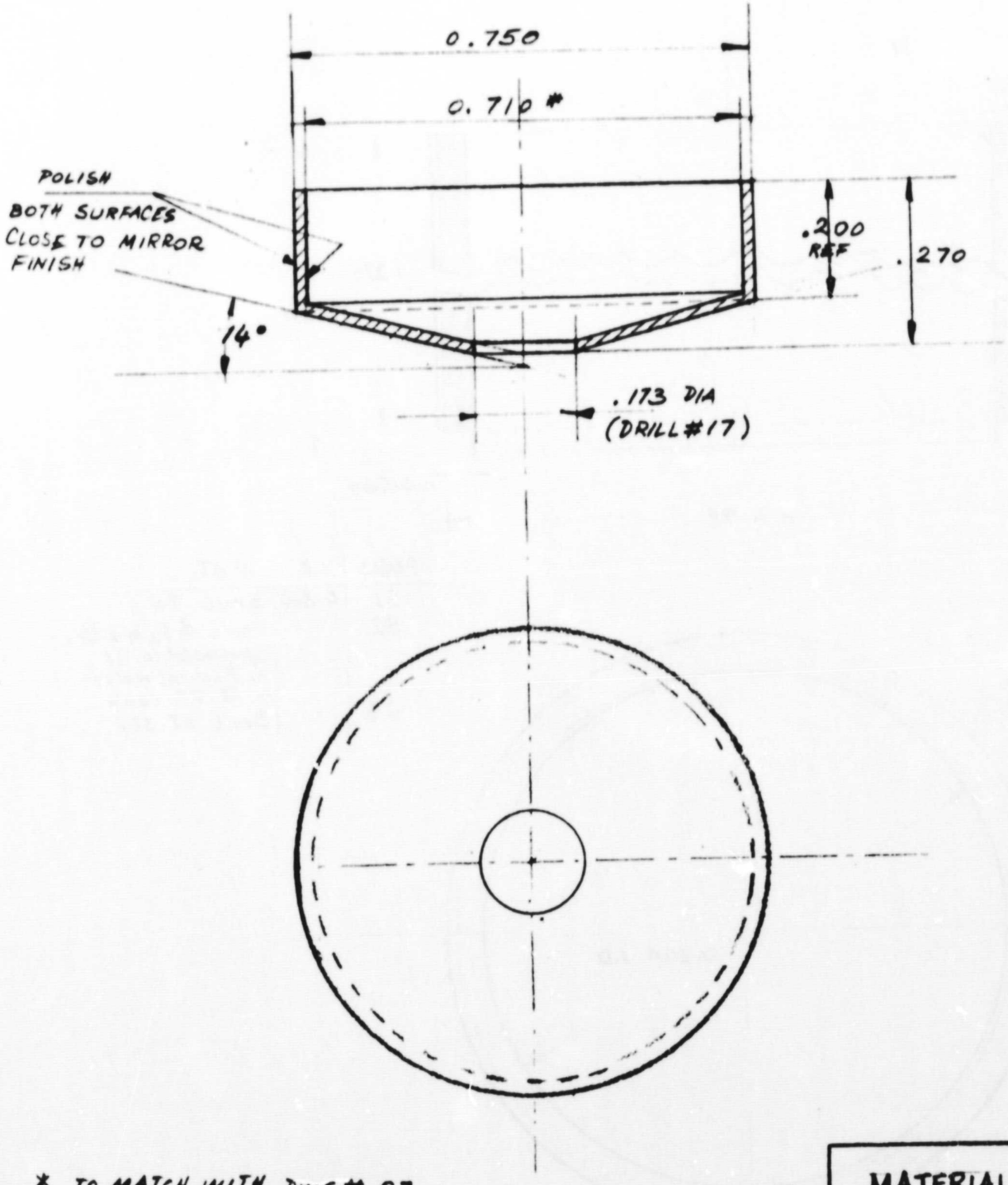

* TO MATCH WITH DWG # 07

MATERIAL: Tantalum

SCALE 4:1

METAL ION SOURCE
DWG # 07
ANODE CONE EXTENSION

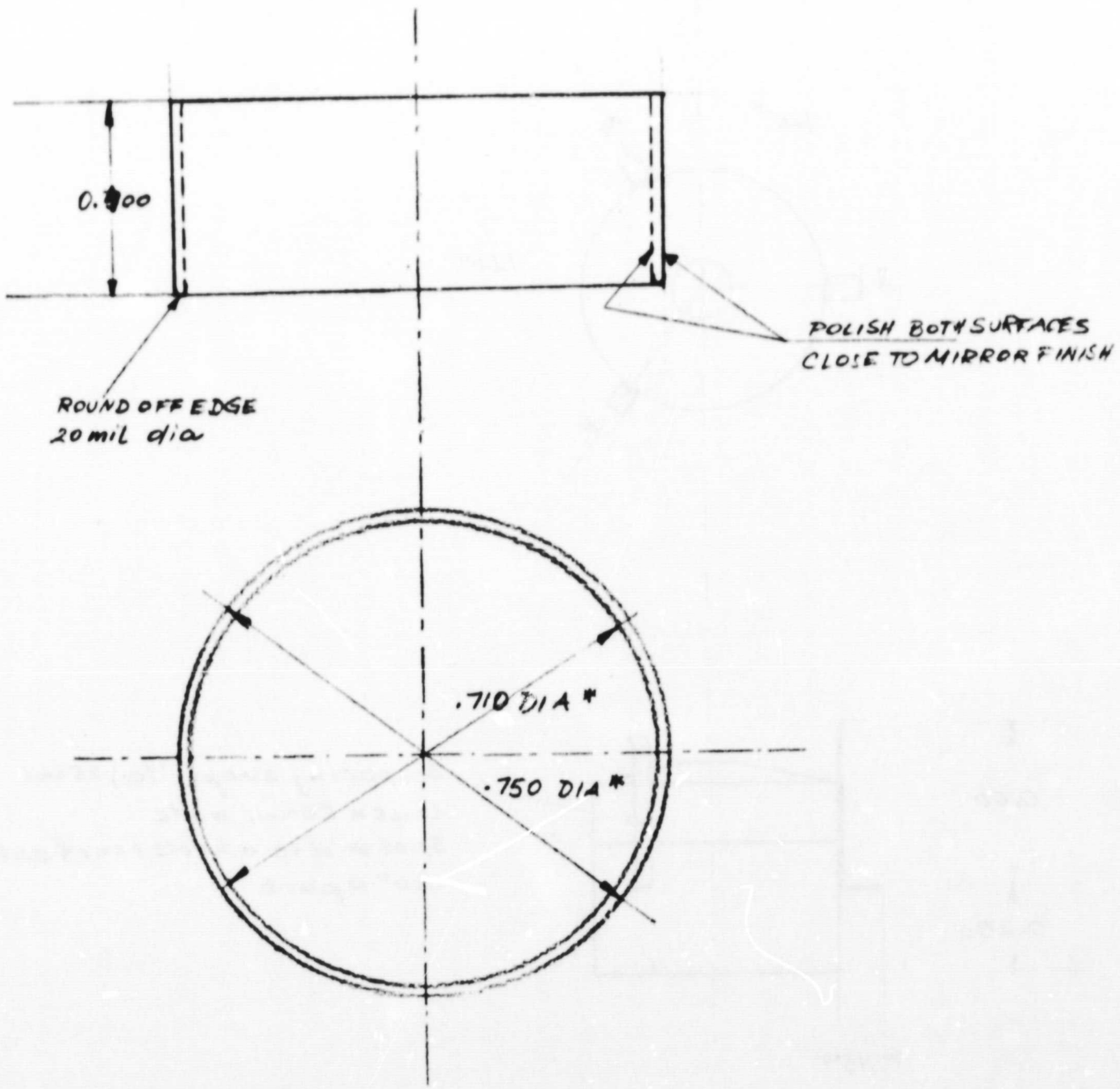

* TO MATCH INSIDE WITH DWG # 06
DIMENSIONS AS Ta-tubing SUPPLIED

MATERIAL: Tantalum
SCALE 4:1

METAL ION SOURCE
DWG # 08
EXTRACTION ANODE ASS'Y

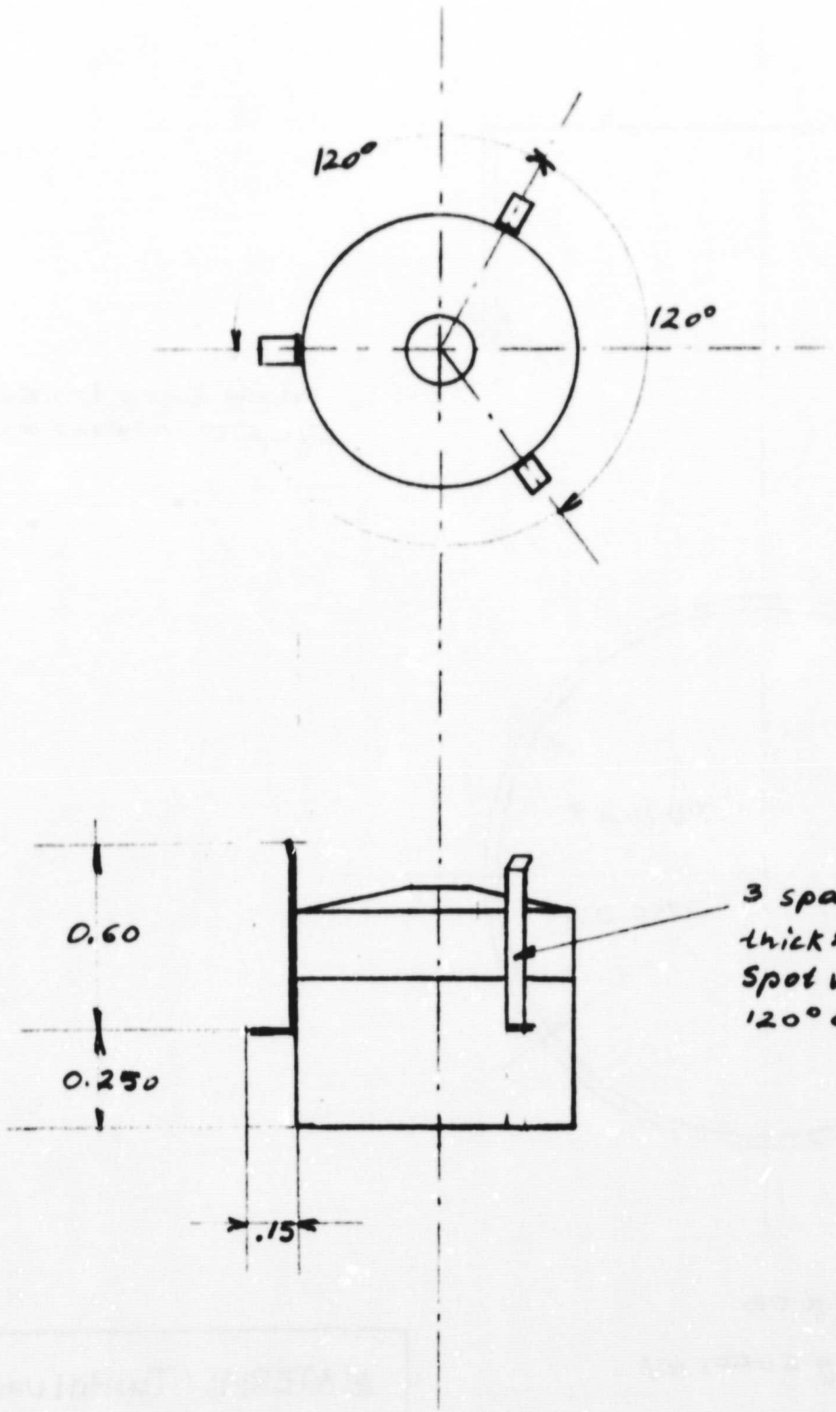

METAL ION SOURCE
DWG # 9

ANODE CONE DIE SET II

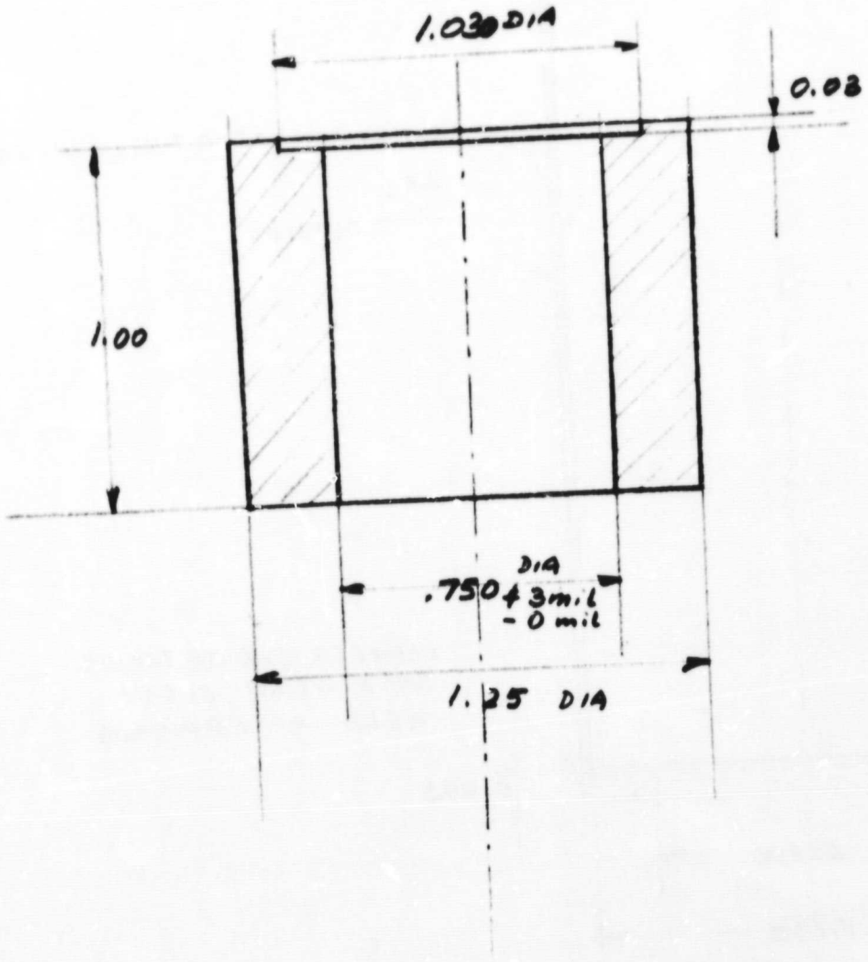

SCALE : 2:1

MATERIAL : TOOL STEEL

METAL ION SOURCE
DWG # 10
SOURCE CAPSULE

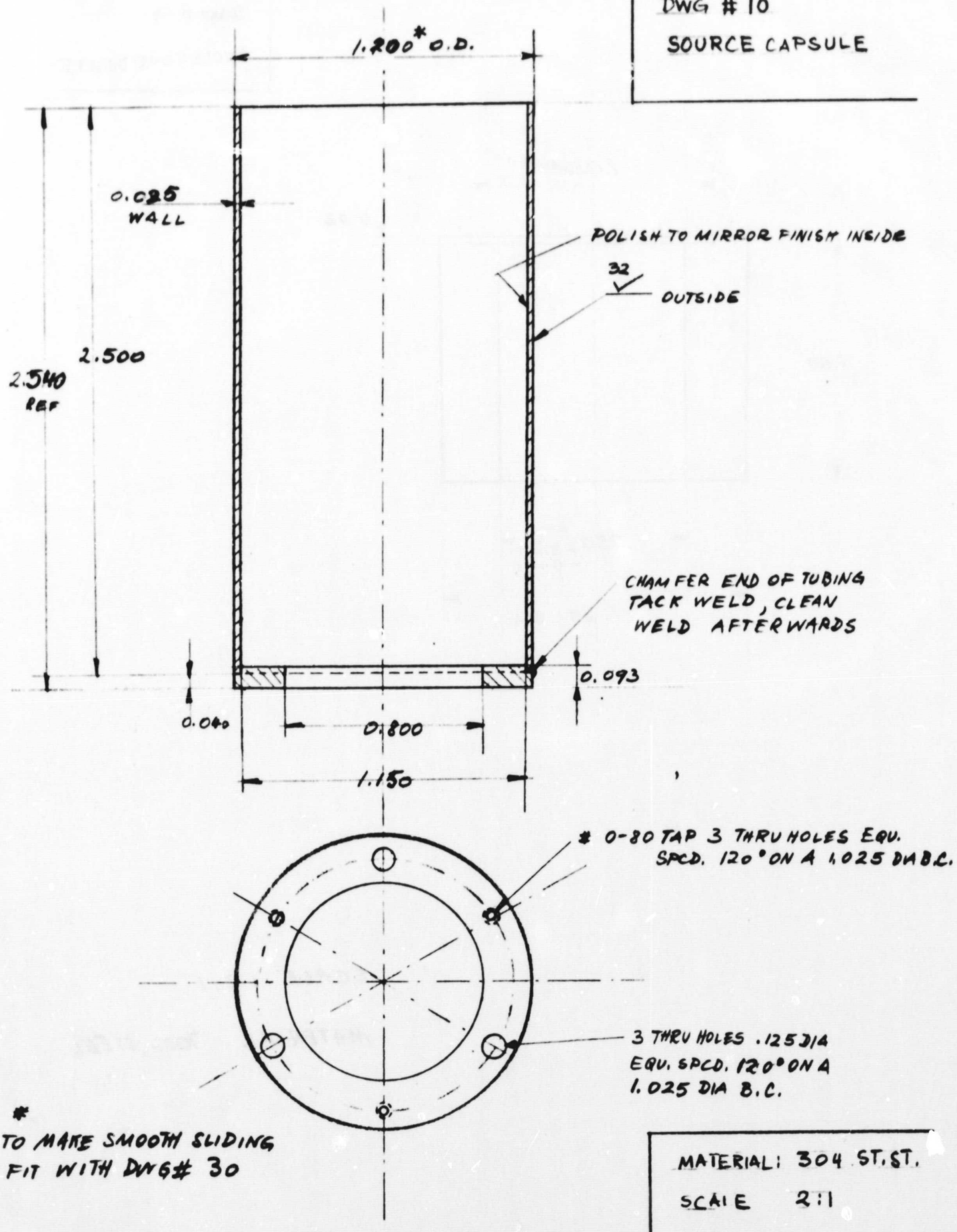

* TO MAKE SMOOTH SLIDING FIT WITH DWG# 30

MATERIAL: 304 ST. ST.
SCALE 2:1

METAL ION SOURCE
DWG # 11 A
EXTRACTION ELEC
TRODE SUPPORT

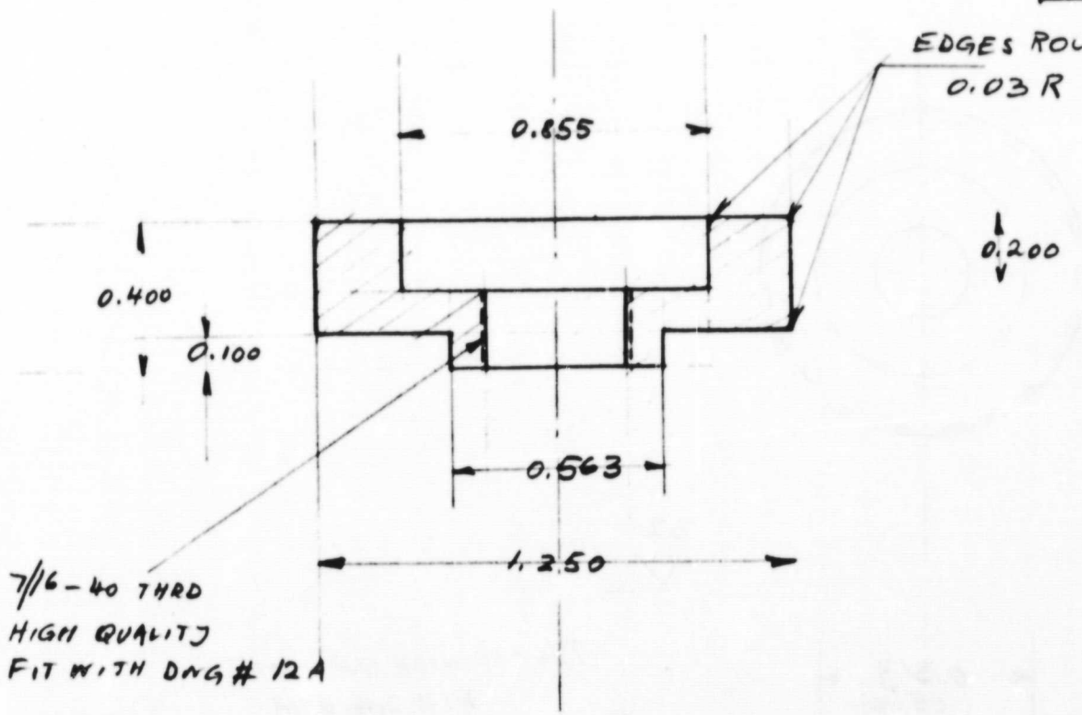

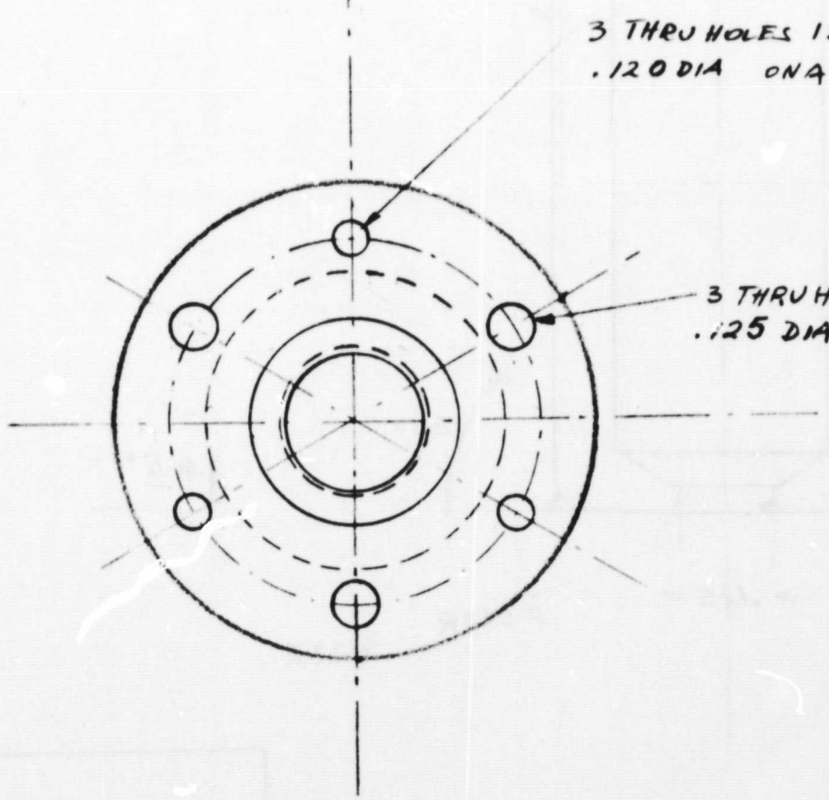

SCALE 2:1
MAT.: 304 ST.ST.

METAL ION SOURCE
DWG # 12 A
EXTRACTION ELECTR.

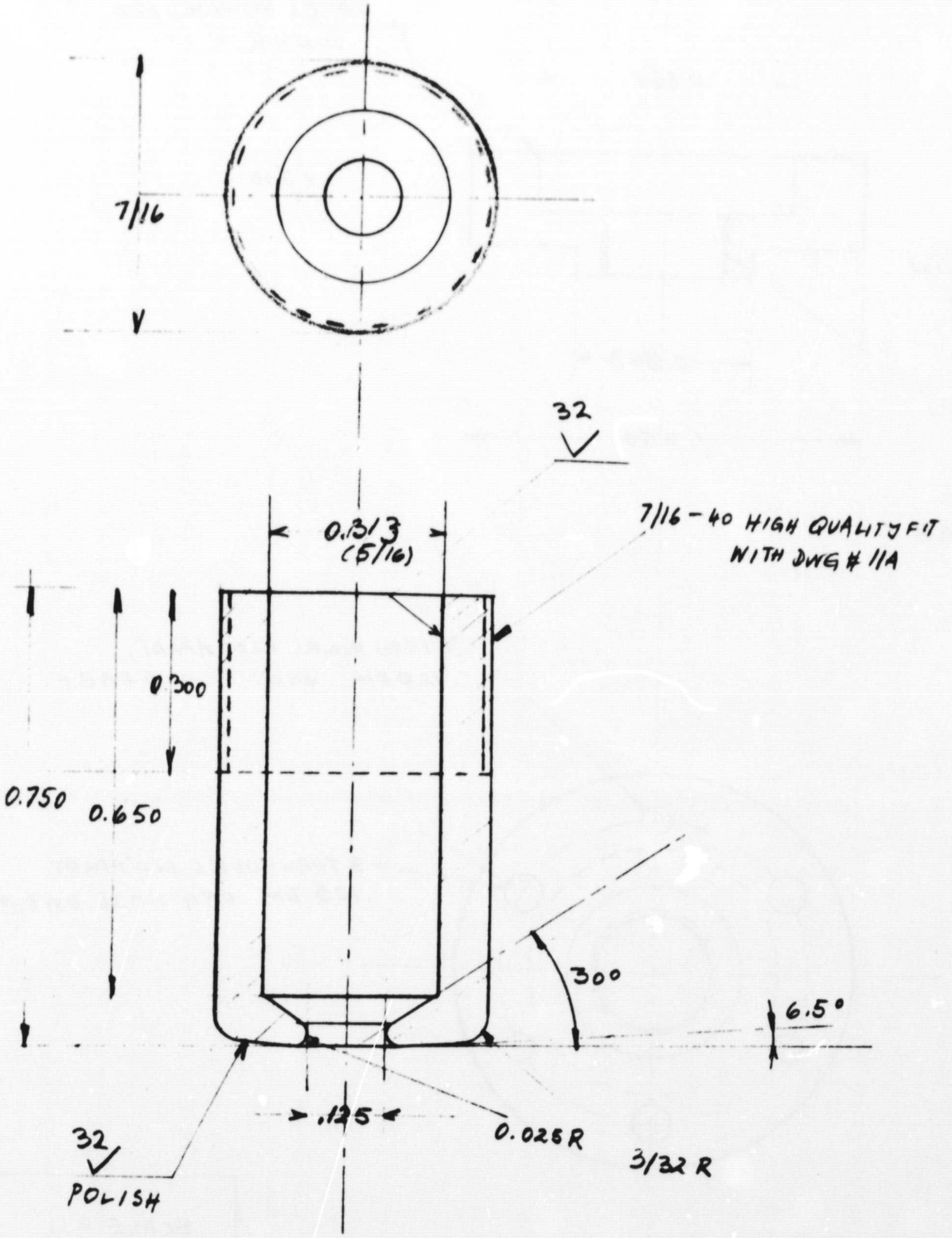

SCALE 4:1
MAT: Tantalum

METAL ION SOURCE
DWG# 13
ANODE CONE DIE SET I

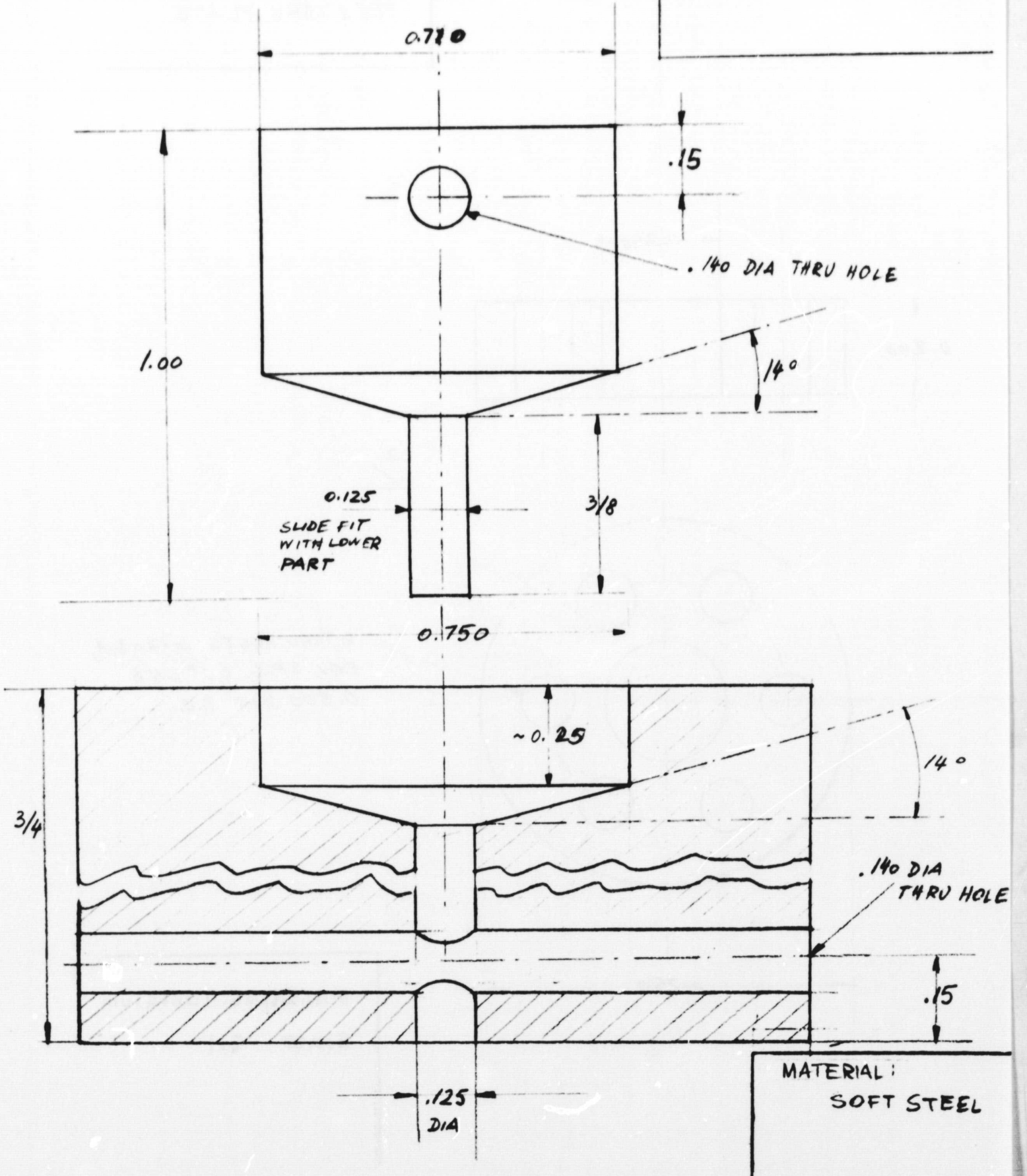

MATERIAL:
SOFT STEEL

METAL ION SOURCE

DWG # 14

FEEDTHRU PLATE

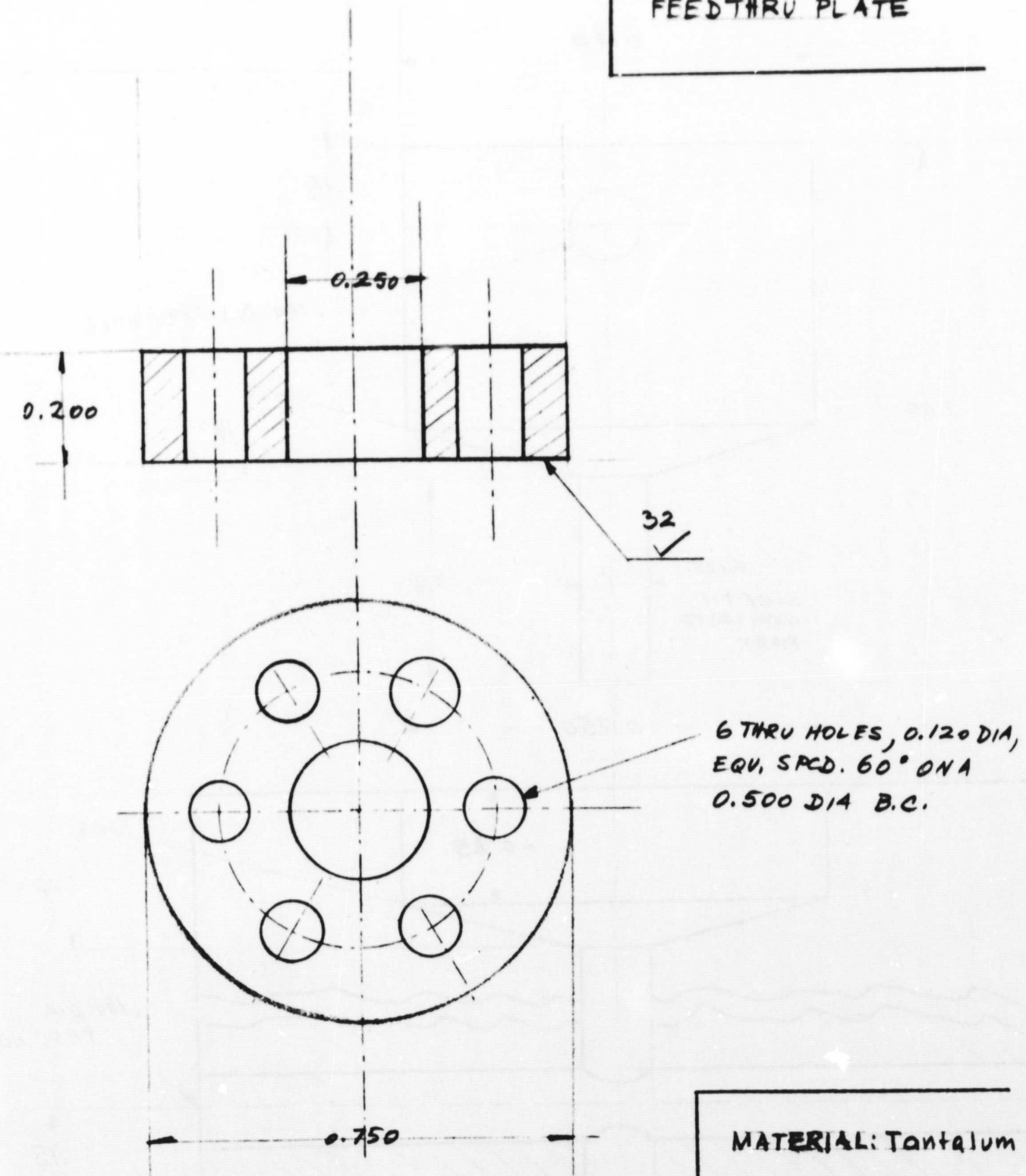

MATERIAL: Tantalum

Scale 4:1

METAL ION SOURCE
DWG #15
ANODE HEATSHIELD

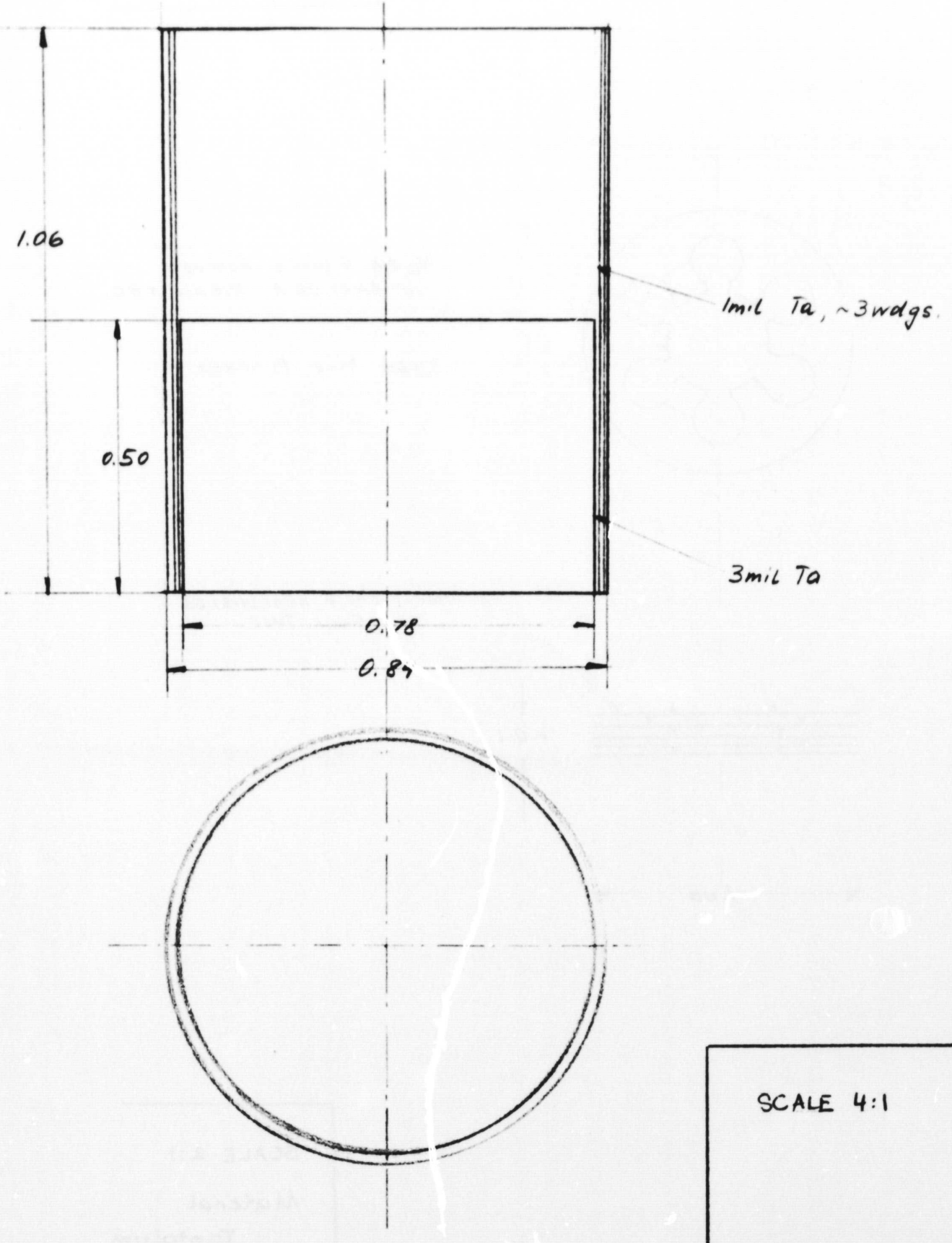

SCALE 4:1

METAL ION SOURCE
DWG # 16
CHAMBER REAR SHIELD

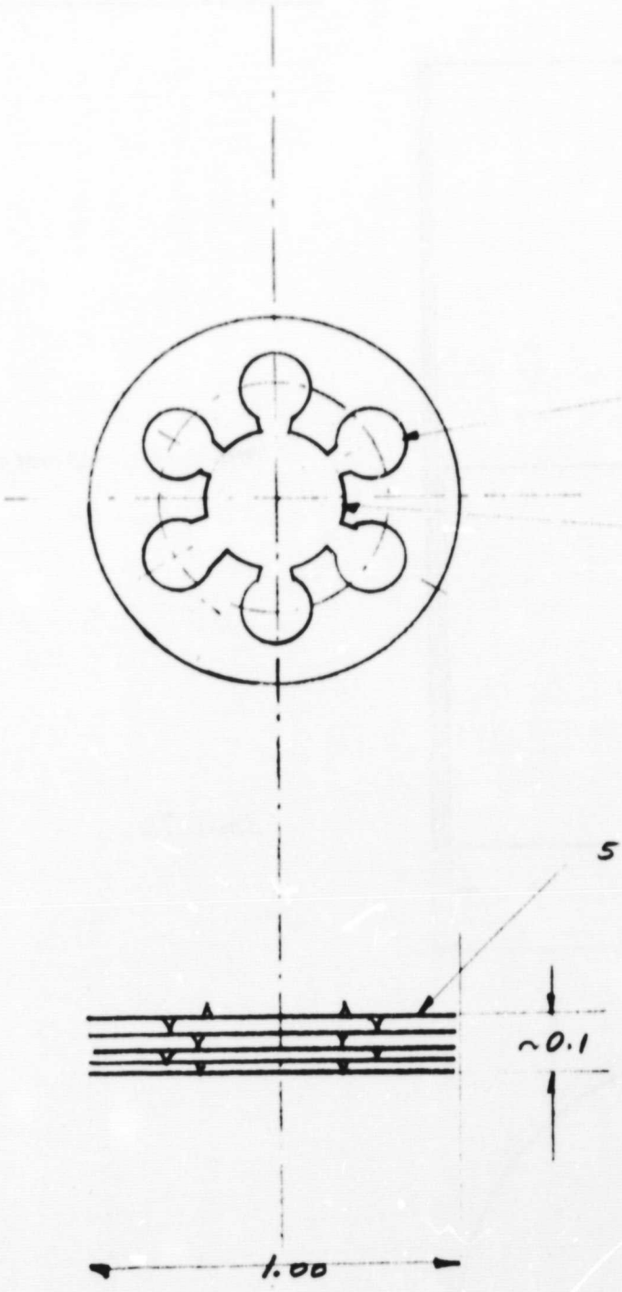

SCALE 2:1
Material:
Tantalum

METAL ION SOURCE
DWG # 17
ANODE CONE DIE SET II

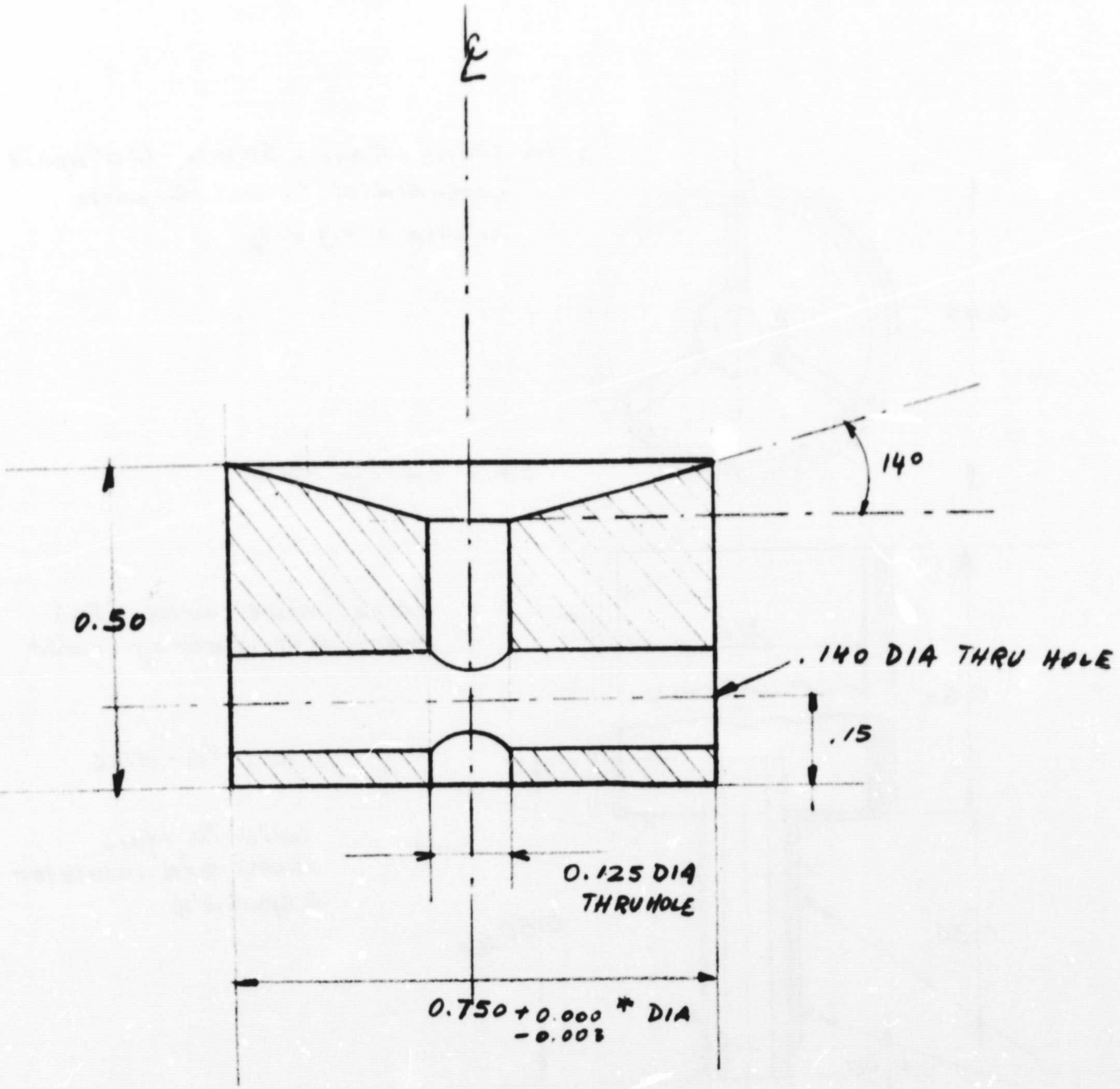

* TO MAKE SMOOTH FIT WITH DWG #

METAL ION SOURCE

DWG # 18

OVEN BACK COVER

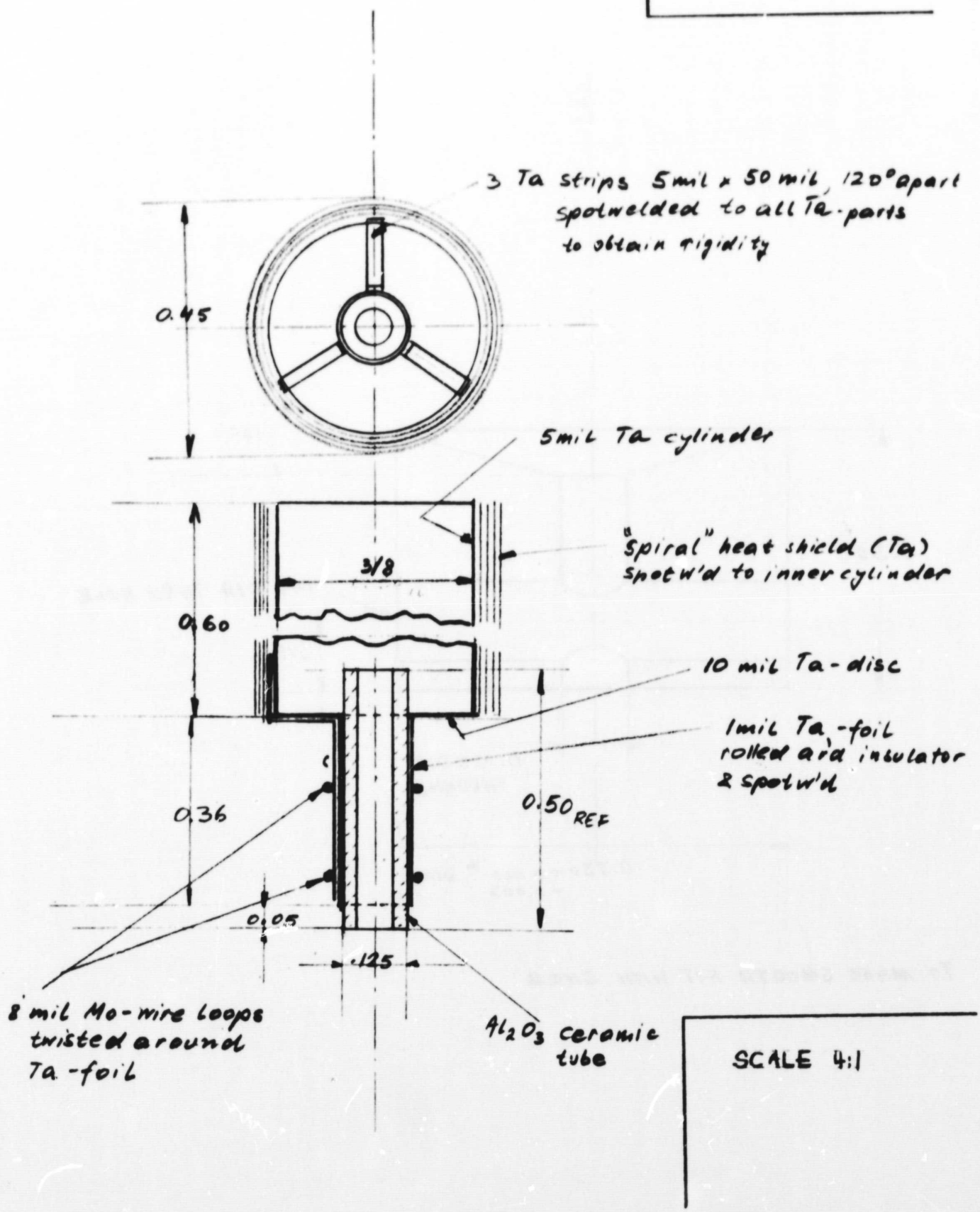

SCALE 4:1

METAL ION SOURCE
DWG # 19
CAN BACK SHIELD

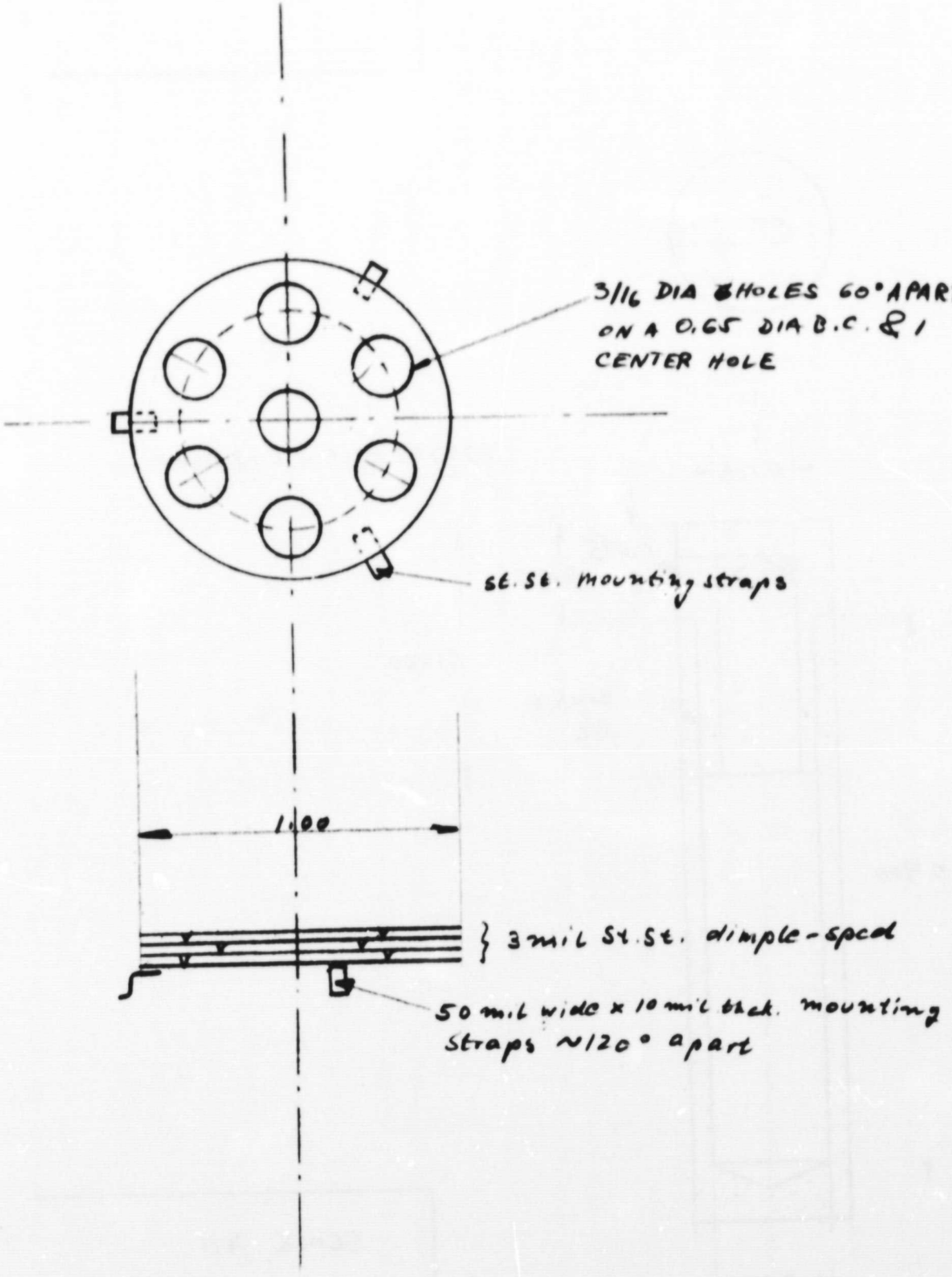

METAL ION SOURCE

DWG # 20

OVEN AND PLUG

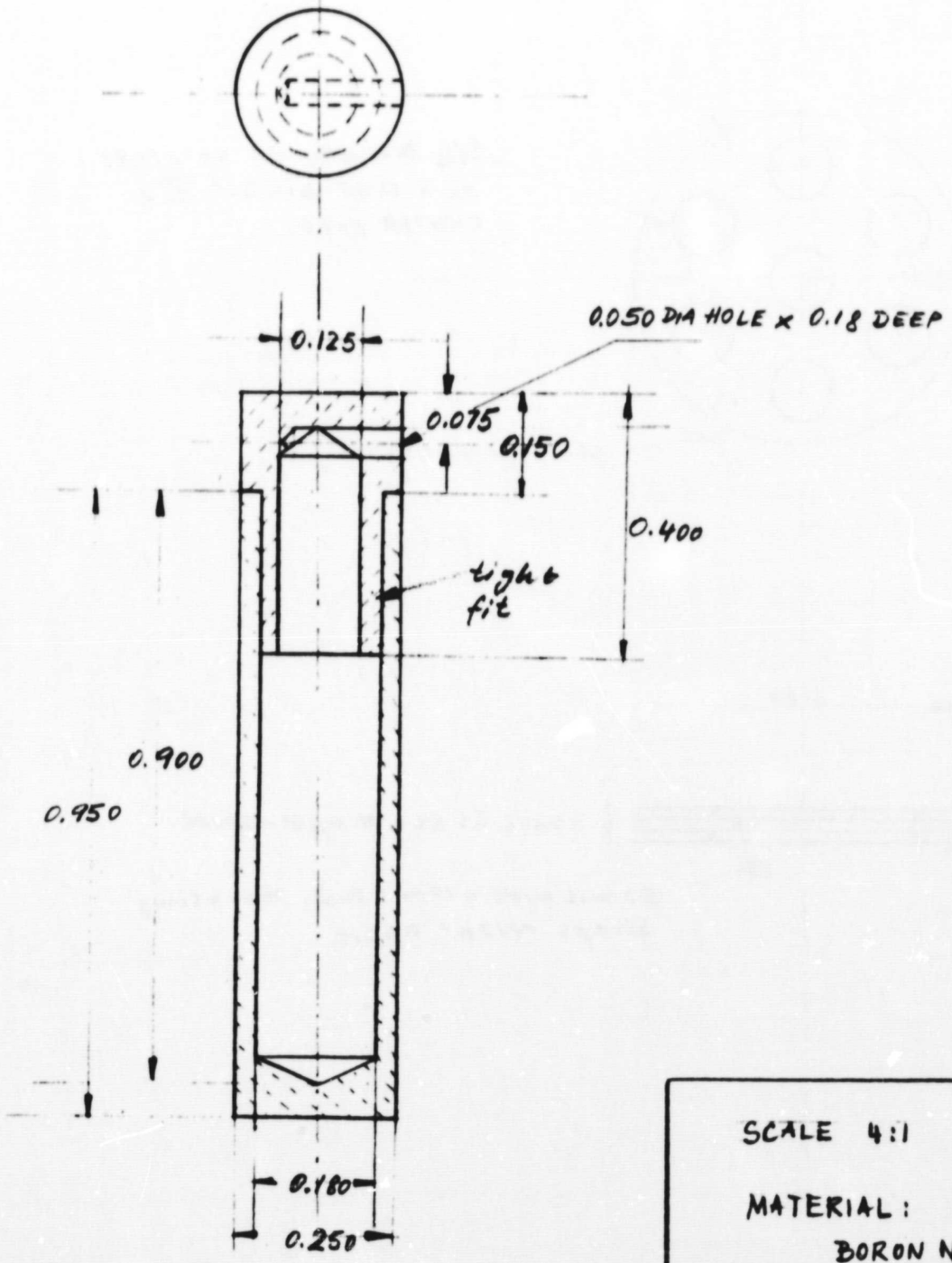

SCALE 4:1

MATERIAL:
BORON NITRIDE

METAL ION SOURCE
DWG # 21
OVEN HEATER & SHIELD ASS'Y

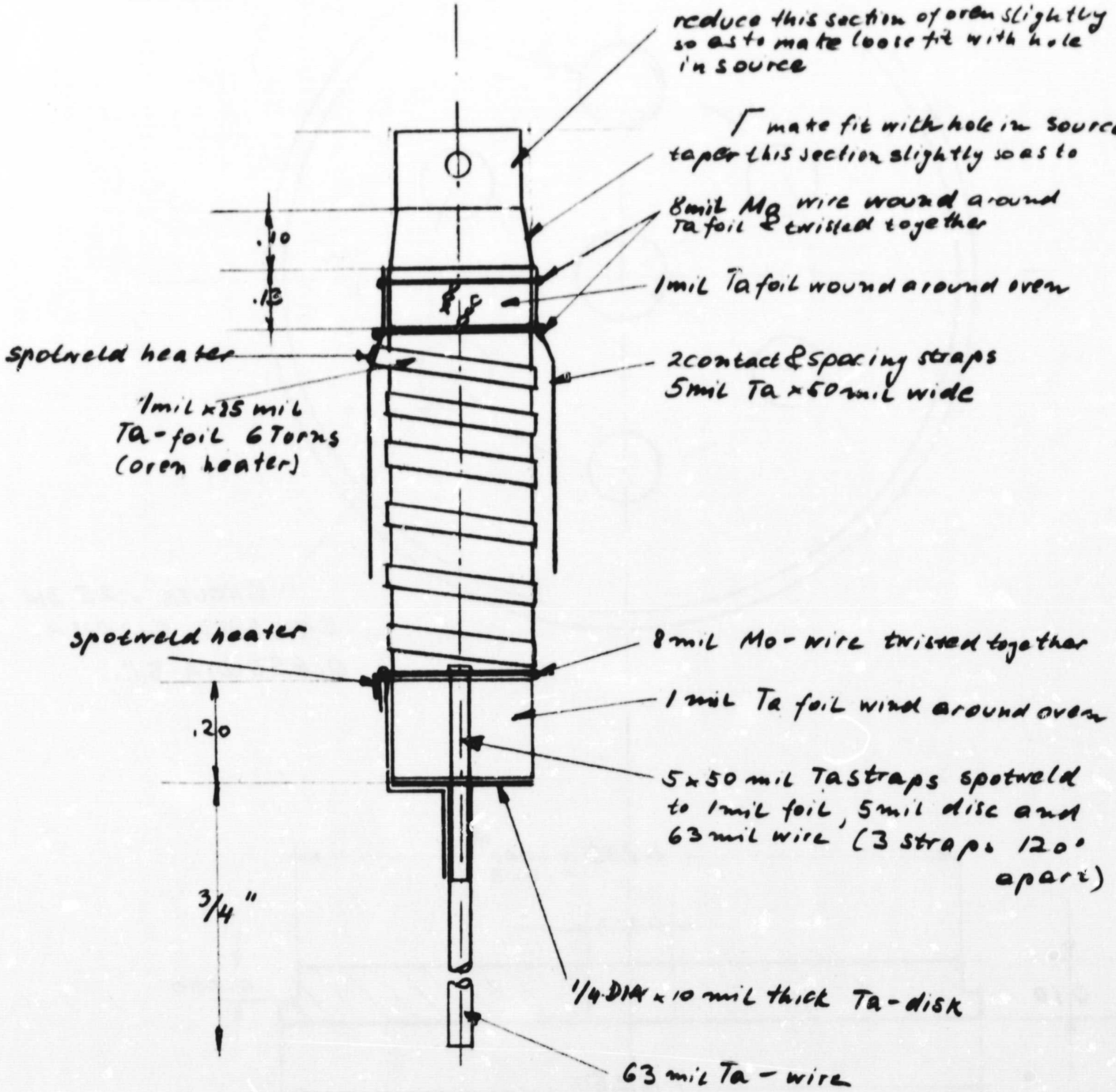

METAL ION SOURCE
DWG #22
CAN BACK PLATE

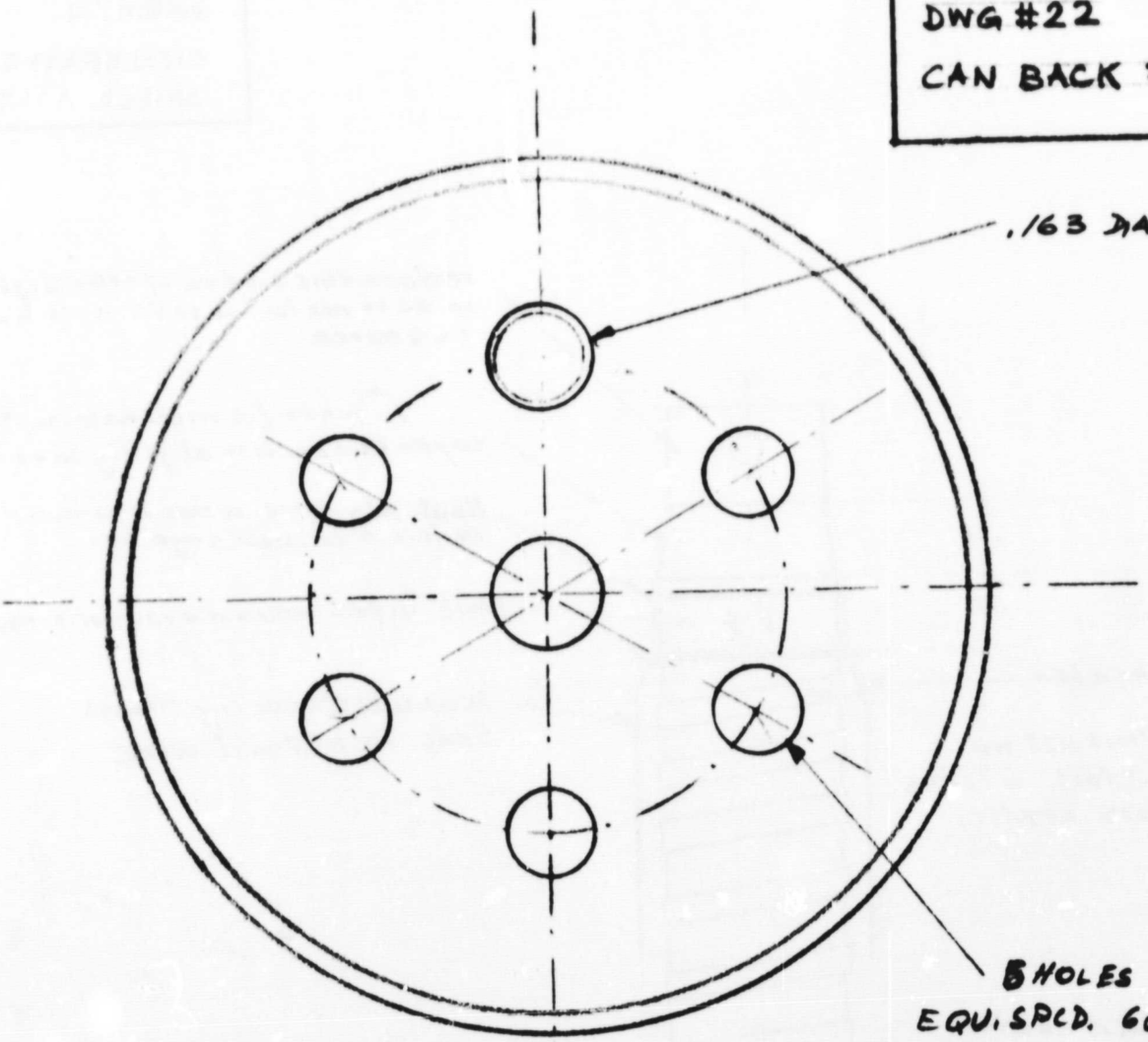

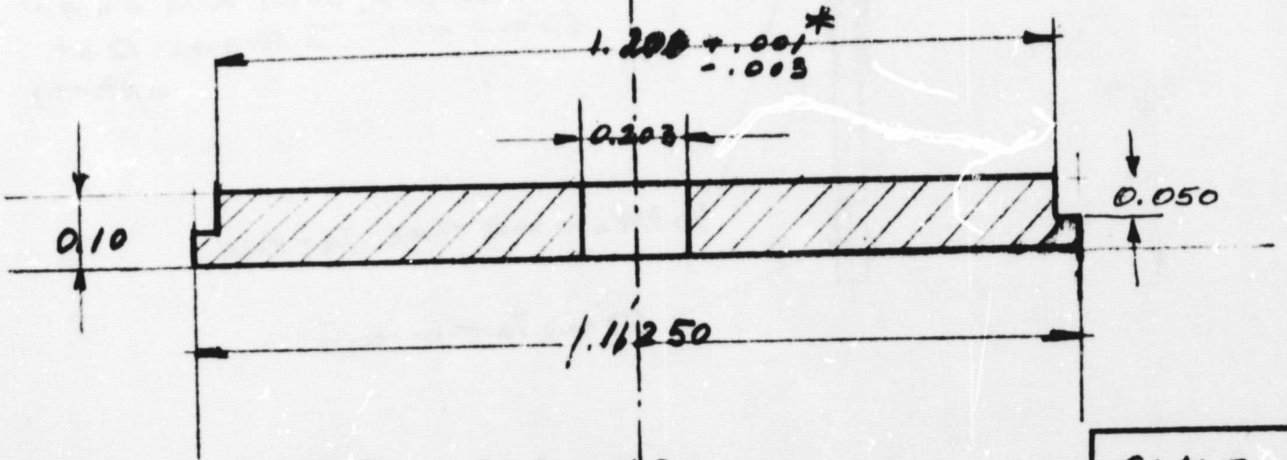

* TO MAKE TIGHT FIT WITH DWG # 30

SCALE 4:1
MATERIAL:
ST. ST. 304 or 316

METAL ION SOURCE

DWG # 23

HOUSING TUBE # 1

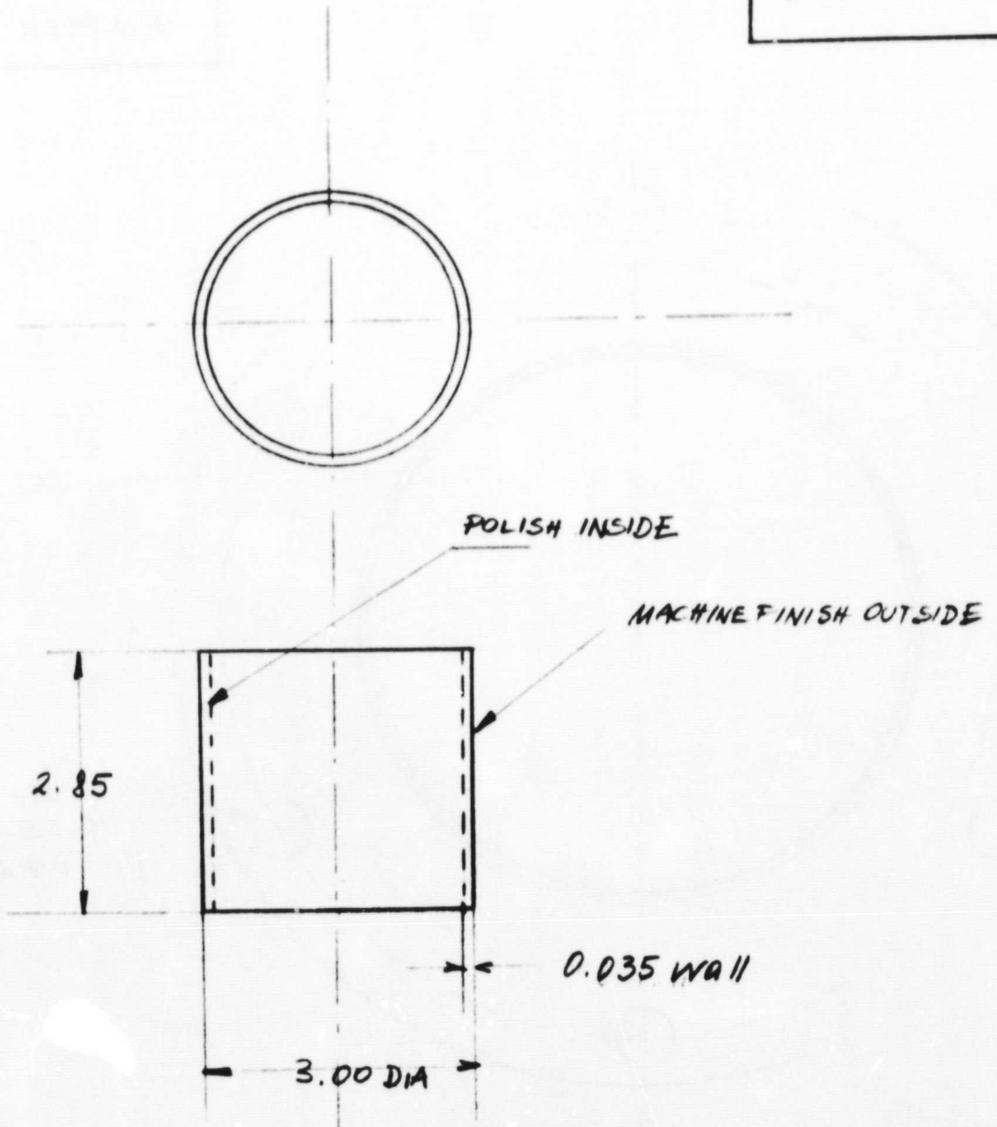

SCALE 1:2

MATERIAL 304 ST. ST.

METAL ION SOURCE
DWG # 24
ACCELERATOR
ADAPTER FLANGE

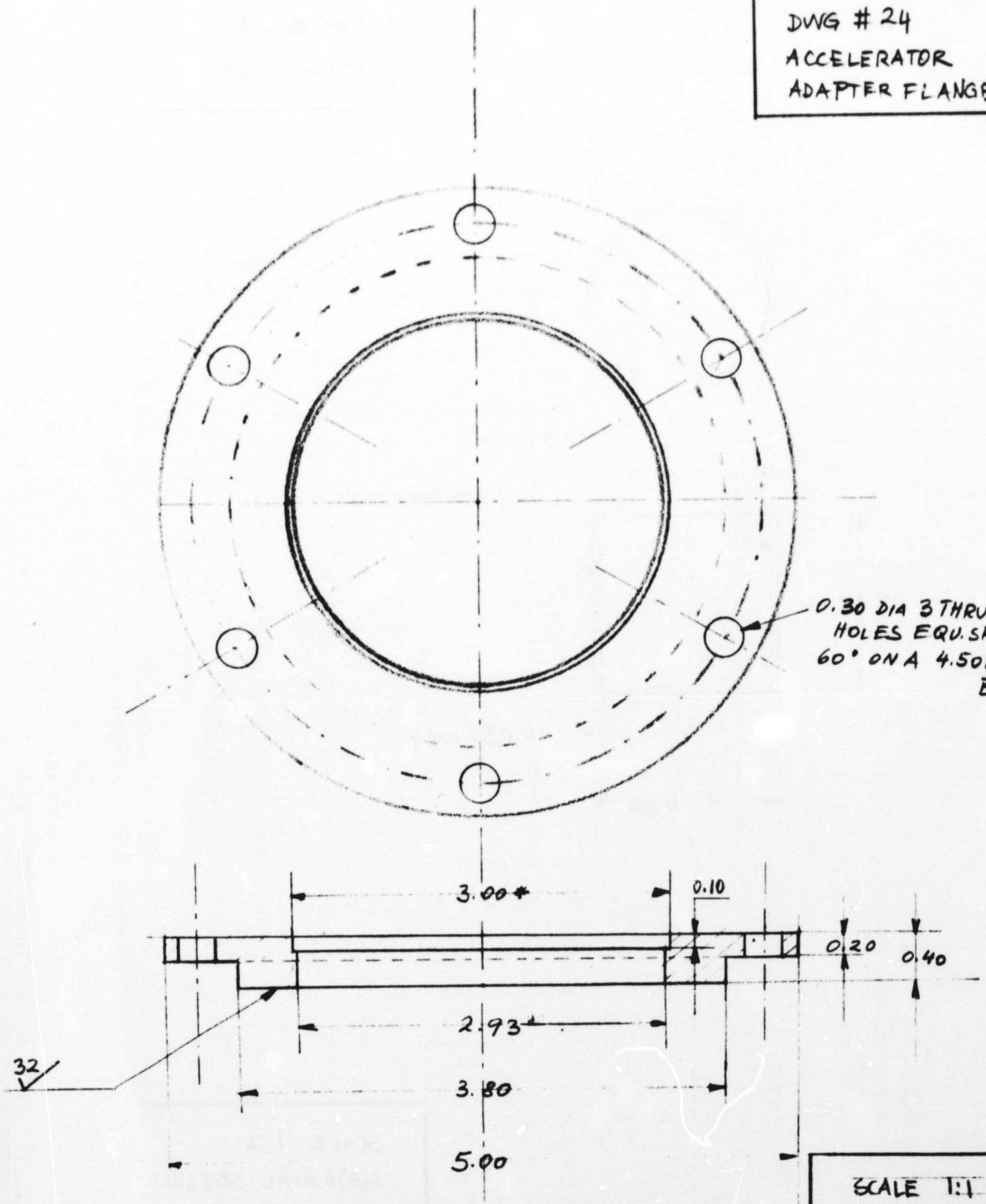

SCALE 1:1
MAT.: 304 ST. ST

* TO MAKE TIGHT FIT WITH DWG # 23

NOTE: MACHINE FINISH ALL SURFACES, IF NOT OTHERW. SPEC.

METAL ION SOURCE
DWG # 25
HOUSING TOP PLATE

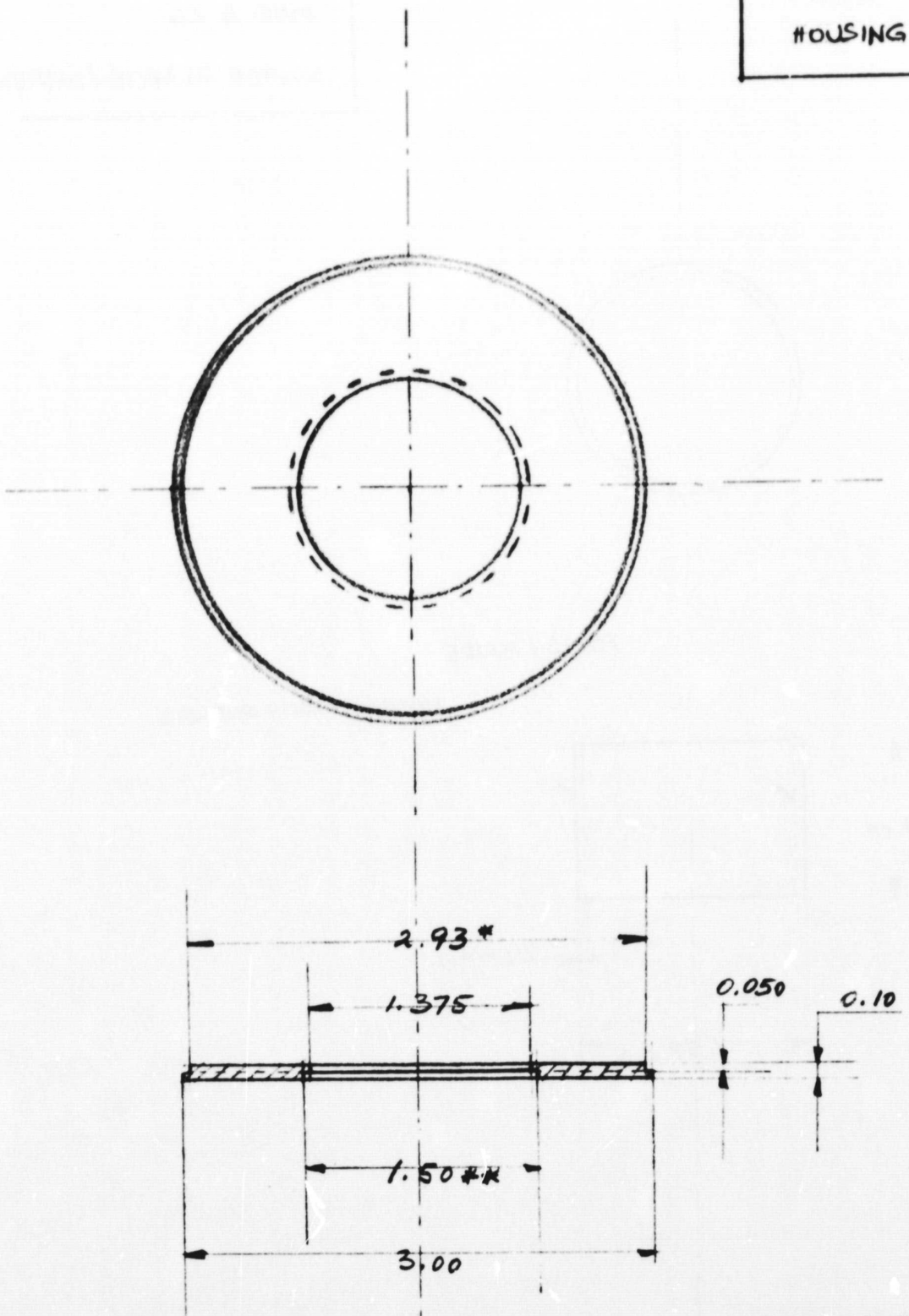

* TO MAKE CLOSE FIT WITH DWG# 23

** — " — 26

NOTE: ALL SURFACES MACHINE FINISH

SCALE 1:1

MATERIAL: 304 ST. ST

METALION SOURCE

DWG # 26

SOURCE FLANGE ADAPTER

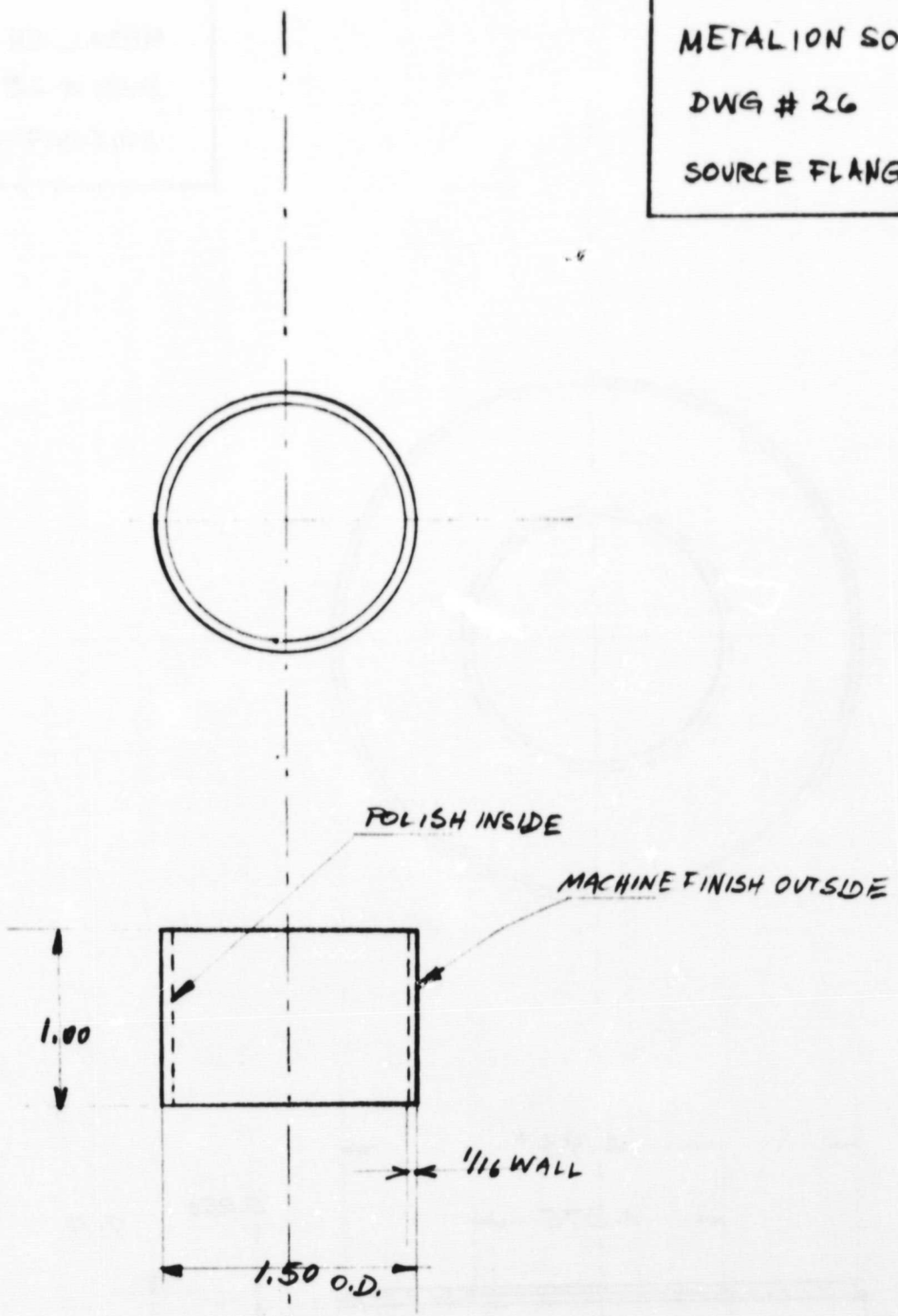

SCALE 1:1

MATERIAL: 304 S.S

METAL ION SOURCE

DWG # 27

COOLING FIN HOLDER

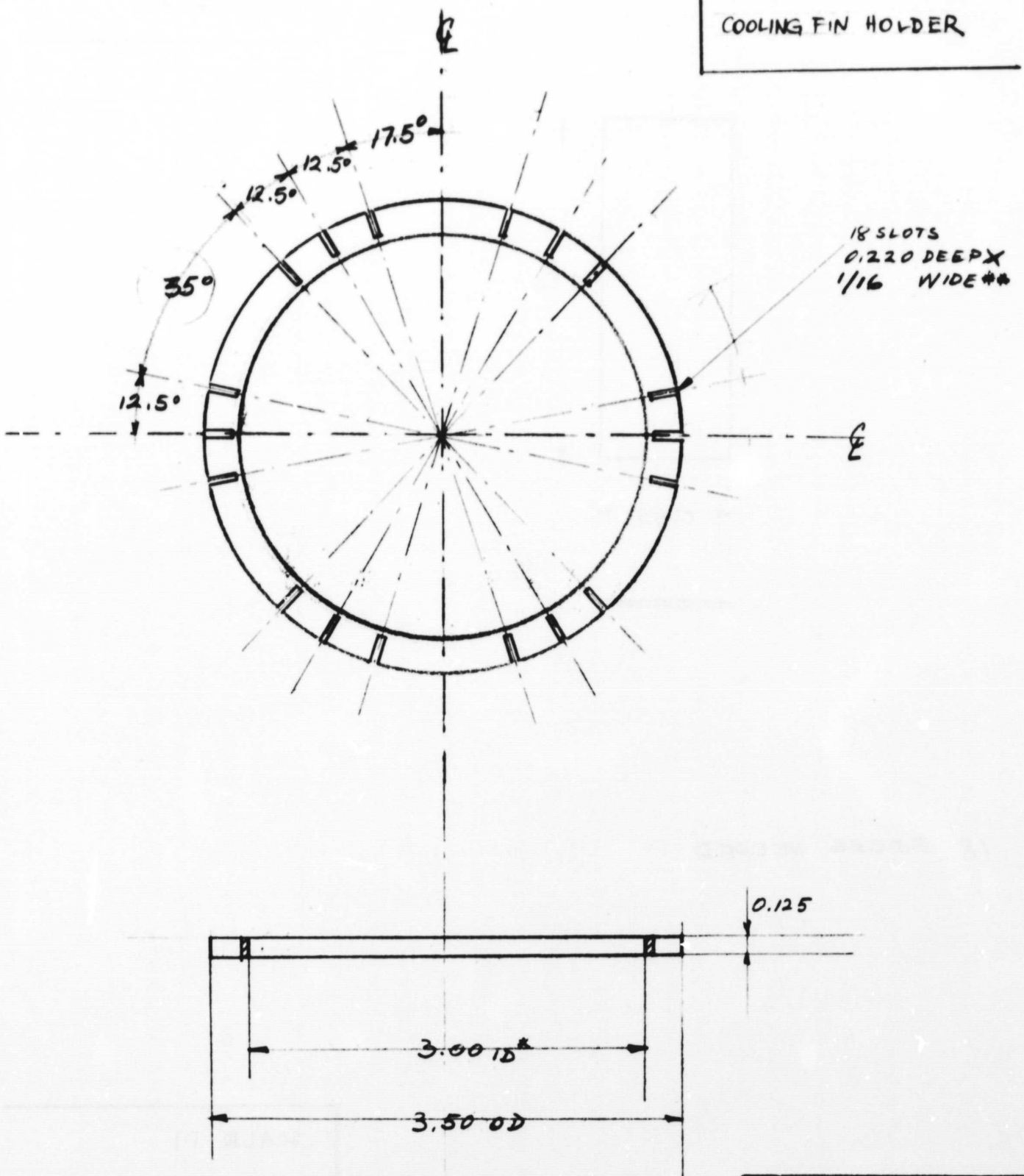

* TO MAKE SMOOTH FIT WITH DWG # 23

** TO MAKE TIGHT FIT WITH DWG # 28

SCALE 1:1

MATER.: COPPER

METAL ION SOURCE

DWG # 28

COOLING FIN

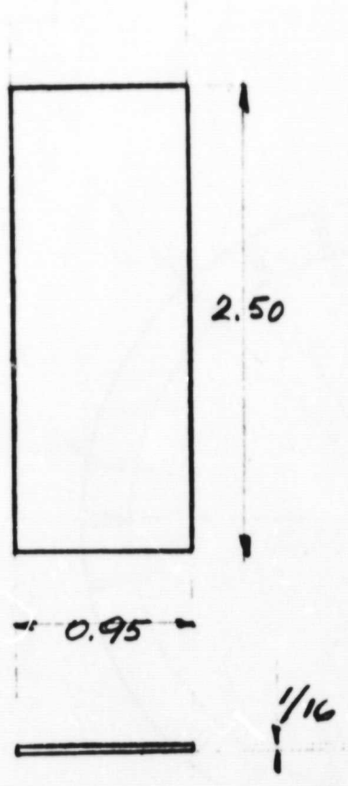

18 PIECES NEEDED

SCALE 1:1

MATERIAL: COPPER

METAL ION SOURCE
DWG # 29
FEEDTHRU FLANGE

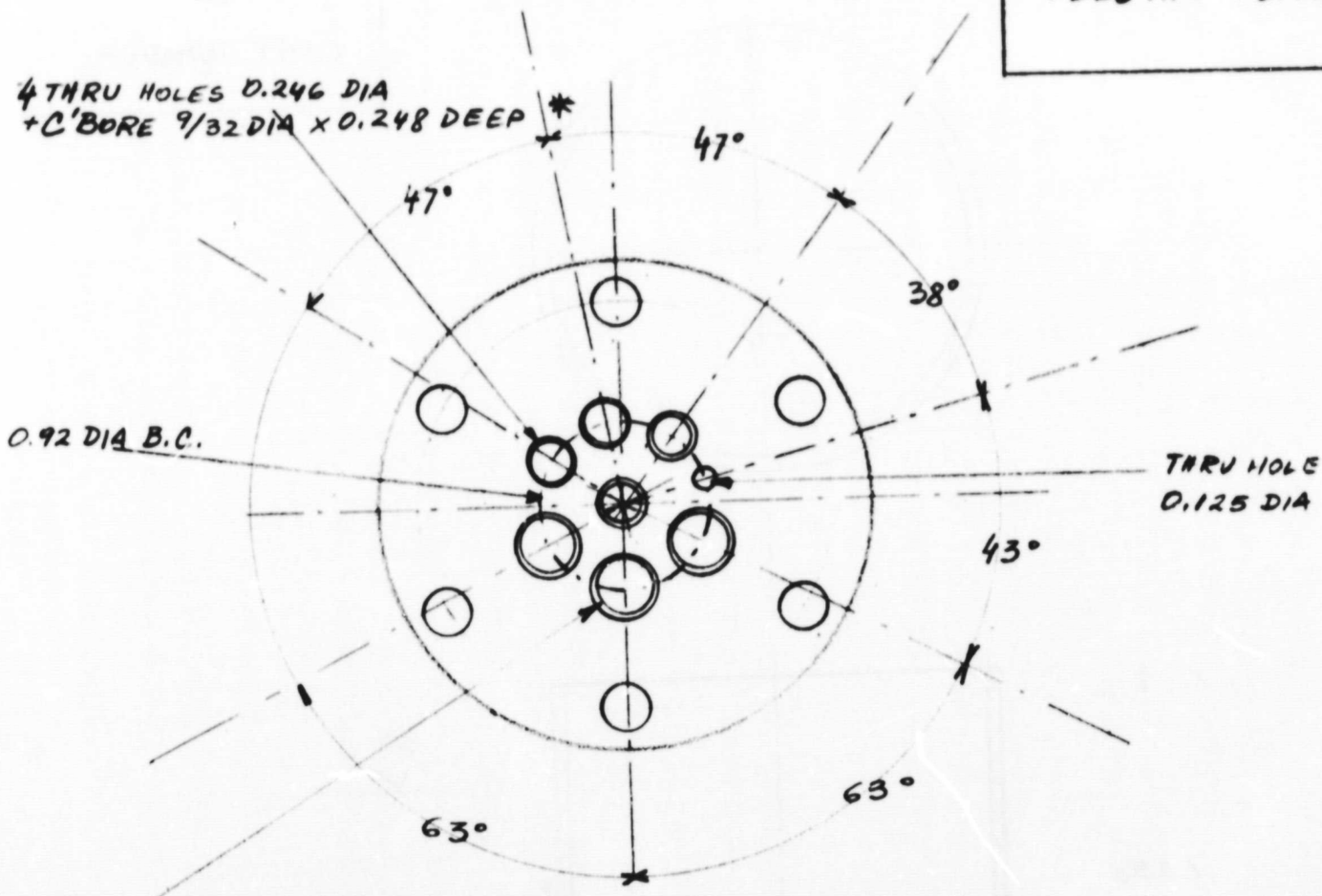

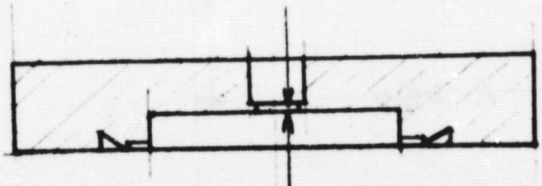

50 mil step all counterbores

* COUNTER BORES ALL ON
FLAT SIDE OF FLANGE

SCALE 1:1

VARIAN SS 1½ nom
Flange

METAL ION SOURCE

DWG # 30

CAN CYLINDER

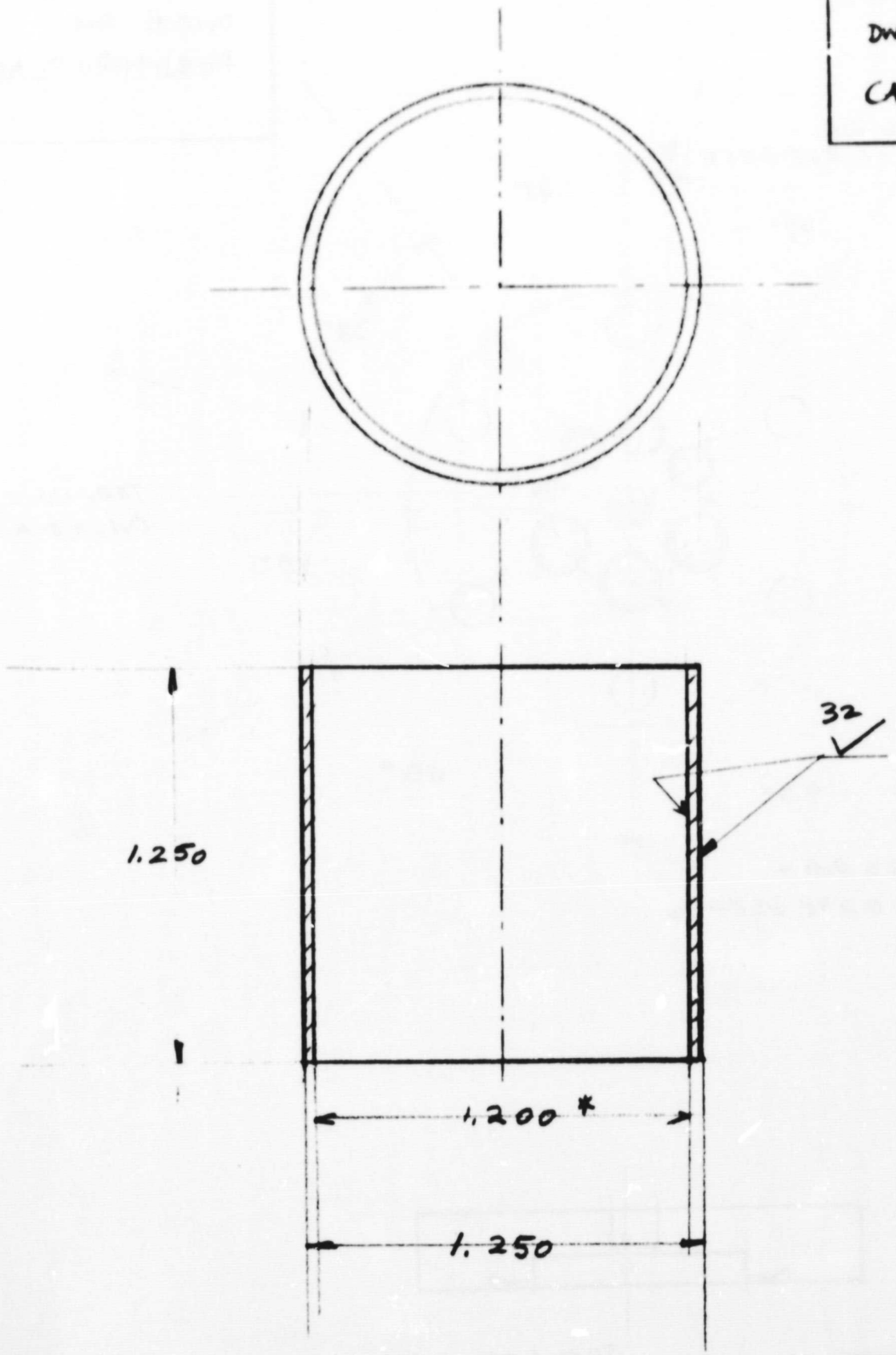

* TO MAKE SMOOTH SLIDING FIT WITH DWG # 10

MATERIAL : 304 ST. ST

SCALE 2:1

METAL ION SOURCE

DWG # 31

FLANGE PIN WIRING

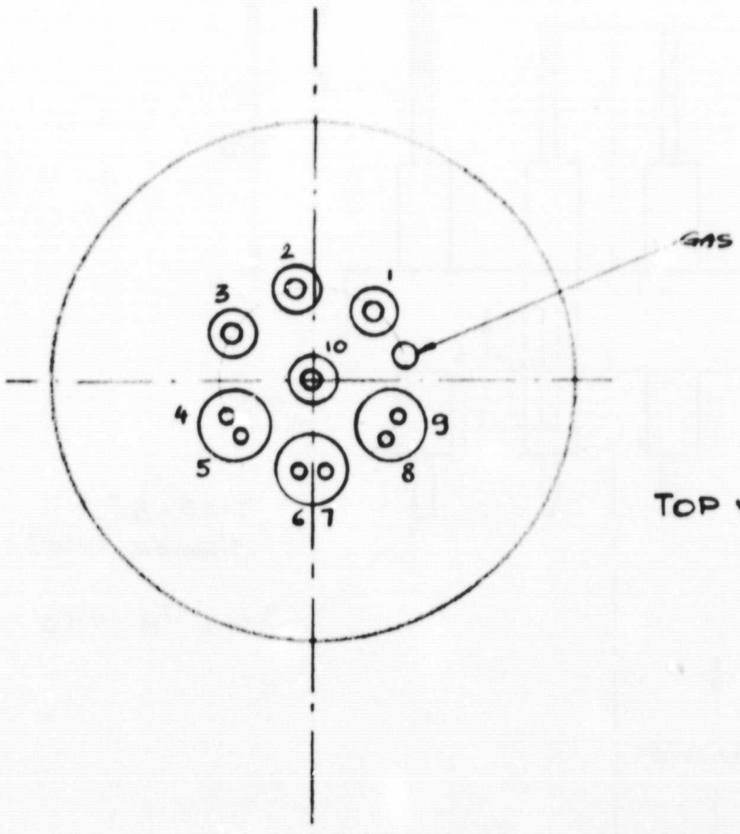

TOP VIEW

1	—
2	EXTRACTOR
3	FILAMENT
4	—
5	—
6	HEATER
7	—
8	OVEN
9	INTERM. ELECTR.
10	FILAMENT

METAL ION SOURCE
DWG # 32
FEEDTHRU ARR'MT

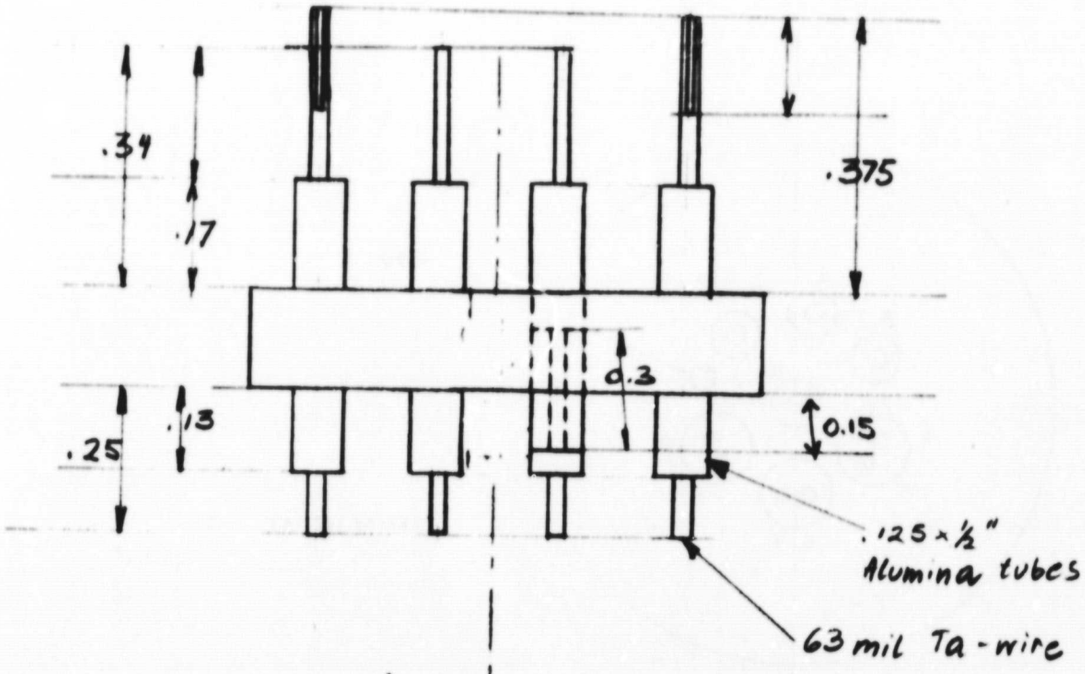

not to scale

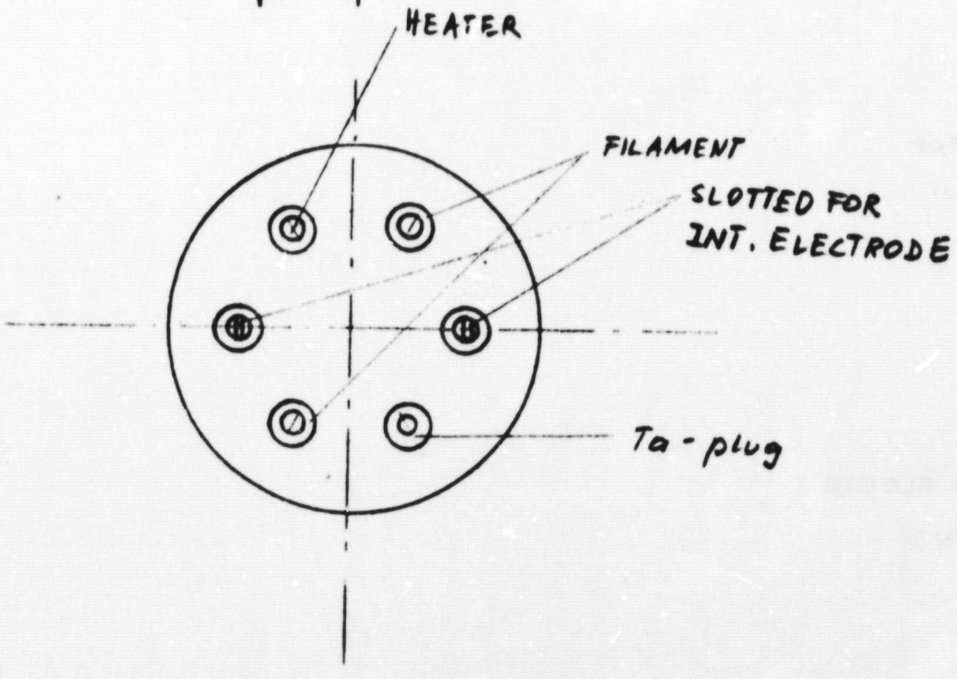

METAL ION SOURCE
DWG # 33
SCHEMATIC

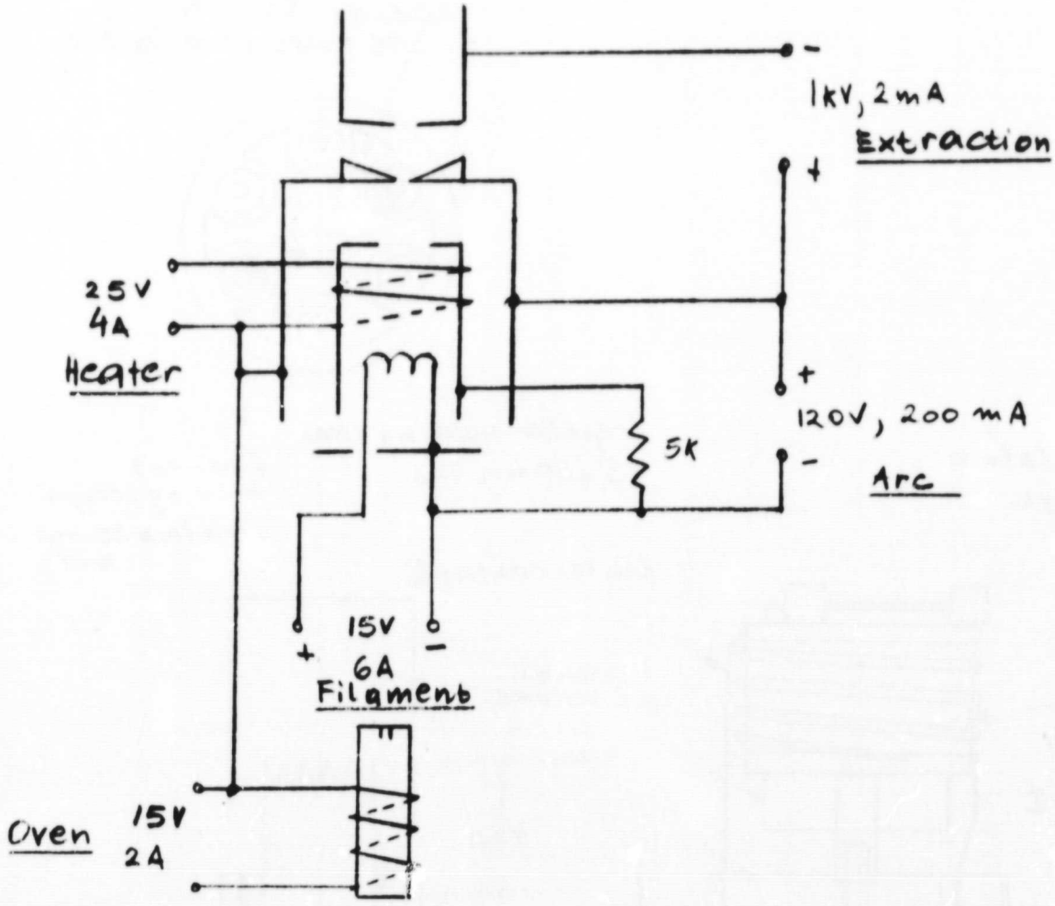

Pin arrangement on outersource can :

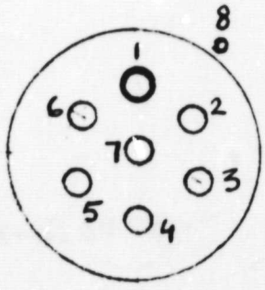

1 Gas
2 Spare
3 Filament
4 Heater
5 Intermediary Electrode
6 Filament
7 Oven
8 Extraction

METAL ION SOURCE
DWG# 34
SOURCE INTERIOUR

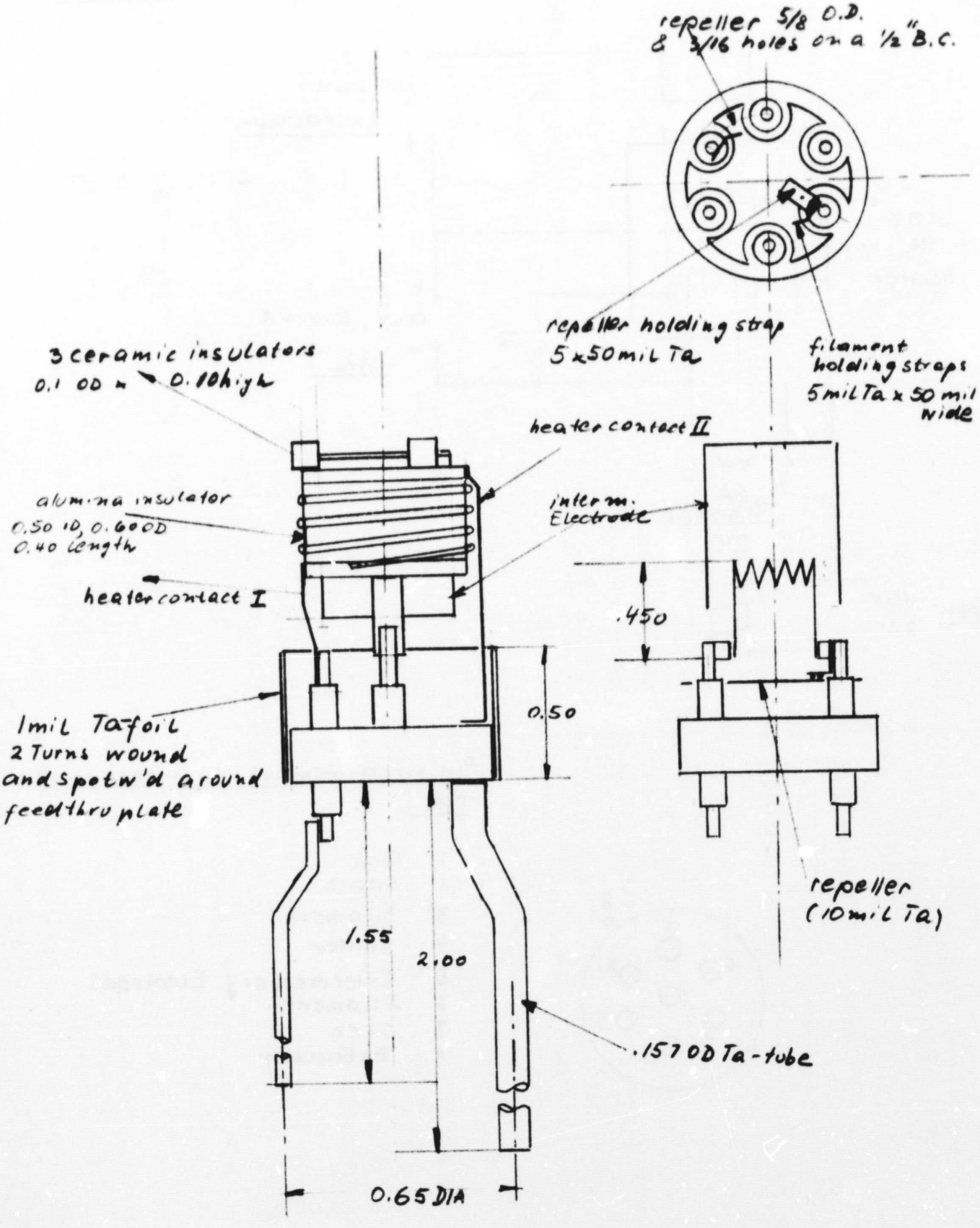

METAL ION SOURCE
DWG # 35
FILAMENT ASS'Y

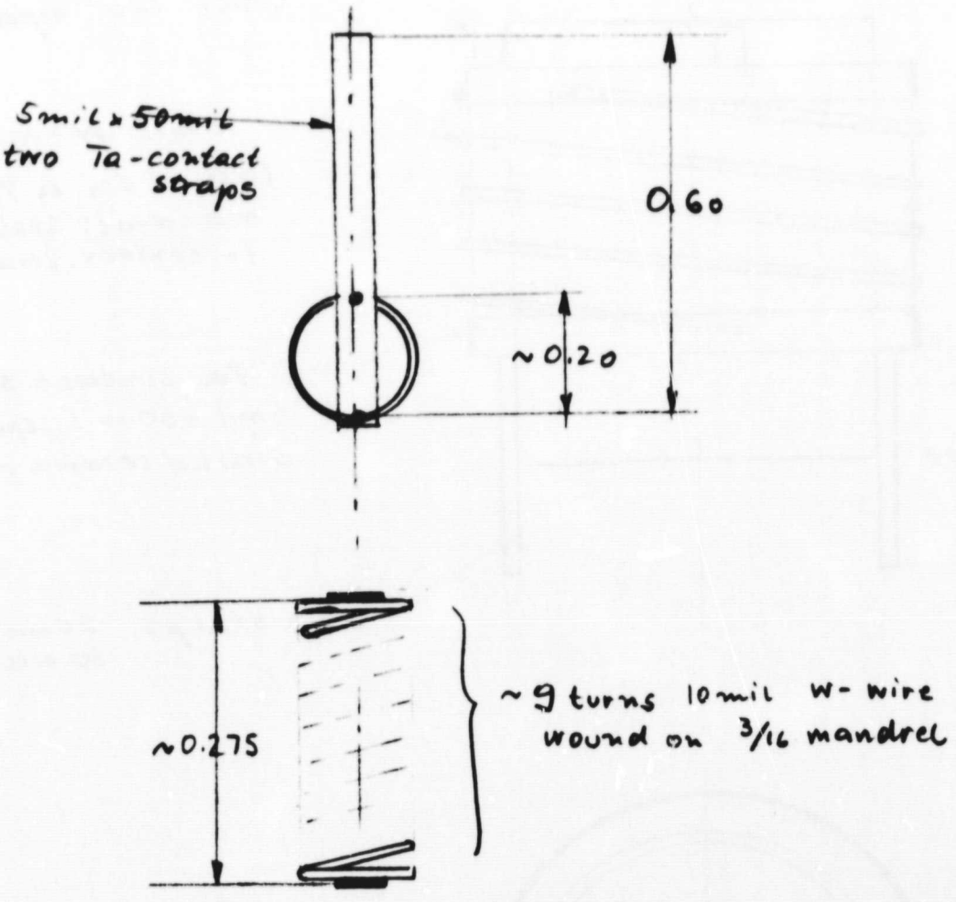

METAL ION SOURCE
DWG # 36
INTERMED. ELECTRODE
& HEATER ARRG'T

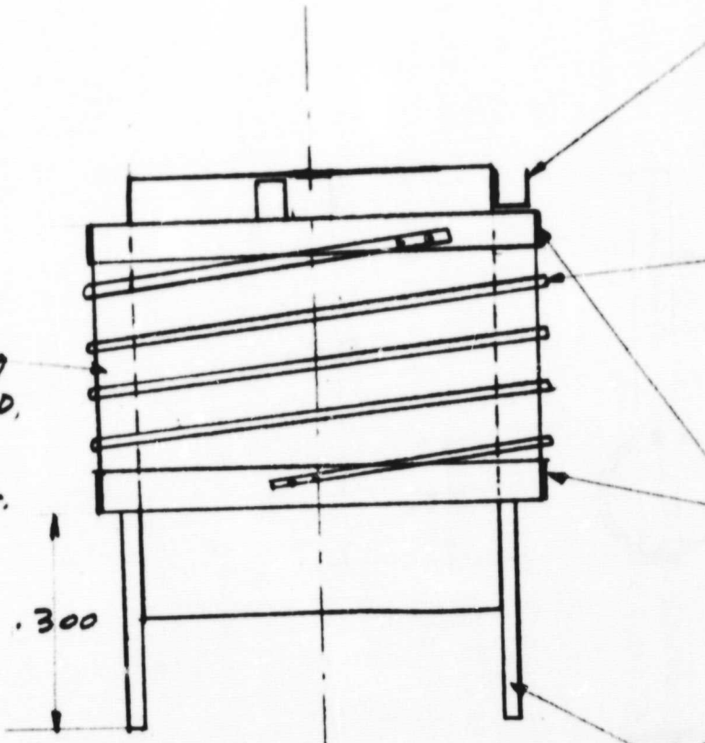

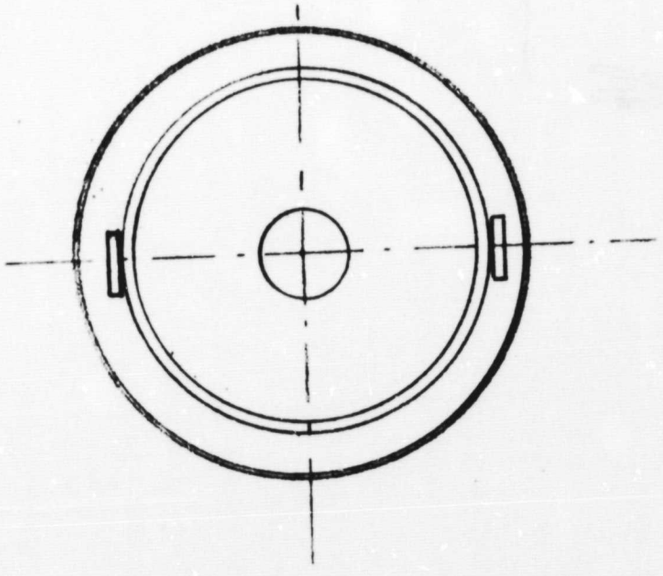

METAL ION SOURCE
DWG # 37
CAN MOUNTING ASS'Y

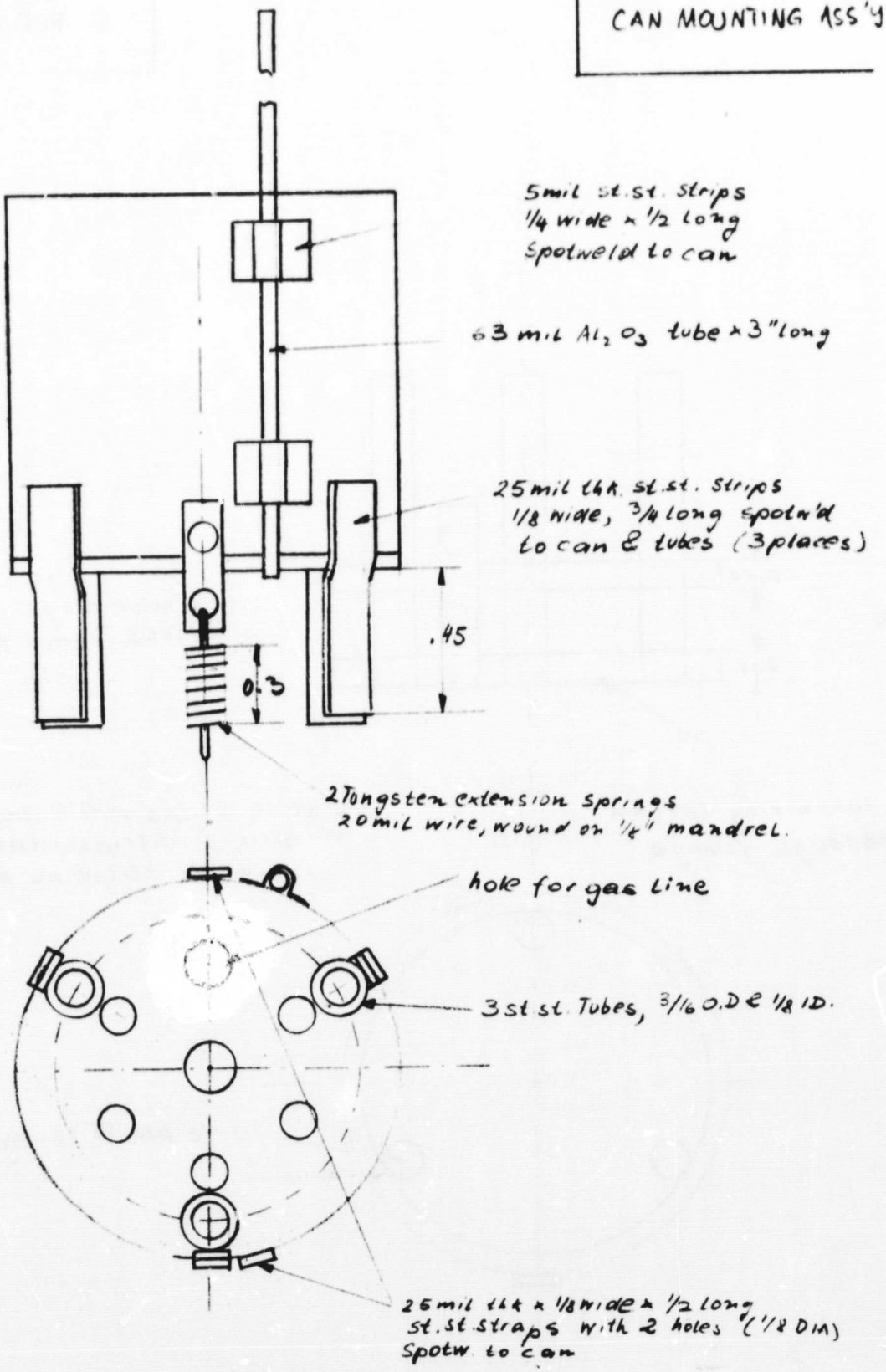

METAL ION SOURCE
DWG# 38
SOURCE MTG. ASS'Y

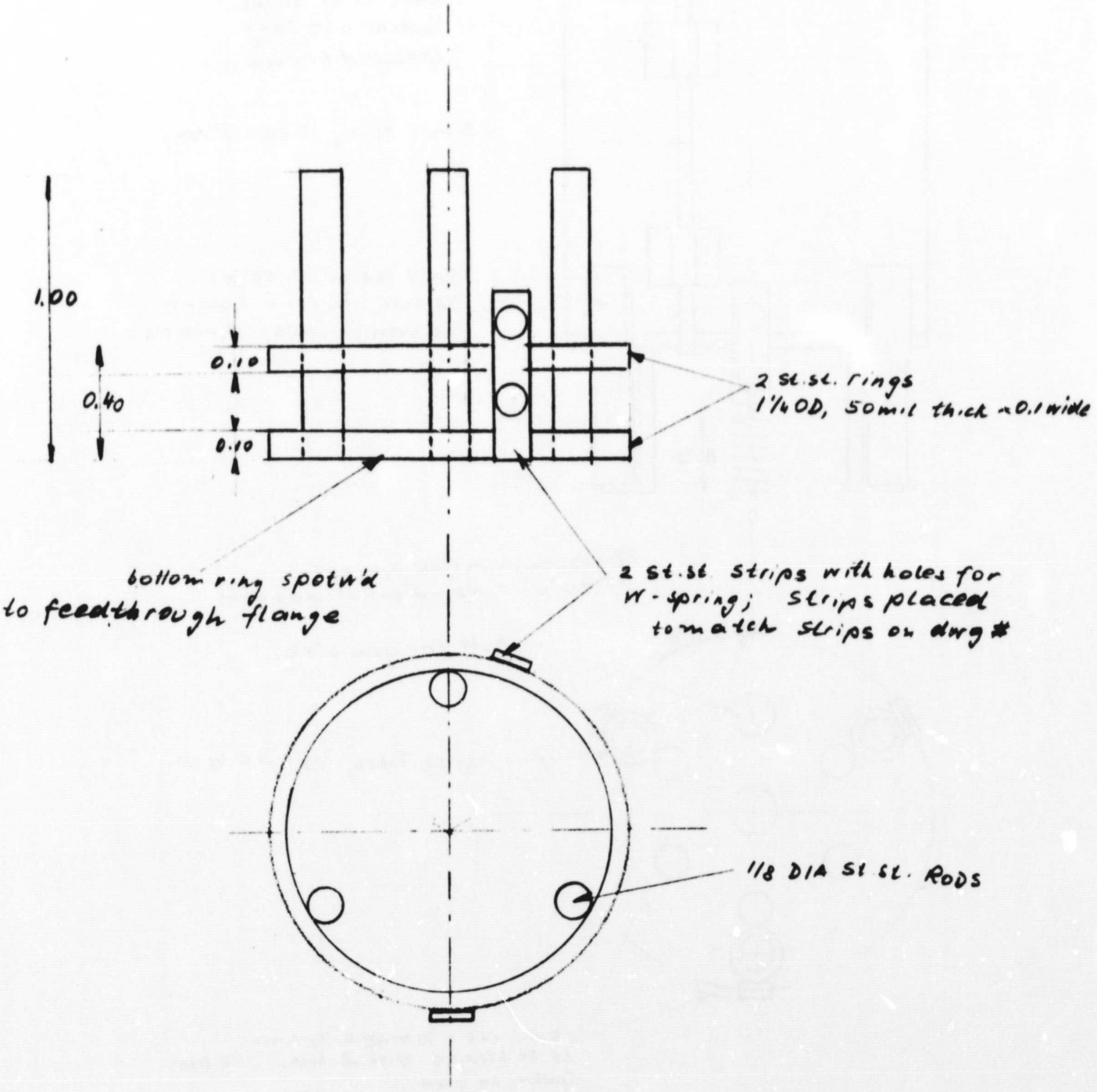

METAL ION SOURCE

FLANGE WELDING

DWG # 3